

**A melt inclusion study of the Sudbury Igneous Complex (Ontario, Canada):
Evidence for two-liquid immiscibility and constraints on trace element distribution**

By Kathleen M. Watts

Thesis Submitted to Saint Mary's University, Halifax, Nova Scotia in Partial Fulfillment
of the Requirements for the Degree of Master of Science in Applied Science

April 29, 2014, Halifax, Nova Scotia

© Kathleen M. Watts, 2014

Approved: Dr. Jacob Hanley
Supervisor
Department of Geology
Saint Mary's University

Approved: Dr. Doreen Ames
Supervisory Committee
Geological Survey of Canada (GSC)

Approved: Dr. Daniel Kontak
Supervisory Committee
Mineral Exploration Resource Centre (MERC)
Laurentian University

Approved: Dr. Sarah Gleeson
Supervisory Committee
Department of Earth and Atmospheric Sciences
University of Alberta

Approved: Dr. Jason Clyburne
Supervisory Committee
Department of Chemistry
Saint Mary's University

Approved: Dr. Alan Boudreau
External Examiner
Department of Earth and Ocean Sciences
Duke University

**A melt inclusion study of the Sudbury Igneous Complex (Ontario, Canada):
Evidence for two-liquid immiscibility and constraints on trace element distribution**

By Kathleen M. Watts

April 29, 2014

Abstract

The Sudbury Igneous Complex (SIC), Ontario, Canada, is the product of a massive bolide impact and has been studied extensively due to its rich endowment of magmatic sulfide (Ni-Cu-platinum-group element) ore deposits. In this study, apatite-hosted melt inclusions from the Main Mass and quartz diorite offset dikes are analyzed for trace and major element compositions. The results of apatite-hosted melt inclusion major and trace element chemistry show two contrasting Si- and Fe-rich coevally (co-entrapped) melt inclusions are present in the SIC Main Mass and offset dikes. The apatite-hosted melt inclusions from the mineralized Whistle offset dike are enriched in Ni by up to 4 orders of magnitude compared to those melt inclusions trapped in the units stratigraphically higher in the SIC. This study provides the first in-situ determination of actual ore metal concentrations from early trapped melt of the SIC and trace element partitioning behavior between immiscible liquids in nature.

Acknowledgements

I would like to thank Dr. Jacob Hanley for his guidance and support throughout this project as primary supervisor and for the opportunity to present my research at two international conferences. I would also like to thank Dr. Doreen Ames (Geological Survey of Canada), Dr. Daniel Kontak (Laurentian University), and Dr. Sarah Gleeson (University of Alberta) for their support as my committee members and Dr. Alan Boudreau (Duke University) as my external supervisor. I would also like to thank Xiang Yang for assisting with SEM-EDS and Joe Petrus for assisting with LA-ICP-MS. I also want to thank my family for all their support and encouragement. And thank you to Ryan for his support, encouragement, patience, and for making sure I didn't starve when I lost track of time at school.

Table of Contents

Abstract	2
Acknowledgements	3
Table of Contents	4
List of Figures	6
List of Tables	8
Chapter 1: Introduction	9
1.0 Structure of thesis	9
1.1 Primary objective of thesis	9
1.2 Secondary objective of thesis	9
1.3 List of acronyms	11
Chapter 2: First melt inclusion study of the Sudbury Igneous Complex (Ontario, Canada): Evidence for two-liquid immiscibility and constraints on trace element distribution	12
Abstract	12
2.0 Introduction	15
2.0.1 Evidence for immiscibility in silicate melt systems: nature	17
2.0.2 Evidence for immiscibility in silicate melt systems: experimental	22
2.1 Regional Geology	24
2.1.1 Ore deposits of the SIC	30
2.2 Sample Preparation and Analytical Methods	31
2.2.1 Sample preparation	30
2.2.2 Scanning electron microscope (SEM)	32
2.2.3 Electron microprobe (EMP)	33
2.2.4 Laser ablation inductively coupled plasma mass spectrometry (LA-ICP-MS)	33
2.2.5 Data reduction and evaluation of data quality	34
2.2.6 Microthermometry	36
2.2.7 Colour CL	37
2.3 Results	37
2.3.1 Apatite petrography	37
2.3.2 North Range apatite chemistry	45
2.3.3 South Range apatite chemistry	45
2.3.4 REE zonation in apatite	48
2.3.5 Melt inclusion petrography	48
2.3.6 Melt inclusion major element chemistry	58
2.3.7 Melt inclusion trace element chemistry	58
2.3.8 Trace element partition coefficients between apatite and coeval melt	59
2.3.9 Trace element partition coefficients between Fe-rich and Si-rich melt	59
2.3.10 Microthermometry	66

2.3.10.1 TZG	66
2.3.10.2 Pele offset dike	71
2.4 Discussion	77
2.4.1 Major questions surrounding the SIC and its ores	79
2.4.2 Evidence for immiscibility in the SIC and comparison of melt-host relationships to other magmatic systems	79
2.4.2.1 Petrographic evidence for silicate liquid immiscibility combined with microthermometry of melt inclusions	79
2.4.2.2 Constraints on the timing of apatite saturation from trace element chemistry	83
2.4.2.3 Evidence for silicate liquid immiscibility and constraints on the timing of immiscibility from major element chemistry of melt inclusions	86
2.4.2.4 Evidence for silicate liquid immiscibility from trace element chemistry of melt inclusions	90
2.4.2.5 The onset of immiscibility in the SIC and subsequent differentiation of the melt sheet	91
2.5 Implications for the SIC evolution and timing of sulfide saturation	109
2.6 Conclusions	114
2.7 References	118
Chapter 3: Future work and limitations of the study	127
3.1 Limitations of Study and Suggestions for Future Work	127
3.2 Potential Exploration Criteria for the SIC	129

List of Figures

In Chapter 2

2.1 Geological map of the Sudbury Igneous Complex and Sudbury impact structure	26
2.2 Schematic cross section of the Sudbury structure, North Range, emphasizing the SIC and offset dikes studied	28
2.3 Representative photomicrographs of apatite morphologies in the North Range Main Mass and offset dikes using colour CL	38
2.4 SEM-BSE and transmitted light images of apatite in the North Range Main Mass and Whistle offset dike	40
2.5 Microphotographs (colour CL) and thin section sketch showing the distribution of apatite in the TZG and Whistle offset dike	43
2.6 Morphology of host phases of apatite as deciphered by colour CL	46
2.7 Zoned apatite grain from the TZG	49
2.8 Zoned apatite grain from the norite	51
2.9 Melt inclusions hosted in apatite from the North Range Main Mass and offset dikes	53
2.10 Element SEM maps of sulfide melt inclusions hosted in apatite from the Pele offset dike	56
2.11 Box and whisker plots of Kd values between apatite and melt inclusions in the Main Mass	60
2.12 Box and whisker plot of Kd values between apatite and melt in two quartz diorite offset dikes	62
2.13 Plot of the Kd values between Si-rich melt inclusions and Fe-rich melt inclusions in the Main Mass	64
2.14 Plot of Kd values between Si-rich and Fe-rich melt inclusions in the Pele and Whistle offset dikes	67
2.15 Microphotographs of microthermometric heating from 25° to 1295°C of an apatite-hosted melt inclusion from the TZG	69
2.16 Microphotographs of an Fe-rich melt inclusion from the Pele offset showing the effects along 8 step changes from thermometric heating from 30°C where it homogenizes at 1135°C	72
2.17 Photomicrographs of microthermometric heating of an apatite-hosted Fe-rich melt inclusion from 838° to 1207°C that homogenizes at 1207°C	74
2.18 Apatite trace element and REE chemistry comparing the North and South Range Main Mass normalized to primitive mantle	84
2.19 Apatite trace element chemistry of the mineralized Whistle offset dike and Barren Pele offset dike normalized to primitive mantle	87
2.20 Spider diagram plot showing the trace element chemistry of Si-rich melt	

inclusions normalized to primitive mantle	92
2.21 Spider diagram plot for trace element chemistry of the Fe-rich melt inclusions normalized to primitive mantle	94
2.22 Major element chemistry of apatite-hosted melt inclusions from the Main Mass And quartz diorite Pele offset dike plotted on an enlarged part of the pseudo-ternary Grieg diagram	96
2.23 Major element chemistry of apatite-hosted melt inclusions from the Main Mass TZG and Pele offset dike plotted as shaded fields on an enlarged part of the pseudo-ternary Grieg diagram with the binodal curve separating the one- and two-liquid fields	99
2.24 End-member immiscible liquids from experiments and from nature plotted on an enlarged part of the pseudo-ternary Grieg diagram with the binodal curve for basaltic liquids and for the SIC shown for comparison	102
2.25 Ratio of Fe: Si-rich liquids observed in the SIC defined by the Lever Rule	107
2.26 Plot of ablation time (s) versus count rate for element isotopes showing apatite-hosted melt inclusions in the Whistle offset dike	111

List of Tables – Appendix A (see attached)

In Appendix A

Table 2.1 Sample localities from the North Range of the SIC

Table 2.2 Major and REE chemistry of apatite from the North Range TZG, norite, and quartz diorite offset dikes and the South Range TZG (EMPA)

Table 2.3 LA-ICP-MS data for apatite from the North Range TZG, norite, and quartz diorite and the South Range mafic norite and TZG

Table 2.4 Major element chemistry (SEM and EMPA) of apatite-hosted melt inclusions from the TZG, norite, and quartz diorite offset dikes

Table 2.5 LA-ICP-MS for apatite-hosted melt inclusions from the North Range TZG, norite, and quartz diorite offset dikes

Table 2.6 Kd values between apatite and Fe-rich and Si-rich melt in the North Range TZG, norite, and quartz diorite offset dikes

Table 2.7 Results of microthermometry for apatite-hosted melt inclusions in the TZG and Pele offset dike

Table 2.8 Instrumental operating conditions for the by LA-ICP-MS at Laurentian University, Sudbury, Ontario

Chapter 1: Introduction

1.0 Structure of the thesis

This study has one main part and it is presented in Chapter 2. In this latter chapter the chemistry of apatite-hosted melt inclusions from the North Range Transition Zone Gabbro (TZG), norite, and quartz diorite offset dikes of the Sudbury structure of Sudbury, Ontario is presented. These results are used to then examine the major and trace element chemistry of the earliest formed melts in the Sudbury Igneous Complex (SIC) that were generated during meteorite impact into the Canadian Shield during the Paleoproterozoic. Chapter 1 briefly summarizes the main objectives of the study whereas Chapter 3 outlines the limitations encountered during this study and offers suggestions for possible future work in the study area.

1.1 Primary objectives of the thesis

The primary objective of this study is to characterize the major and trace element chemistry of apatite-hosted melt inclusions from the North Range Main Mass (the TZG and norite) and sublayer quartz diorite offset dikes of the Sudbury structure. Emphasis is placed on the chemical and petrographic characteristics of apatite from the base upwards in the SIC and also for samples from mineralized versus unmineralized offset dikes around the SIC.

1.2 Secondary objectives of thesis

The secondary objective of the thesis was to investigate the role of immiscibility as an important petrogenetic process in the evolution of the SIC melt sheet. Upon finding

that immiscible Si -and Fe-rich melt inclusions occur in apatite from all units studied, the potential implications of such immiscibility on both the petrogenesis and evolution of the SIC melt sheet was investigated in the following contexts: (i) timing of immiscibility in the melt sheet, (ii) formation of the granophyric cap overlying the norite and TZG (iii) trace element partitioning between Si- and Fe-rich immiscible melt pairs, and (iv) the potential influences on sulfide saturation of the melts in the presence of immiscible Si- and Fe-rich melts.

1.3 List of acronyms

The following is a list of commonly used terms throughout the thesis:

EMP – electron microprobe

LA-ICP-MS – laser ablation inductively-coupled mass spectroscopy

SEM – scanning electron microscope

SEM-BSE – scanning electron microscope back-scattered electron

SEM-EDS – scanning electron microscope energy-dispersive spectroscopy

SIC – Sudbury Igneous Complex

TZG – transition zone gabbro

CL – cathodoluminescence

Chapter 2: First melt inclusion study of the Sudbury Igneous Complex (Ontario, Canada): Evidence for two-liquid immiscibility and constraints on trace element distribution

Kathleen Watts^{1*}, Jacob Hanley¹, Joe Petrus², Daniel Kontak², Doreen Ames³, Ilya Veksler⁴

¹ *Dept. of Geology, Saint Mary's University, Halifax, Nova Scotia, Canada*

² *Dept. of Earth Sciences, Laurentian University, Sudbury, Ontario, Canada*

³ *Geological Survey of Canada (GSC), Ottawa, Ontario, Canada*

⁴ *GFZ Potsdam, Germany*

*corresponding author email address: kathleen.margot@gmail.com

Number of pages of text: 104

Number of figures: 26

Number of tables: 8

Abstract

The Sudbury Igneous Complex (SIC), Ontario, Canada, is the product of the impact of a massive bolide and it has been studied extensively due to its rich endowment in magmatic sulfide (Ni-Cu-platinum-group element) ore deposits. Interpretations of the source(s) of parental magma and the subsequent behaviour during evolution of the melt sheet remain controversial. In this study, analyses of primary melt inclusions hosted in cumulus apatite from the TZG, norite, and quartz diorite offset dikes of the SIC are used to decipher the thermochemical characteristics of the original melt sheet and trace element partitioning behaviour within the evolving melt sheet. Textural analyses of apatite in the SIC shows that apatite occurs as a cumulus phase in the Main Mass and quartz diorite offset dikes. Early saturation of apatite in the SIC is supported by microthermometric data that yields melt inclusion trapping temperatures in the TZG and quartz diorite offset dikes of ~1100° to 1200°C.

Apatite-hosted melt inclusions commonly display a negative crystal shape, occur parallel to the c-axis, and commonly occur within a central growth zone, suggesting primary origin. Coeval (co-entrapped) melt inclusion compositions show two distinct types: (i) Si-rich liquids that range in composition from tonalitic to granodioritic (60-70 wt % SiO₂, up to 11 wt % FeO) and (ii) Fe-rich liquids that range in composition from syenogabbroic to essexitic to alkali gabbroic (27-49 wt % SiO₂, 16-44 wt % FeO), determined by SEM-EDS and EMP analyses of opened, homogenized melt inclusions (apatite grains heated at 1100° to 1200°C for 3 hrs in a box furnace). These contrasting melt pairs may represent the products of immiscibility by either simple cooling of the superheated melt sheet or fractional crystallization.

The position of the bulk liquid composition of the SIC, the equivalent of the chilled margin of the quartz diorite offset dikes and least altered vitric bombs and blocks of the Onaping Formation, falls between immiscible melt pairs and in close proximity to the two-liquid field in the system leucite-fayalite-silica which suggests that the onset of immiscibility in the SIC was a consequence of simple cooling of the superheated melt sheet (~1700°C) and not liquidus crystallization which has been indicated to occur in other well studied basaltic layered intrusions.

In this study the proportion of Fe-rich to Si-rich liquid (~1:4.5) is in close agreement with the volume of granophyric liquid predicted from experiments modelling the fractional crystallization of the SIC melt sheet. However, these experiments have shown that fractional crystallization alone does not account for the observed 1:3 ratio of norite to granophyre along the North Range. Importantly, trapped (immiscible?) Si-rich liquid lower in the SIC must be taken into consideration. If one considers immiscibility as

a petrogenetic process for SIC melt sheet it may explain the large amount of granophyre in the SIC that has been so poorly understood in the past.

Trace element data, obtained by LA-ICP-MS analyses of single inclusions and surrounding host apatite are used to infer K_d values between apatite and the two melt types, and between coexisting melt types. ($K_d^{\text{Fe-rich melt/Si-rich melt}}$). The K_d values between immiscible melt pairs in this study show that the majority of trace elements partition evenly between Si- and Fe-rich liquid, with the incompatible elements (Hf, Zr, Nb, and Ta) showing a slight affinity for the Si-rich liquid and V and Co showing a slight affinity for the Fe-rich liquid in the TZG. Immiscible melt pairs in the norite have K_d values closer to one, with the exception of Co that prefers the Fe-rich melt. K_d values between immiscible Fe- and Si-rich liquid are also in close agreement to what has been found experimentally for melts with basaltic starting compositions. $K_d^{\text{apatite/melt}}$ values for both Si- and Fe-rich melt pairs show that the REE, Sr, Y are compatible in apatite, and As is weakly compatible or incompatible in apatite, whereas the following elements behaved incompatibly (in increasing order of incompatibility: Cr, Ni, Cu, Zr, Co, Cs, Ag, Nb, Hf, Ta, Rb).

Apatite-hosted melt inclusions from the mineralized Whistle offset dike are enriched in Ni by up to 4 orders of magnitude compared to those melt inclusions trapped in units stratigraphically higher in the SIC, reflecting loss of these metals to sulfide liquids prior to the crystallization of these units in the SIC. The absence of enrichment in Ni and Cu in melt inclusions from the unmineralized Pele offset dike suggests that proximity of trapped melt to ore bodies may influence their metal content. The results of this study have implications for our understanding of the petrogenesis of the SIC melt

sheet and the potential effects of sulfide saturation in the presence of immiscible Si- and Fe-rich liquids. Melt inclusion compositions may provide an important proxy for distance to ore bodies in the margin of the SIC. The study provides the first in-situ determination of actual ore metal concentrations from early trapped melt of the SIC and trace element partitioning behavior between immiscible liquids in nature.

2.0 Introduction

The 1.85 Ga Sudbury Igneous Complex (SIC), Ontario, Canada, is an igneous complex that represents the crystallized melt sheet that formed within a large impact crater at 1.85Ga (Dietz, 1964; Naldrett & Hewins, 1984, Mungall et al., 2004). The SIC has been extensively studied due to its rich endowment in magmatic sulfide ores (Ni-Cu-PGEs), but the nature and origin of the SIC melt sheet and its subsequent evolution still remain controversial. Our understanding of how the SIC melt sheet evolved is lacking due to the absence of information about the physical and chemical properties of the superheated melt sheet generated upon meteor impact. The study of melt inclusions, however, provides a way to understand the early events within the SIC since melt inclusions provide a snapshot in time and space of what the melt sheet looked like physically and chemically as the earliest rock forming minerals began to crystallize out of the melt sheet.

In recent years, notably over the past decade, the role of immiscibility in the petrogenesis of igneous rocks has sparked considerable controversy among igneous petrologists with the introduction of modern experimental methods (e.g., Veksler., 2004; Veksler *et al.*, 2006; Veksler *et al.*, 2007; Morse, 2008; McBirney, 2008; Philpotts, 2008;

Veksler *et al.*, 2008; Charlier & Grove, 2012). However, evidence for immiscibility occurrence in plutonic settings is limited and its implications for petrogenesis controversial. The first unequivocal evidence for immiscibility in a plutonic setting on Earth came from Si- and Fe-rich immiscible melt pairs found in melt inclusions of the Skaergaard complex (Jakobsen *et al.*, 2005; Jakobsen *et al.*, 2011), although immiscibility has been suggested to play a role in a multitude of conventionally studied layered intrusions on Earth (e.g., the Duluth complex, Ripley, 1998; the Sept Iles layered intrusion, Namur *et al.*, 2012; the Bushveld Complex, VanTongeren & Mathez, 2012). The SIC is unique from all conventionally studied layered intrusions in many aspects, most notably that its bulk starting composition is andesitic in nature and it started off as a superheated (~1700°C) impact melt sheet (Zieg & Marsh, 2005).

In this study, melt inclusions are used to provide constraints on crystallization processes and melt properties: (i) temperature and pressure upon trapping of melt; (ii) major and trace element chemistry that have implications for the original bulk melt composition; and (iii) major and trace element partition coefficients between immiscible Si- and Fe-rich liquids. These data are used to discuss the importance of immiscibility in the development of the SIC igneous stratigraphy of the Main Mass and ore-forming systems in the contact sublayer. Most notably lacking in the literature regarding immiscibility in melt inclusions is trace element data systematics. Such data are presented here for the first time for natural melt inclusions exhibiting immiscibility. In this study we demonstrate that two immiscible melts are present throughout the lower part of the SIC and based on these findings, various models are addressed pertaining to the original

melt composition and evolution of the igneous complex hosting the base metal ores of the Sudbury district.

2.0.1 Evidence for immiscibility in silicate-melt systems: nature

Immiscibility is a widely recognized process that is known to occur in many lunar basalts (e.g. Fagan *et al.*, 2003) and terrestrial volcanic basalts (e.g. Philpotts, 1982). However, there is an abundance of literature for basic plutonic settings where immiscibility is either not reported, or supporting evidence that immiscibility played any significant role is not found. Therefore, the variables that control the onset of immiscibility and the extent of the immiscibility field must be further evaluated in order to determine how extensive and how significant silicate liquid immiscibility is in nature.

Silicate liquid immiscibility was first proposed in the early development of petrology by Zirkel and Rosenbusch (1887) to explain how felsic and mafic rocks appear to be related but without the presence of intermediate compositions; hence is one of the oldest controversies in this field of study (Grieg, 1927; Bowen, 1928; Roedder 1951). The 1960s and 70s brought forth an abundance of literature in which silicate liquid immiscibility was proposed for natural rocks and a detailed reference list can be found in Roedder (1979). In more recent years, evidence for silicate liquid immiscibility in nature has been presented for a variety of settings on Earth: the Skaergaard intrusion, East Greenland (Jakobsen *et al.*, 2005; Jakobsen *et al.*, 2011); the North Mountain Basalt, Canada (Kontak *et al.*, 2002; Kontak & Dostal, 2010); the Sept Iles layered intrusion, Canada (Charlier *et al.*, 2011, Namur *et al.*, 2012b); and the Bushveld Complex, South Africa (VanTongeren &Mathez, 2012).

Definitive evidence for silicate liquid immiscibility in volcanic suites occurs as Fe-rich droplets embedded within Si-rich glassy matrix. In addition, various textures related to the unmixing process are persevered in the glassy mesostasis of volcanic and have been inferred as evidence for silicate liquid immiscibility. This aforementioned evidence for immiscibility has been found to occur in compositions ranging from olivine basalt to tholeiitic basalt to andesite (Philpotts, 1982). In regards to the textural evidence for immiscibility, Philpotts (1979) found in basalt from the Southbury basin of Connecticut, USA, an abundance of spheres of brown glass surrounded by clear glass in the mesostasis when viewed under reflected light. The same observation was noted by Kontak *et al.* (2002) in their study of the North Mountain Basalt. Though reflected light microscopy, not a widely used method, it is needed to observe features indicating immiscibility, it may provide an explanation as to much of the literature on basalt petrogenesis that either does not consider or does not show conclusive textural evidence for silicate liquid immiscibility.

The liquid line of descent pertaining to tholeiitic basalt is the most commonly studied and most widely debated for the Skaergaard intrusion, East Greenland (e.g. Hunter & Sparks, 1987; Brooks & Nielson, 1990; McBirney & Nasland, 1990; Thy *et al.*, 2006), whereby arguments have centered on whether the residual liquid follows the Fenner trend where it becomes Fe-rich at low SiO₂, or the Bowen trend, where it tends towards SiO₂ rich compositions at relatively lower FeO contents during fractional crystallization of a bulk liquid (Holness *et al.*, 2011). However, cumulates produced by the crystallization of a homogeneous melt followed by crystal sorting cannot be readily distinguished from the crystallization products of two immiscible melts, as these liquids

are in equilibrium and crystallize the same liquidus phases but in different proportions (Charlier *et al.*, 2011). Thus, this observation indicates that it is difficult to infer anything about immiscibility and its influence in the petrogenesis of magmatic systems without evidence from melt inclusions or experiments on fractionation of various bulk liquid starting compositions.

Melt inclusions provide the most unambiguous constraints on melt characteristics upon their entrapment. Thus, finding two chemically distinct types of melt inclusions, which occur primarily in cumulus mineral phases, in the upper zone gabbroic units of the Skaergaard Complex, (Jakobsen *et al.*, 2005, Jakobsen *et al.*, 2011) imply that these rocks must have crystallized from an emulsion of Si- and Fe-rich liquids (Holness *et al.*, 2011). It may also be plausible that previous evidence for both Fenner and Bowen trends in fact represents the contrasting compositions of these immiscible melt pairs (Humphreys, 2011). The trapping of emulsified liquid in melt inclusions furthermore suggests that immiscibility occurred on a sub- millimetre scale and that melt inclusions trapped stratigraphically higher in the sequence containing only end-member inclusions suggests that these globules eventually coalesced into larger pockets (Jakbosen *et al.*, 2011).

The discovery of immiscible melt pairs trapped as melt inclusions in the Skaergaard intrusion turned the focus on silicate liquid immiscibility in nature from the question of whether or not immiscibility occurs in plutonic settings to, instead, the timing of immiscibility, the factors contributing to the onset of immiscibility, and the implications for petrogenetic processes. The importance of immiscibility in the petrogenesis of basaltic intrusions has previously been largely overlooked, predominantly due to the lack of definitive evidence for immiscibility in nature and only due to its

manifestation on only a microscopic scale (Charlier *et al.*, 2011). These observations have, however, been nullified by the recent observation of large-scale, outcrop-sized pods and lenses of melanogranophyre in the Skaergaard Complex which have been demonstrated to be compositionally very similar to conjugate Si-rich immiscible melt (Jakobsen *et al.*, 2011). Further evidence for large-scale segregation of immiscible melts has also been presented for the Bushveld Complex (VanTongeren & Mathez, 2012) and the Sept Iles intrusion (Charlier *et al.*, 2011, Namur *et al.*, 2012) where immiscible liquids resulted in the crystallization of two types of ferrogabbros: (i) leucogabbro that crystallizes from the Si-rich melt and (ii) melanogabbro that crystallizes from the Fe-rich melt (Namur *et al.*, 2012). On a more intermediate scale, Kontak and Dostal (2010) present evidence for the mobilization of the Si-rich component of an unmixed basic silicate melt to form late-stage felsic pipes which crosscut the earlier, unfractionated parental basalt of the North Mountain Basalt.

Small scale textural evidence supporting the occurrence of immiscibility and speculation on its timing has recently been attributed to various late stage magmatic microstructures, as described by Holness *et al.* (2011) and based on their observations for the Skaergaard intrusion the textural and compositional record for the interstitial liquid in the crystal mush which accumulated on the margins of the magma chamber provides evidence for the presence of immiscible melts as well as its early onset. Non-reactive microstructures, i.e., those that appear to be in chemical equilibrium with surrounding mineral grains, include interstitial granophyre, which is understood to form by solidification of highly evolved silicic liquids. However, recently described non-reactive ilmenite intergrowths that have been found to occur in close spatial association with

granophyre suggests the presence of multiply saturated liquids in chemical equilibrium with their bounding primocryst phases, and in addition, their contrasting chemical compositions suggest that these two types of late stage microstructures represent the solidified remnants of highly evolved interstitial silicate liquids that have undergone immiscibility (Holness *et al.*, 2011).

A detailed study of two apatite bearing ferrogabbro horizons of the Sept Iles intrusion, Quebec, Canada by Namur *et al.* (2012) presented textural evidence and used fractionation modelling of liquid lines of descent, based on bulk rock mineral data to conclude that, whereas one of these horizons crystallized from a homogeneous melt, the other formed by solidification of immiscible Si- and Fe-rich melts. In this study, fractionation modelling suggests that whether tholeiitic basalt enters the two-liquid field or crystallizes as a homogenous melt depends on minor differences in the bulk liquid composition. Furthermore, whether large-scale segregation of immiscible melts occurs may depend on magma chamber size, with large-scale segregation possibly favouring larger chambers (Namur *et al.*, 2012), but this remains unclear. Philpotts (1979) reported that the size and abundance of the brown Fe-rich droplets appear to be dependent on the spatial relation of certain minerals (i.e. larger droplets surrounded completely by plagioclase laths and more frequent smaller droplets found in close spatial relation to pyroxene grains). This phenomenon is only clearly noted under reflected light, which may account for why such immiscible droplets are not reported in other studies on basalts.

2.0.2 Evidence for immiscibility in silicate-melt systems: experimental

Early experimental work on immiscibility in silicate melts for a number of binary and ternary systems showed that for silicate melts immiscibility occurred only at very high temperatures ($\sim 1700^\circ\text{C}$) (Greig, 1927). Later work by Roedder (1951) showed, however, that in the system $\text{K}_2\text{O}-\text{FeO}-\text{Al}_2\text{O}_3-\text{SiO}_2$ a low temperature (i.e. $\sim 1150^\circ\text{C}$) immiscibility field exists in dry silicate systems whereas in the system $\text{FeO}-\text{Al}_2\text{O}_3-\text{SiO}_2$, the addition of K_2O is required for the presence of this low temperature field; the effect of adding other components, such as H_2O and Na_2O_3 , remained unknown at this time. The implications for silicate liquid immiscibility in nature remained, however, largely ignored until 1954 when Norman Holgate presented evidence for immiscibility based on the presence of glassy rims (i.e. former melt) surrounding quartzite xenoliths, as discussed by Roedder (1957), who strongly refuted this interpretation and stated that it could be explained by other magmatic processes. After nearly 30 years, further work in the system $\text{K}_2\text{O}-\text{FeO}-\text{Al}_2\text{O}_3-\text{SiO}_2$ by Roedder (1978) indicated that a basaltic bulk composition could unmix to form two immiscible silicate liquids by either simple cooling or by cooling and crystallization. Although the addition of alkalis and alumina, in the form of leucite, eliminates the high temperature immiscibility field, further addition also makes the lower temperature immiscibility field ($1100-1270^\circ\text{C}$) relevant.

Immiscibility must occur at a relatively early stage in the crystallization of a basic magma if the process is to have petrogenetic significance and, as noted by Philpotts (1976), the alkali magmas may undergo the necessary enrichment in alkalis to reach the immiscibility field early in its crystallization. In recent years, the high temperature centrifuge (e.g. Veksler *et al.*, 2006; Veksler *et al.*, 2007; Veksler *et al.*, 2008), has been

employed in order to constrain the process and implication of for silicate liquid immiscibility in tholeiitic basalt petrogenesis. Experimental studies by Veksler *et al.* (2006) placed the onset on immiscibility of basaltic magma at temperatures near 1100°C which suggested that immiscibility could in fact be occurring early enough to play a significant role during the early stages of fractionation. These results sparked considerable debate (e.g. Philpotts, 2008; McBirney, 2008; Morse, 2008; Veksler *et al.*, 2008,) and it was concluded by Veksler *et al.* (2010) that the temperatures previously reported for the early onset of immiscibility was erroneously high and that immiscibility had occurred in a metastable state.

The recent experiments by Charlier and Grove (2012) provided evidence that immiscibility occurs only at temperatures of 1000° to 1020°C and is independent of the starting composition of the basalt. These authors showed that whether or not a bulk liquid surpasses the binodal curve (the term solvus is reserved for solid solutions) into the field of immiscibility depended on small variations in the bulk liquid that than whether the magma follows the trend of Fe-enrichment or of Fe-depletion and Si-enrichment, that is, immiscibility will be reached under the right chemical conditions. The composition of the homogeneous melt at the point where the immiscibility field is reached will define the extent of compositional variation of the immiscible melts. Those melts that experience significant Fe- or Si-enrichment prior to unmixing produce immiscible pairs with extensive compositional separation, in contrast to melts that evolve to a composition near the closure of the binodal curve and produce immiscible pairs with narrow compositional separation (Charlier & Grove, 2012).

2.1 Regional Geology

The 1.85 Ga (Krogh *et al.*, 1984) Sudbury event occurred when a bolide body struck the continental margin of Nuna, Earth's first supercontinent and created the Sudbury structure (Dietz, 1964; Naldrett & Hewins; 1984; Ames *et al.*, 2008). The impact created a transient crater with an original rim diameter of ~200-300 km and 1-6 km depth which was wholly or partially occupied by a melt sheet of andesitic composition (Grieve *et al.*, 1991; Mungall *et al.*, 2004). The melt sheet, generated due to near instantaneous melting of the target rocks at >1700°C (Zieg & Marsh, 2005), subsequently crystallized the Sudbury Igneous Complex (SIC), which was itself capped by fallback breccia related to the impact (the Onaping Formation). The variably-brecciated basement rocks, a consequence of the impact and re-equilibration of the footwall rocks to the SIC, were cut by breccia bodies (Sudbury Breccia) and dikes of impact melt (offset dikes) (Grieve *et al.*, 1991). The offset dikes formed as a result of magma being injected into dilated concentric and radial fracture zones when the temperature of the footwall rocks was elevated (Grant & Bite, 1984) with the infill melt representing the original quenched melt composition of the SIC (Lightfoot *et al.*, 2001, Ames *et al.*, 2002; Pope *et al.*, 2004). Underlying the SIC is target rock breccia (Footwall Breccia), which was thermally metamorphosed by the impact generated melt sheet (Footwall Breccia). Finally, in direct contact with the SIC is the SIC sublayer, a basal fine grained unit of noritic composition that is heavily charged with lithic debris (Grieve, *et al.*, 1991).

The Sudbury structure straddles the boundary of two geological provinces, the Superior and Southern (Card *et al.*, 1984; Dressler, 1984; Ames & Farrow, 2007) (Fig.

2.1). The Northern Superior Province contains Neoproterozoic granitic rocks and the high grade Levack gneiss complex which underlay the North Range of the Sudbury structure. To the south is the South Range where the Superior Province contains Early Proterozoic metasedimentary and metavolcanic rocks that are overlain by Huronian greywackes and feldspathic quartzites. The SIC is also addressed in terms of its North Range or South Range, as these areas differ in their geochemical and petrological features (Naldrett *et al.*, 1970; Gasparri *et al.*, 1972; Therriault *et al.*, 2002). It is unlikely that the melt sheet produced by a large-scale impact as the SIC retained any heterogeneity between the North and South Ranges, as initial superheated low viscosity melt products would have homogenized during collapse of the transient crater within minutes of impact. However, whereas trace element ratios show minimal variation in the Main Mass, isotopic evidence revealed significant differences between the North and South Ranges. This heterogeneity is very likely attributed to continuous melting of footwall rocks, fallback material, and entrained clasts post-impact by a superheated homogeneous melt sheet (Ivanov & Deutsch, 1999; Darling *et al.*, 2010b).

The SIC is elliptical in shape and is made up of the Main Mass, covering an area of ~60 x 30 km (Naldrett & Hewins; 1984; Grieve *et al.*, 1991; Ames *et al.*, 2008). The SIC Main Mass, from its base to top, consists of: (i) the concentric and radial quartz diorite offset dikes, (ii) the discontinuous zone of the noritic inclusion rich sublayer, (iii) quartz-rich norite of the South Range and orthopyroxene-rich mafic norite of the North Range, (iv) the transition zone gabbro (TZG), and (v) the granophyre and plagioclase-rich granophyre (Naldrett & Hewins; 1984; Lightfoot *et al.*, 1997a) (Fig. 2.2). The offset dikes, traditionally termed “quartz diorite” range in composition from between quartz

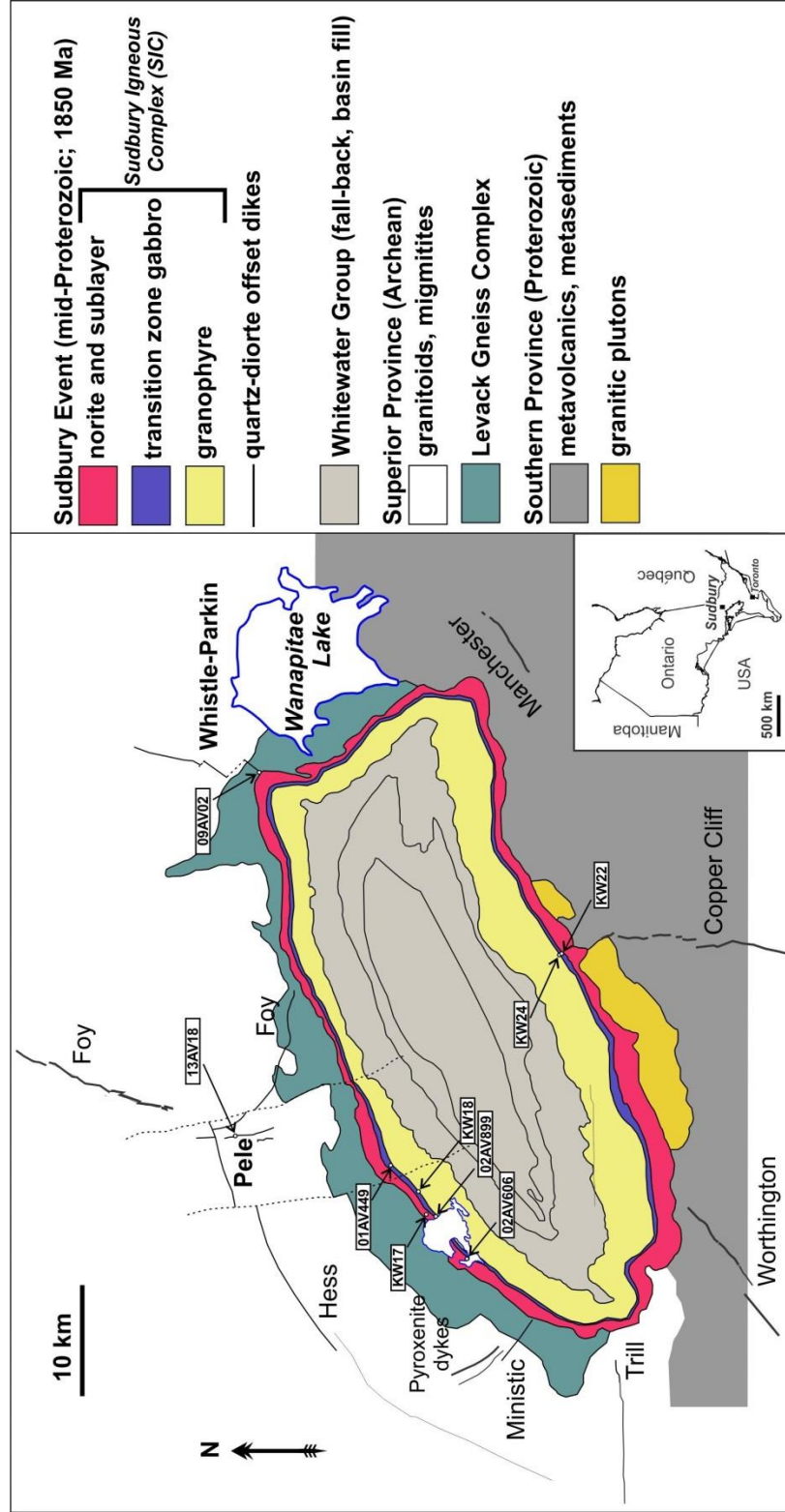


Figure 2.1: Geological map of the Sudbury Igneous Complex and Sudbury impact structure. General map of the SIC and surrounding area with sample localities from the North Range norite and TZG, the South Range norite and TZG, and the Whistle and Pele offset dikes.

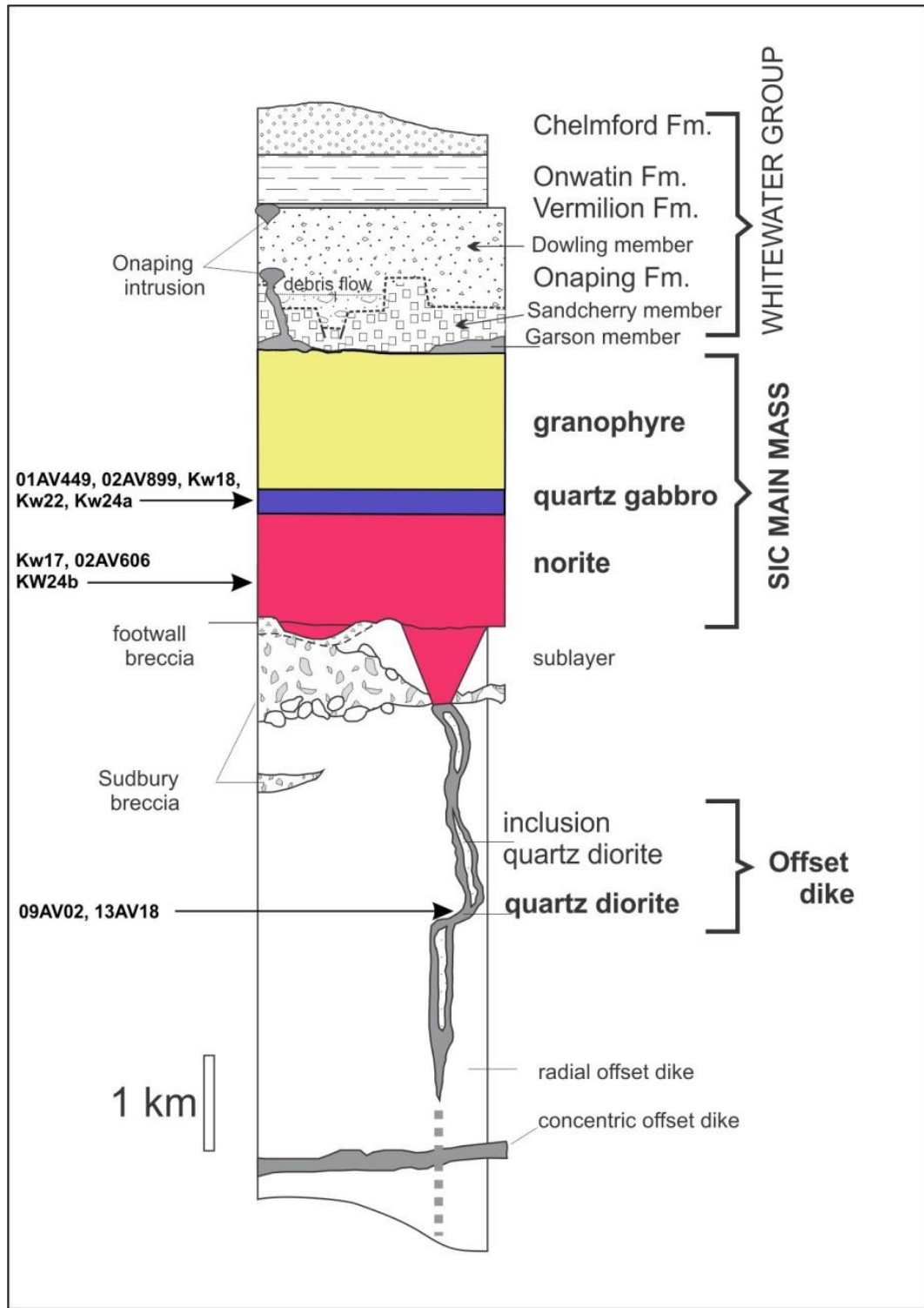


Figure 2.2: Schematic cross section of the Sudbury structure, North Range, emphasizing the SIC and offset dikes studied. The units included in this study are shown in bold (modified from Ames *et al.*, 2008).

monzodiorite through granodiorite to tonalite (Ames & Farrow, 2007) and can be subdivided by their structural occurrence into three types: (i) radial offset dikes that begin at embayments of the Footwall contact of the Main Mass and extend for several kilometres into the surrounding country rocks; (ii) radial or concentric offset dikes that occur as continuous to semi-continuous dikes of quartz diorite and strike parallel to the lower contact of the Main Mass in zones of massive Sudbury Breccia; and (iii) discontinuous quartz diorite that occur within embayment structures and filled with mainly sublayer rocks (Grant & Bite, 1984).

2.1.1 Ore deposits of the SIC

Ore deposits associated with the SIC occur as three main types and are based on their interrelated environments, (i) contact, (ii) offset, and (iii) footwall deposits. All deposits contain Ni-Cu-PGE, however the footwall deposits have elevated and locally very high PGE contents.

The contact deposits are host to over 50% of the historical Sudbury resource. These deposits are typically pyrrhotite-rich, Ni-Cu ores that are hosted within sublayer norite and/or Footwall Breccia within depressions or embayments at the base of the SIC at or near the contact with NeoArchean (North Range) or Paleoproterozoic (South Range) basement rocks. The contact type deposits are rich in Ni-Ir-Rh, which are hosted by a sulfide and oxide mineral assemblage of pyrrhotite, pentlandite, and chalcopyrite with minor magnetite and pyrite.

Offset deposits that occur within the offset dikes are host to ~25% of the historical Sudbury resource. Mineralization occurs within local inclusion bearing quartz diorite,

which is interpreted as resulting from a secondary pulse of magma. The offset ores become more PGE-, Cu-, and Au-rich with increasing distance from the SIC and are dominated by pyrrhotite and less abundant pentlandite and chalcopyrite.

The South Range Breccia belt is host to ~15% of the historical Sudbury resource. It ranges in width from 100 m to more than 1 km and is more than 45 km in length and is comprised of Sudbury breccia. The Frood-Stobie mine of the South Range breccia belt has an upper domain of Ni mineralization (pyrrhotite) and a lower domain of Cu-PGE mineralization, termed the “siliceous zone in the South Range breccia belt”.

Footwall type deposits are host to less than ~10% of the historical Sudbury resource. They are hosted in Sudbury Breccia and have more recently been referred to as “Cu-Ni-PGE” systems. These systems are subdivided into the dominant “sharp-walled” and less common low sulfide end-members, whereas deposits that contain both types are termed “hybrid” (Ames & Farrow, 2007 and authors therein; Coats & Snajdr, 1984; Farrow & Watkinson 1997; Farrow & Lightfoot, 2002; Farrow *et al.*, 2005; Golightly, 1994; Lightfoot & Zotov, 2005; Mungall *et al.*, 2002; Mungall *et al.*, 2005; Mungall *et al.*, 2007; Mungall & Naldrett, 2008).

2.2 Sample preparation and analytical methods

2.2.1 Sample Preparation

Samples from the North Range of the SIC include 3 samples of TZG, 1 sample of norite, and 2 samples of quartz diorite offset dikes. Nine samples from the South Range gabbro and norite were also collected (Table 2.1, Appendix A). All samples were

processed for apatite separates at Activation Laboratories Inc. and at the University of Toronto. An aliquot of apatite grains from each sample of the North Range was placed in a ceramic crucible, heated in a Thermolyne 4800 muffle furnace to 1100° to 1200°C for 3 hours and quenched by removing the crucible from the furnace. Based on the proceeding, two types of apatite separates were then prepared for analysis: (i) grain mounts containing unhomogenized melt inclusions on glass slides using a thin film of CrystalBond epoxy; and (ii) grain mounts, some containing unhomogenized and others homogenized melt inclusions, in 1 inch diameter pucks using a BUEHLER SimpliMet 1000 Automatic Mounting Press in transcoptic powder which were taken to 180°C and 275 bars. Bulk rock samples were also cut into blocks and sent to Vancouver Petrographics Ltd., Langley, BC, and prepared into 30 µm thick polished thin sections for EMP analysis and petrographic study.

2.2.2 Scanning electron microscope (SEM)

Polished thin sections were analysed at the Geological Survey of Canada, Ottawa, Ontario, with an Oxford INCA 450 SEM-EDS. A cathodoluminescence detector (CL) attached to the SEM-EDS system was used to map the distribution of apatite and melt inclusions and detect zonation within apatite crystals. Polished thin sections and grain mounts were analysed semi-quantitatively to determine major element compositions of exposed melt inclusions using a Leo 1450 VL SEM-EDS system operated at 5 nA current and 25 keV accelerating voltage at Saint Mary's University, Halifax, Nova Scotia. The data were processed using INCA software.

2.2.3 *Electron microprobe (EMP)*

Apatite in grain mounts were polished using 1000 grit sandpaper before smoothing the surface using oil based diamond paste (1 μm) in order to expose glassy melt inclusions. The homogenized melt inclusions were then analyzed for major elements and halogens and apatite was analysed for major elements, rare earth elements (REE), and halogens. Total oxide concentration of melt inclusions was used for an H_2O total for data reduction of LA-ICP-MS trace element analysis. The instrument used was a JEOL 8200 electron microprobe at Dalhousie University, Halifax, Nova Scotia, and operated at an accelerating voltage of 20 kV, a beam current of 5 nA, and variable beam size (to assess volatile migration). On-peak count time for each element was 10s.

2.2.4 *Laser ablation inductively coupled plasma mass spectrometry (LA-ICP-MS)*

A laser ablation inductively coupled plasma mass spectrometry (LA-ICP-MS) was used to determine the abundance of trace elements in apatite and of homogenized and unhomogenized melt inclusions using a Resonetics RESolution M50 laser probe (Ar-F Excimer laser) operated in dual detector mode at Laurentian University, Sudbury, Ontario. The same LA-ICP-MS system was used to assess variations in the minor and trace element chemistry along visible growth zones in apatite using the rastering mode and a repetition rate of 5 Hz and a fluence of 6 J/cm^2 . The two samples, KW18 and 02AV606 were mapped by using a laser spot size of 13 μm and a speed of 6 $\mu\text{m}/\text{s}$. The LA-ICP-MS operating conditions can be found in Table 2.8, Appendix A.

2.2.5 Data reduction and evaluation of data quality

Data reduction for melt inclusions analysed by LA-ICP-MS was done using SILLIS (Guillong *et al.*, 2008). Through SILLIS the melt inclusion traces and major element chemistry is distinguished from that of the host apatite. SILLIS also does a “drift correction” for the LA-ICP-MS. An internal standard of CaO (wt %) determined by EMP analyses of apatite in each sample, was used to calculate the other elements present. Two constraints need to be known about the melt inclusions being analysed and this presented an issue given that two different melt compositions occur. It was found that EMP totals from melt inclusion analyses averaged ~95% and so a “total oxides” constraint was also utilized. The second constraint used was a “matrix-only tracer” in which lanthanum (La) was used, as La showed the highest incompatibility in the melt relative to the apatite host phase. Minimum $K_d^{\text{apatite/melt}}$ values range from 13 to 25. The LA-ICP-MS files were brought into SILLIS where sections of background, host, and host + melt are highlighted along an interval with the y-axis being elements (in counts per second) and the x-axis being time taken for background and ablation of sample (in seconds). Data reduction for LA-ICP-MS raster maps for apatite used the Iolite software.

Evaluation of analytical accuracy and precision for transient LA-ICPMS signals is challenging since no certified synthetic melt inclusion reference standards are available. However, some statements can be made concerning the quality of the data.

With respect to the accuracy of trace element analyses in melt inclusions, repeated analyses of synthetic glass standards at the Laurentian University laser ablation ICP-MS facility as secondary QC standards (BHV02 from USGS; ATHO from MPI-DING), quantified using NIST610 routinely yield concentrations better than within 15% relative

of expected concentrations (Petrus, personal communication). Analytical precision cannot be readily evaluated since the method is destructive, however, two possible strategies are considered. First, when different integration windows through homogenized (glassy) melt inclusions are quantified, adjacent intervals of inclusion yield analytical reproducibility better than 5% relative. Similarly, when melt inclusion results from a single sample are compared (and assumed to contain the same liquid, for melt end-member compositions) reproducibility of melt compositions within single samples is high. However, these results are measures of melt homogeneity at various scales rather than true (external) precision.

With respect to the accuracy of major element analyses in melt inclusions, comparison of analytical results yielded from SEM/EMP for homogenized inclusions with data from LA-ICP-MS shows that all major elements (with the exception of FeO, MgO, and MnO) yield concentrations within 25% (relative) of each respective method. For reasons that are unclear at this time, and likely related to the low concentrations in the standard NIST610 glass, FeO, MgO, and MnO are up to 70% higher in the LA-ICP-MS analyses of equivalent inclusions analysed by SEM/EMP. For these reasons it is our preference to utilize the SEM/EMP data for major elements and the LA-ICP-MS data for trace elements. For precision of major element analyses, only a similar approach as that stated above for trace elements can be employed for the LA-ICP-MS method. For SEM/EMP analyses, repeated analyses of single points within homogenized melt inclusions yielded reproducibilities in the quantified EDS spectra of better than 2% relative.

Analytical uncertainties in the SEM/EMP analyses (in the total wt% oxides excluding H₂O, the CaO composition of the host apatite) and uncertainty introduced by assuming La to be the matrix-only tracer also impact the overall uncertainty in major and trace element analyses. Uncertainties in the host composition (which was selected for all data reduction as a constant value of CaO for each respective sample; norite [sample KW17: 55.60 wt%], TZG [sample 01AV449: 55.21 wt%; sample 02AV899: 53.48 wt%; sample KW18: 55.80 wt%] and for the offset dikes values were taken from the Main Mass; Whistle offset dike [sample 09AV02: 53.48 wt%], Pele offset dike [55.48 wt%]) and analytical total (value used 95%, actual range: TZG [89.14 to 94.90 wt%]), by SEM/EMP are no larger than a few % which would impact the resulting melt inclusion data reduced in SILLS proportionally. With respect to La as the matrix-only tracer, the actual ratio of $La_{\text{host}}/La_{\text{inclusion}}$ is on the order of ~100 (i.e., 0.2 wt% La in apatite vs. 20 ppm expected for felsic liquids; not quantifiable). Uncertainties in melt composition resulting from this unmixing procedure will be larger for elements that show less compatibility in the melt phase.

2.2.6 Microthermometry

Microthermometry of melt inclusions was conducted using a Linkam TS1500 heating stage with sapphire plates for heating. The stage is mounted on BX53 microscope with a Q imaging colour video camera. Heating rates varied between 10°C/min and 100°C/min, and a flow rate of 40 ml/min of argon gas was used to prevent oxidation of melt inclusions and their apatite host during heating. The error associated with the absolute temperature is ± 2 °C based on monitoring of fixed temperature stability. Pure

Ag, Au, and Cu metals were used as standards to calibrate the stage by measuring their melting points and comparing them against accepted values.

2.2.7 Colour CL

Section 09AV02 was analysed on a Reliotron-based CL under which photos were taken with a vacuum gauge pressure that read between 79 and 82 millitorr, a beam current fluctuation between 40 and 66 microamps, a voltage of 12 kV, a beam focus of 28, and a current limit set at 2 ma. Photos were taken using the Empix program and an Optronics camera. Section 01AV449 photos were taken with a vacuum gauge pressure read between 75 and 80 millitorr, a beam current fluctuation between 57 and 64 ma, a voltage of 12 kV, and a current limit set at 2 ma. Sections KW17 and 13AV18 were taken at 13 kV and 70 nA.

2.3 Results

2.3.1 Apatite petrography

Apatite in thin section can be found as 3 distinct morphological types in the TZG, norite, and offset dikes: (i) hexagonal cross section, (ii) elongate hexagonal, and (iii) needle, as demonstrated by CL images for the Main Mass and offset dikes (Fig. 2.3). Apatite petrography is also shown by SEM-BSE images for the TZG, norite, and Whistle offset dike (Fig. 2.4). Apatite is rare in the norite compared to the TZG and the offset dikes and so thin sections were examined by SEM-EDS and transmitted light microscopy. In the norite, needle type apatite is common and commonly cross cuts quartz

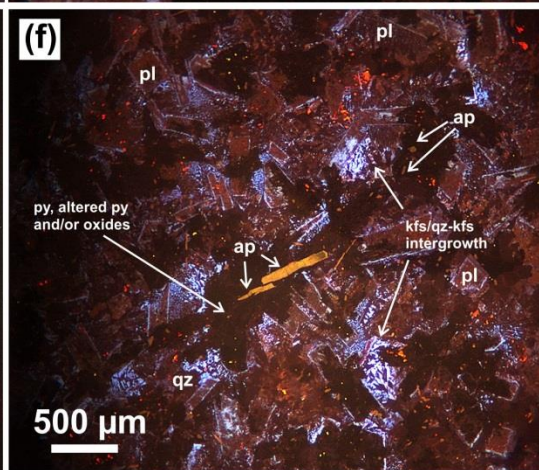
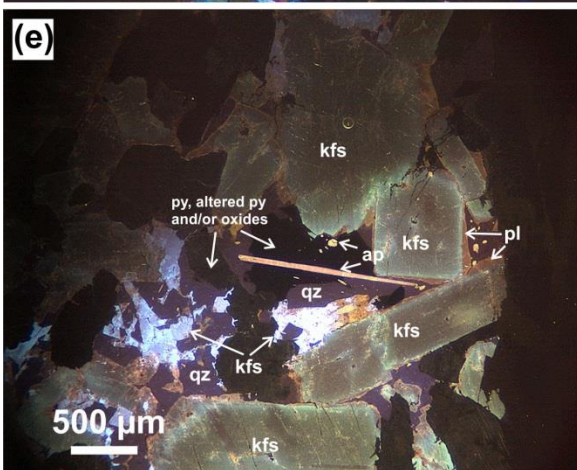
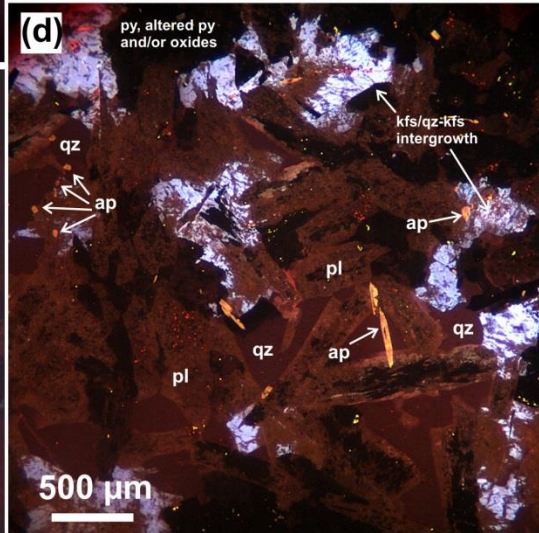
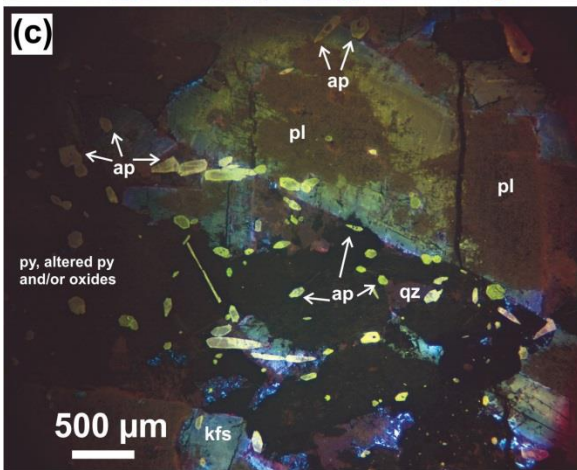
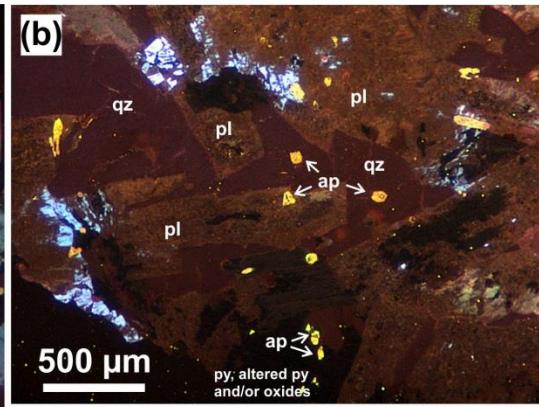
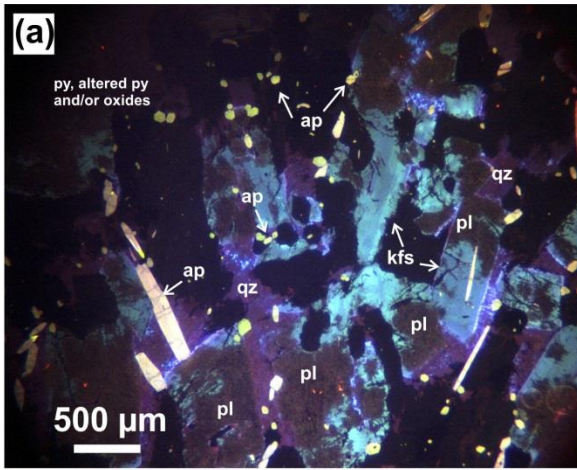


Figure 2.3: Representative photomicrographs of apatite morphologies in the North Range Main Mass and offset dikes using colour CL. This image demonstrates the different morphologies of apatite found in the Main Mass and offset dikes of the Sudbury structure. (a) Shows elongate hexagonal apatite cross cutting all phases and needle type apatite in the centre of plagioclase or dispersed in interstitial phases, 01AV449. (b) Shows the smaller volume of apatite in in the Whistle offset dike as primarily small hexagonal cross section type apatite, 09AV02. (c) Shows that hexagonal apatite can be found clustered in high volume percentages in interstitial material, along with occasional needle type, 01AV449. (d) Shows that whereas apatite is less abundant in the Whistle offset dike, all three morphologies are still present, 09AV02. (e) Shows the common needle apatite in the norite that cross cuts multiple phases and also small hexagonal apatite hosted in quartz and opaque and/or altered orthopyroxene phases, KW17. (f) Shows apatite in the Pele offset dike that occurs mainly as very small hexagonal apatite dispersed in opaque and mafic phases, whereas rare apatite is found as large elongate hexagonal and hosted in mafic phases. Colour assignments for mineral phases shown in colour cathodoluminescence images are as follows: tabular green-green brown lathlike crystals = plagioclase; bright blue alteration = potassium feldspar; purple = quartz; grey-black = pyroxene, altered pyroxene phases, oxides; pink is carbonate alteration. Abbreviations are: ap = apatite, pl = plagioclase, kfs = potassium feldspar, py = pyroxene, qtz = quartz.

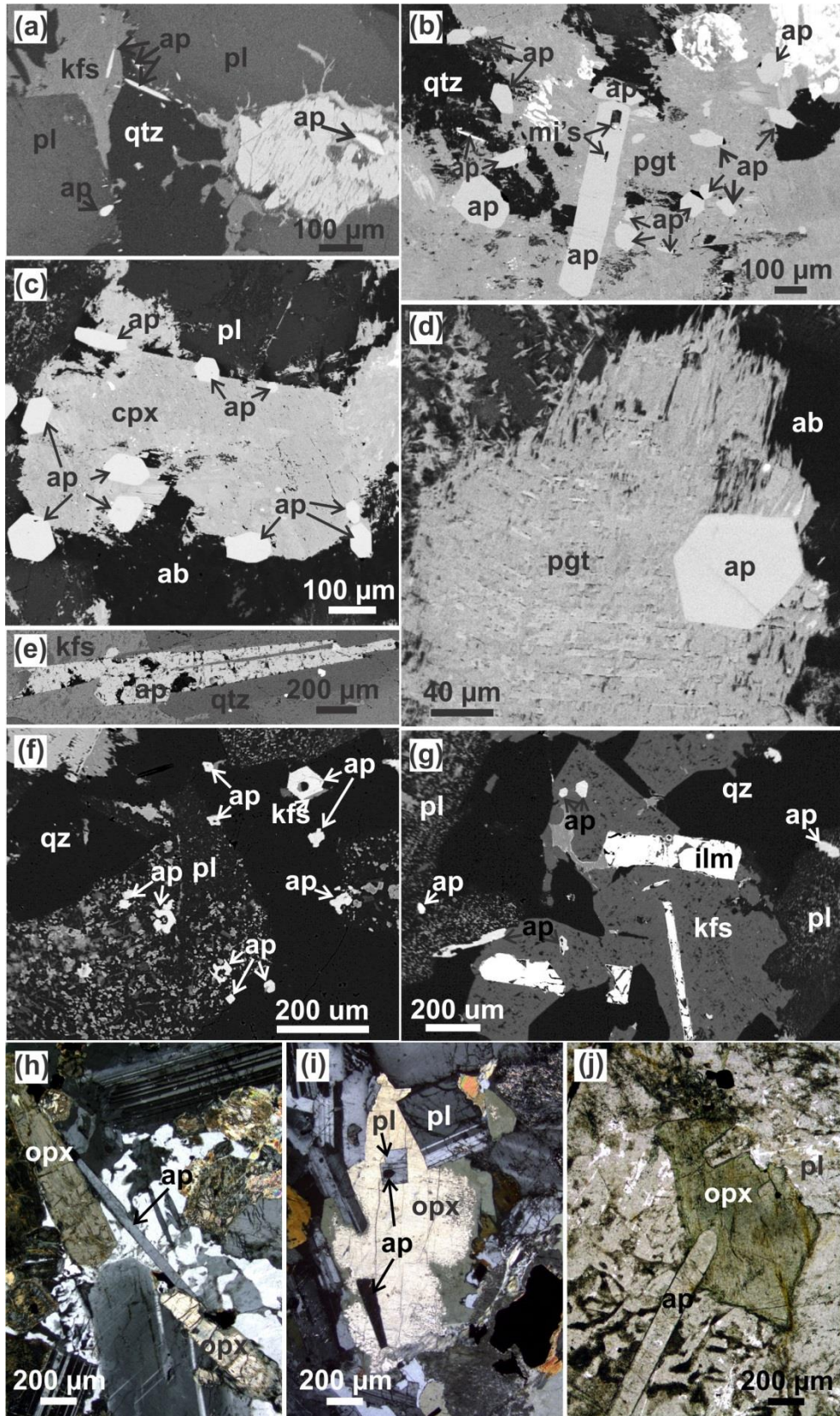


Figure 2.4: SEM-BSE and transmitted light images of apatite in the North Range Main Mass and Whistle offset dike. (a) Shows apatite enclosed in quartz, potassium feldspar, and plagioclase and also demonstrates the common needle morphology of apatite in the norite. In the TZG euhedral apatite crystals are poikilitically enclosed in pigeonite and clinopyroxene (b, c, and d). (e) Shows large apatite cross cutting quartz and potassium feldspar from the norite. (f-g) Shows apatite from the Whistle offset dike that is commonly enclosed in inclusion rich plagioclase or as overgrowths on plagioclase. (h, XPL) shows a large needle apatite touching the grain boundary of two separate cumulus orthopyroxene grains. (i, XPL) Shows an apatite grain that is hosted in plagioclase that is poikilitically enclosed in interstitial orthopyroxene and another apatite grain that is enclosed in interstitial orthopyroxene. (j, PPL) Shows a large needle apatite that is lodged in a cumulate orthopyroxene grain. Abbreviations are: ap = apatite, pl = plagioclase, kfs = potassium feldspar, ab = albite, cpx = clinopyroxene, qtz = quartz, pgt = pigeonite, ilm = ilmenite, opx = orthopyroxene, opq = opaque. PPL = plane polarized light and XPL = cross polarized light.

and plagioclase and occurs as very small (>20 µm) grains embedded in oxides or in interstitial phases. Transmitted light petrography of least altered norite show that at least some apatite is associated with orthopyroxene (Fig. 2.4, h and j) or hosted in cumulus plagioclase that is enclosed in intercumulus orthopyroxene (Fig 2.4, i).

A cartoon demonstrating how the apatite host phases were chosen using colour CL petrographic images is shown in Figure 2.5. Apatite can be subdivided into 11 types based on the host mineral phase in the TZG, norite, and Pele and Whistle offset dikes: (i) hosted in quartz; (ii) hosted in plagioclase; (iii) hosted in pyroxene and pyroxene alteration products (i.e chlorite, amphibole) and/or cumulus magnetite; (iv) cross cutting plagioclase and quartz; (v) hosted in granophyre texture (i.e., quartz-potassium feldspar intergrowth); (vi) cross cutting quartz and pyroxene and pyroxene alteration products and/or cumulus magnetite; (vii) cross cutting plagioclase and pyroxene and pyroxene alteration products and/or cumulus magnetite; (viii) cross cutting quartz granophyric texture and pyroxene and pyroxene alteration products and/or cumulus magnetite; (ix) cross cutting quartz, plagioclase rimmed with potassium feldspar, and pyroxene and pyroxene alteration products and/or cumulus magnetite (in the Pele offset is cross cutting mafic phases and quartz-potassium feldspar intergrowth); (x) cross cutting quartz, plagioclase, and pyroxene and pyroxene alteration products and/or cumulus magnetite; (xi) cross cutting plagioclase and potassium feldspar alteration along plagioclase grain boundary and quartz or crosscutting plagioclase with quartz-potassium feldspar intergrowth.

Apatite is very abundant in the TZG (~5 %) and appears in BSE and plane polarized images as clean homogenous grains free from any mineral inclusions. In the

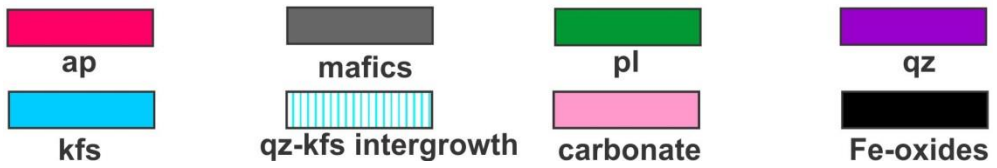
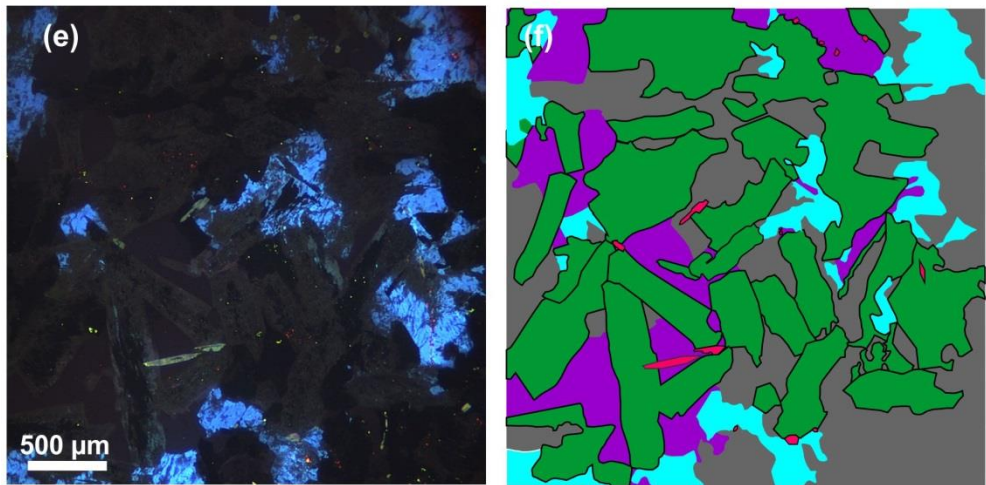
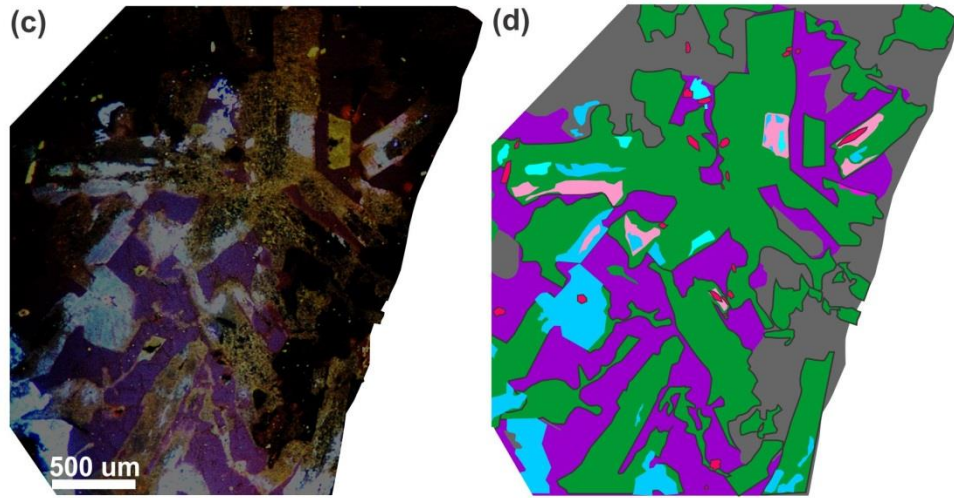
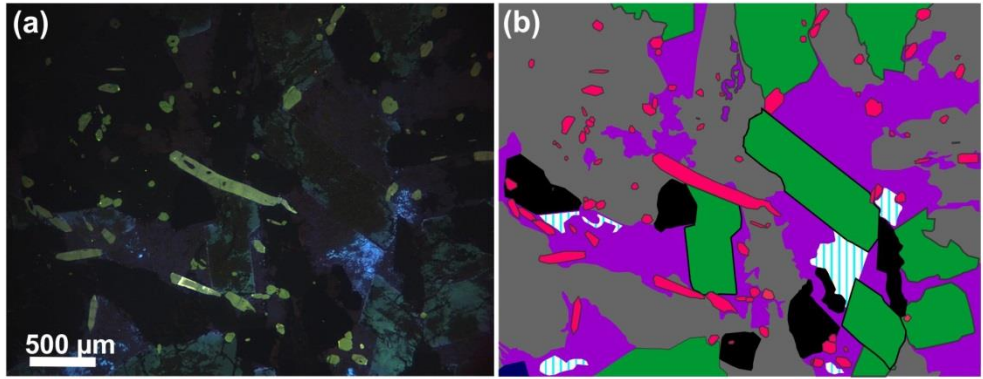


Figure 2.5: Microphotograph (colour CL) and thin section sketch showing the distribution of apatite in the TZG and Whistle offset dike. (a, b) is apatite from the TZG and (c-f) is apatite from the leucocratic quartz diorite Whistle offset dike. See previous figure (2.4) for mineral abbreviations.

norite, apatite is less abundant (~2 %) and commonly contains small mineral inclusions, and abundant fluid inclusions. In the Whistle offset dike apatite is also less abundant (~1 %) and is hosted in all mineral phases and cross cuts several mineral phases. Fluid inclusions are abundant and can be found in all three types of apatite. The occurrence of apatite in host phases for the Main Mass and offset dikes is summarized as a bar graph in Figure 2.6.

2.3.2 North Range apatite chemistry

Apatite analyses by EMP from the North Range TZG and norite indicate a fluorine rich composition (average ~3wt % Table 2.2, Appendix A). Trace element chemistry of apatite from North Range TZG, norite, and quartz diorite offset dikes by LA-ICP-MS can be found in Table 4, Appendix A. In the Main Mass, the LREE (La, Ce, Pr, Nd) are highest in apatite from the norite and decrease into the TZG. The LREE (La + Ce) concentrations in the Whistle offset dike are comparable to apatites in the norite and LREE (La + Ce) concentrations in apatite in the Pele offset dike are comparable to that observed in cumulus apatite from the TZG. The concentrations of Cu (~17 ppm) and As (~20 ppm) are highest in apatite from the Whistle offset dike (~8 ppm). The concentration of As in apatite in the Main Mass increases from ~4 ppm in the norite to ~9 ppm in the TZG (Table 2.3, Appendix A).

2.3.3 South Range apatite chemistry

Sample KW24 (South Range norite) was analysed by EMP and is F rich (average ~3%) (Table 2.2, Appendix A). Samples KW24a, KW24b, and KW22 (South Range

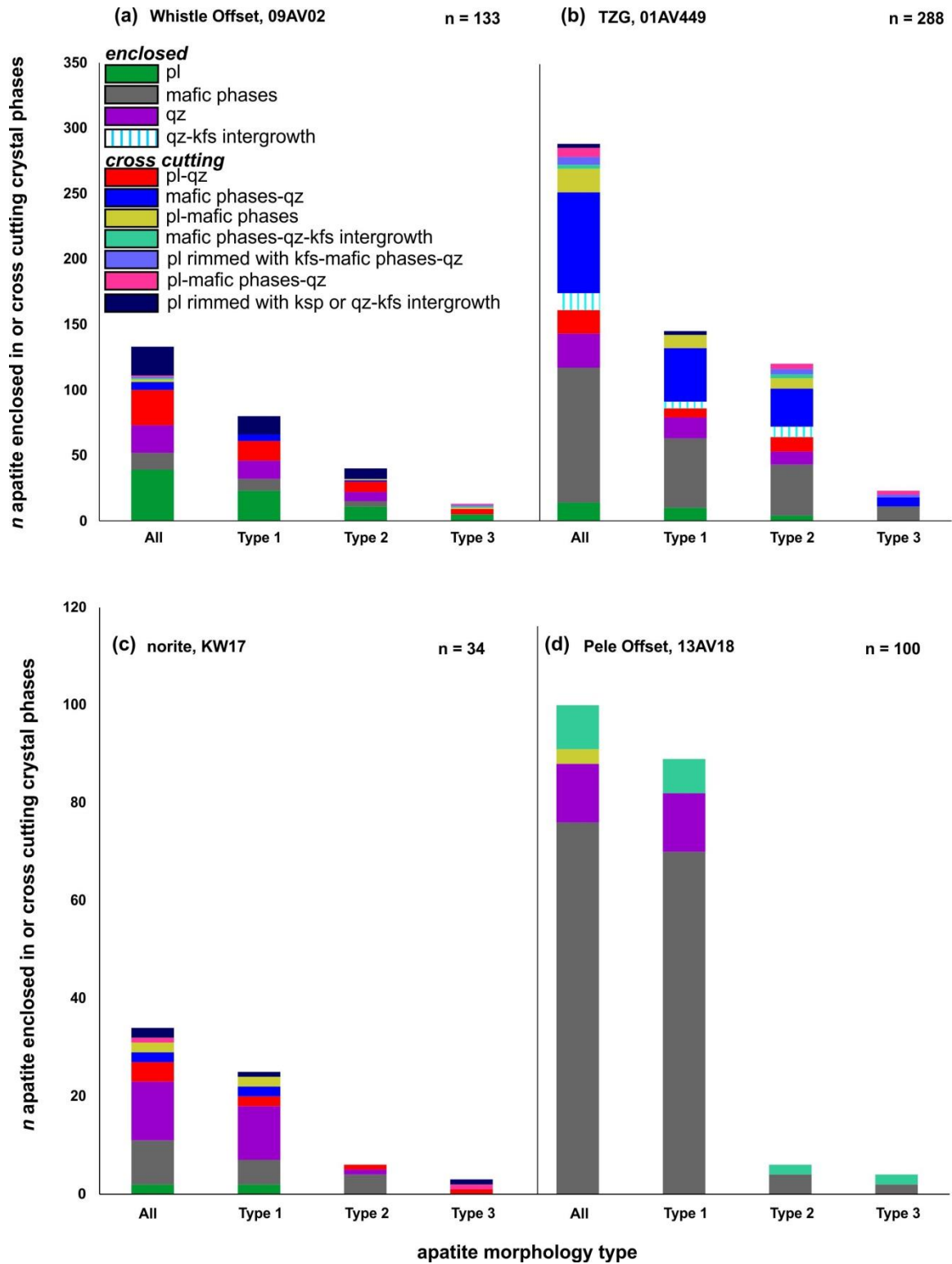


Figure 2.6: Morphology and host phases of apatite as deciphered by colour CL. Results are shown from (a) the leucocratic quartz diorite Whistle offset dike, sample 09AV02, (b) the TZG, sample 01AV449 (c) the norite, sample KW17, and (d) the Pele offset dike. Apatite shows 3 distinct morphologies in thin section: Type 1 is hexagonal in cross section; Type 2 is elongate hexagonal; and Type 3 is needle like. Apatite was divided into groups based on the host phase or phases which apatite is cutting. Host phases are: pl = plagioclase; mafic phases are comprised of oxides and pyroxenes and altered pyroxene phases; qz = quartz; qz-kfs intergrowth = quartz-potassium feldspar intergrowth texture. Cross cutting mineral phases are: pl-qz = cross cutting plagioclase and quartz; mafic phases-qz=cross cutting pyroxene, oxides, and/or pyroxene alteration phases; pl-mafic phases = cross cutting plagioclase and pyroxene, oxides, and/or pyroxene alteration phases; mafic phases-qz-kfs intergrowth = pyroxene, oxides, and/or pyroxene alteration phases and quartz-potassium feldspar intergrowth texture; pl rimmed with kfs-mafic phases-qz = plagioclase rimmed with potassium feldspar alteration and pyroxene, oxides, and/or pyroxene alteration phases and quartz; pl-mafic phases-qz = plagioclase and pyroxene, oxides, and/or pyroxene alteration phases and quartz; pl rimmed with ksp-quartz-kfs intergrowth = plagioclase rimmed with potassium feldspar alteration and quartz-potassium feldspar intergrowth texture.

norite) analysed by LA-ICP-MS are included in Table 2.3, Appendix A. Samples 24a and 24b, on a cm scale, showed two phases a dark coloured mafic norite and light coloured TZG. The sample was sawed along the boundary and analyzed separately.

2.3.4 REE zonation in apatite

CL images show that apatite can be strongly zoned in the North Range TZG and norite. A large hexagonal apatite grain (~1000 µm in length) from the North Range TZG (KW18) mapped by LA-ICP-MS shows that Sr, Y, Sm, Eu, Tb, La, Dy, Lu, Th, and U are strongly concentrated in the core (Fig. 2.7). In contrast, an in situ apatite grain of the about the same size and morphology from the North Range norite (02AV606) also mapped using LA-ICP-MS showed the elements mentioned above are strongly concentrated in the rim of apatite, the opposite of what is found in the gabbro (Fig. 2.8).

2.3.5 Melt inclusion petrography

Melt inclusions in the North Range TZG, norite and Whistle and Pele offset dikes are commonly elongate bullet shaped or negative crystal shaped inclusions that range in size from 10 to 200 µm. The melt inclusions occur parallel to the c-axis of host apatite which indicates primary origin (Fig. 2.9). Unheated melt inclusions are mainly crystalline with distinct dark and light coloured crystal phases. When heated close to or above the temperature required for complete melting (~1100°C), the melt inclusions appear as 2 distinct types: (i) dark coloured glassy or (ii) light coloured glassy. Mixed melt inclusions are also common and contain dark coloured globules within a clear glassy matrix or as contrasting phases occupying opposite ends of the melt inclusion. Where these co-

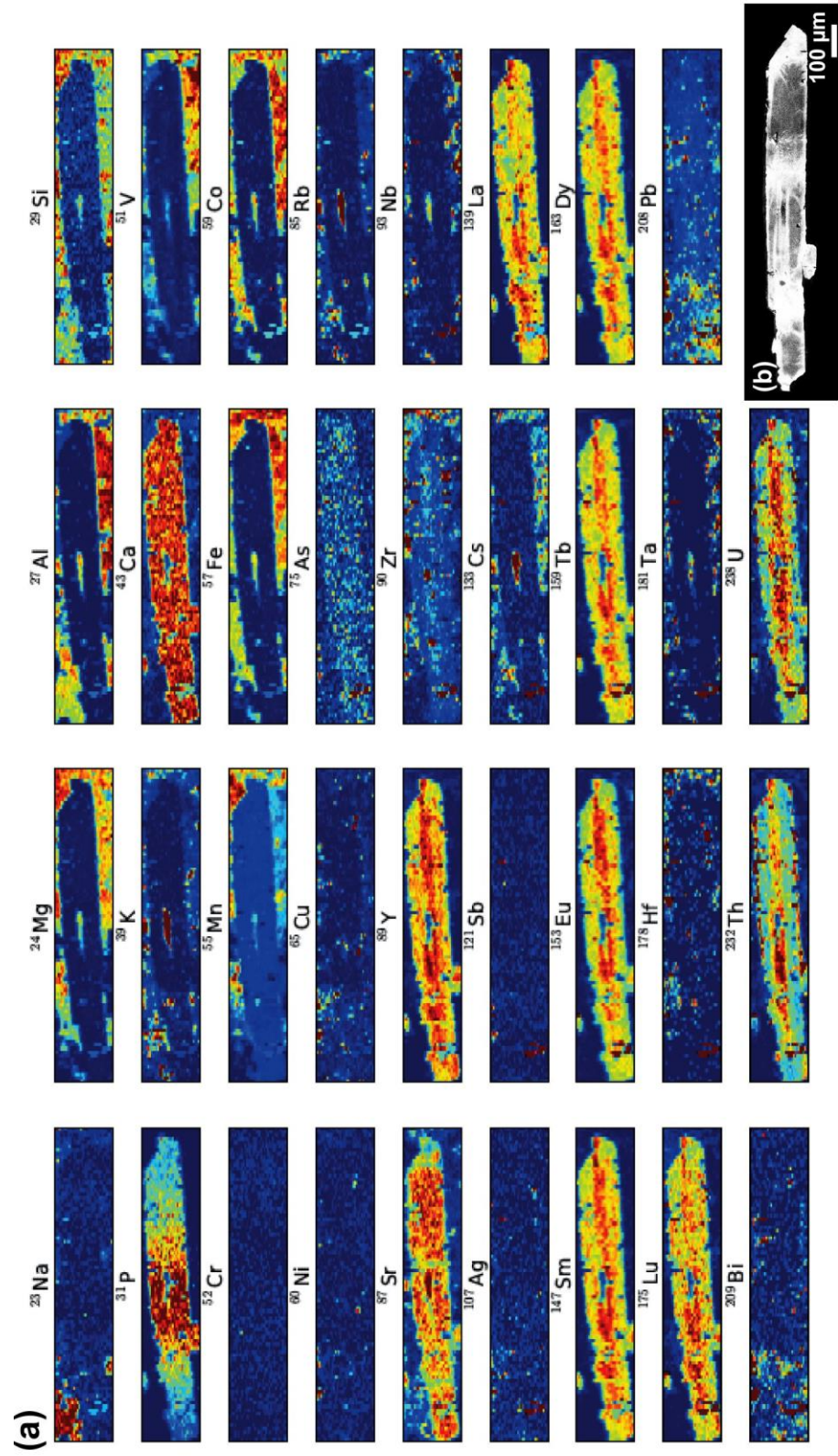


Figure 2.7: Zoned apatite grain from the TZG. (a) LA-ICP-MS map of apatite, KW18, from the Main Mass TZG showing REE zonation. (b) SEM-CL image of zoned apatite grain. Note that the elemental zonation patterns are opposite to that of apatite in the norite shown in Figure 2.8. The CL image shows grey scale fluorescence variations related REE zonation.

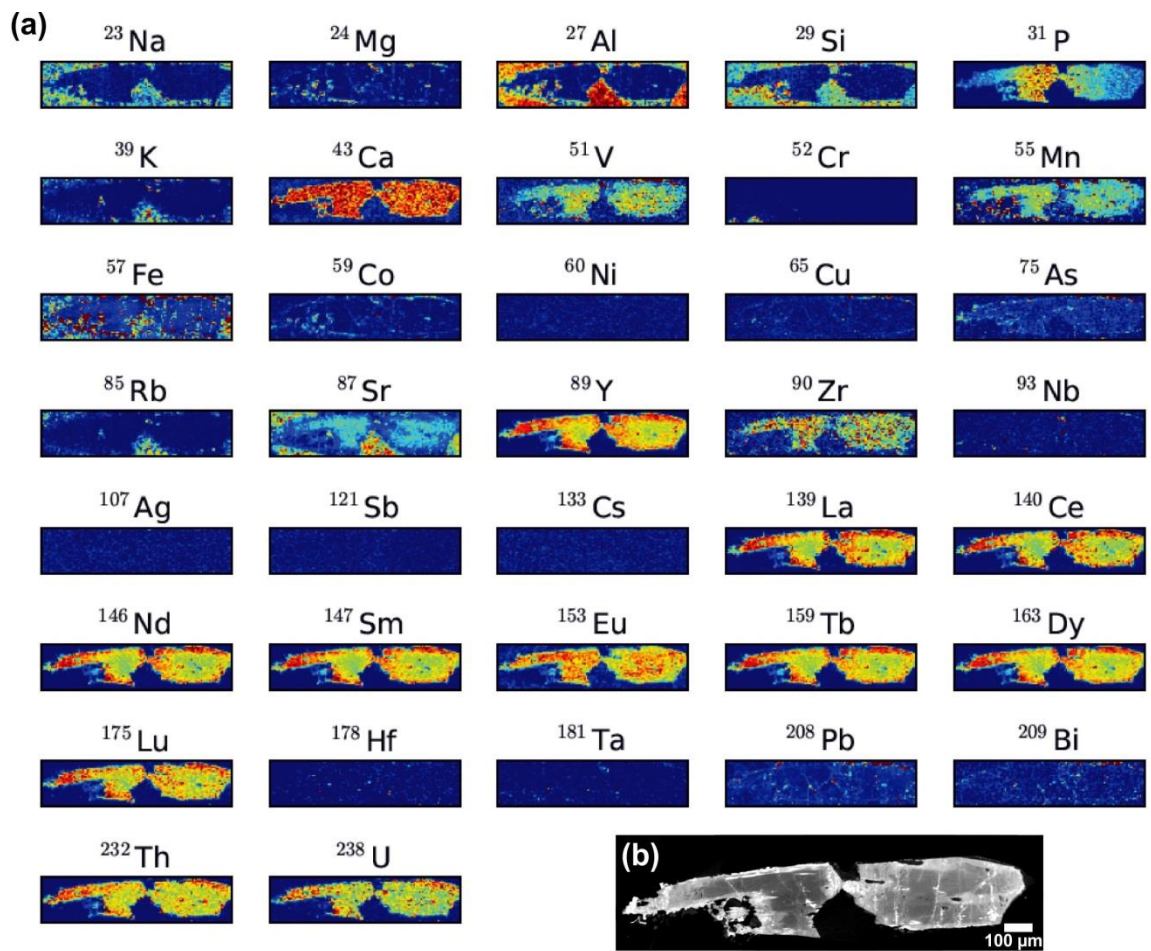


Figure 2.8: Zoned apatite grain from the norite. (a) Apatite from the norite, 02AV06, shows trace element zonation. (b) The corresponding CL image of the apatite grain. The trace elements (REE + Y, U, Th) are concentrated strongly in the rim of apatite.

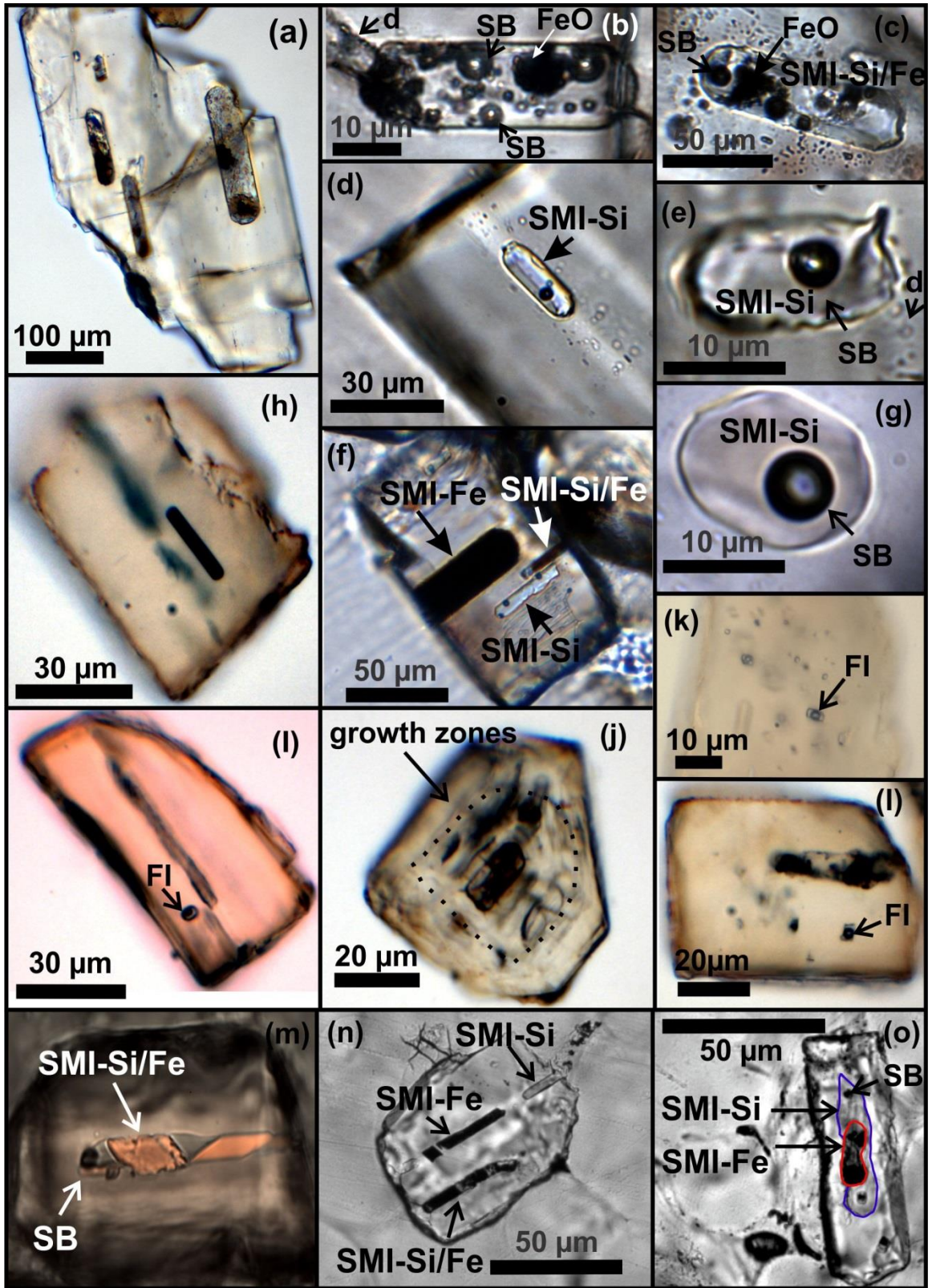


Figure 2.9: Melt inclusions hosted in apatite from the North Range Main Mass and offset dikes. Representative melt inclusion types in apatite in the TZG (a-g), leucocratic quartz diorite Whistle offset (h-l) and quartz diorite, Pele offset (m-o). (a) Shows an unhomogenized melt inclusion. (b and c) Show homogenized melt inclusions that show a mixture of Fe- and Si-rich liquid. (d and e) Show homogenized Si-rich melt inclusions, as well as mixed melt inclusions. (f) Shows a single apatite grain that has trapped both pure end-member Fe-rich homogenized melt inclusions, as well as mixed. (g) Shows a homogenized Si-rich melt inclusion. (h) Is an unhomogenized melt inclusion. (i, j, and k) Demonstrate the large vapor bubble in fluid inclusions from the Whistle offset dike. (l) Shows a heterogeneously trapped mixed melt inclusion and fluid inclusion in a single apatite grain from the Whistle offset dike. (m) Shows an unhomogenized melt inclusion from the Pele offset dike (PPL). (n and o) Show homogenized melt inclusions from the Pele offset dike (PPL). Abbreviations are as follows: SMI-Si is silicate melt inclusion that is Si-rich, SMI-Fe is silicate melt inclusion that is Fe-rich, SMI-Si/Fe is silicate melt inclusion that has trapped both end-member types, SB is shrinkage bubble, PPL is plane polarized light, and XPL is cross polarized light.

entrapped end-members were observed in highly variable proportions from one inclusion to another, and could not be homogenized on heating (see below), unambiguous evidence for heterogeneous entrapment is presented. Coevally trapped fluid and melt inclusions are commonly found in host apatite, more so in the norite and Whistle offset dike than in the Pele offset dike and TZG. When present, fluid inclusions in apatite are very abundant, although too small to use for microthermometry (~1-5 μm). Unheated melt inclusions in apatite from the quartz diorite are also found to occur parallel to the c-axis of host apatite, but these melt inclusions are glassy with small amounts of crystalline phases and may show the presence of a vapor bubble at room temperature. Both light coloured and dark coloured glassy phases are present in melt inclusions as mixed (heterogeneously trapped) and end-member pure dark and light coloured melt inclusions. Further details of melt inclusion petrography for homogenized and unhomogenized material hosted in apatite in the TZG, norite, and quartz diorite offset dikes is given in Figure 2.9. The finding of a single sulfide melt inclusion in apatite from the Pele offset (Fig 2.10) is of interest. This particular melt inclusion, although depleted in Ni, contains ~20 wt; % Zn, ~20 wt; % S, ~8 wt; % Fe, ~7 wt; % Pb, and ~2 wt; % Cu. Mapping of melt inclusions by SEM indicates a slight zonation of elements from its core to rim (Fig. 2.10). This melt inclusion may have originated as the result of a sulfide blob that became trapped in the viscous Si-rich melt (Chung & Mungall, 2009). In unheated grains that show crystalline phases it cannot be determined indefinitely if the melt inclusion is Si- or Fe-rich. Melt inclusions must be completely melted in order to distinguish between mixed and homogeneous inclusions on the bases of the presence of absence of a meniscus or two distinct types of liquid.

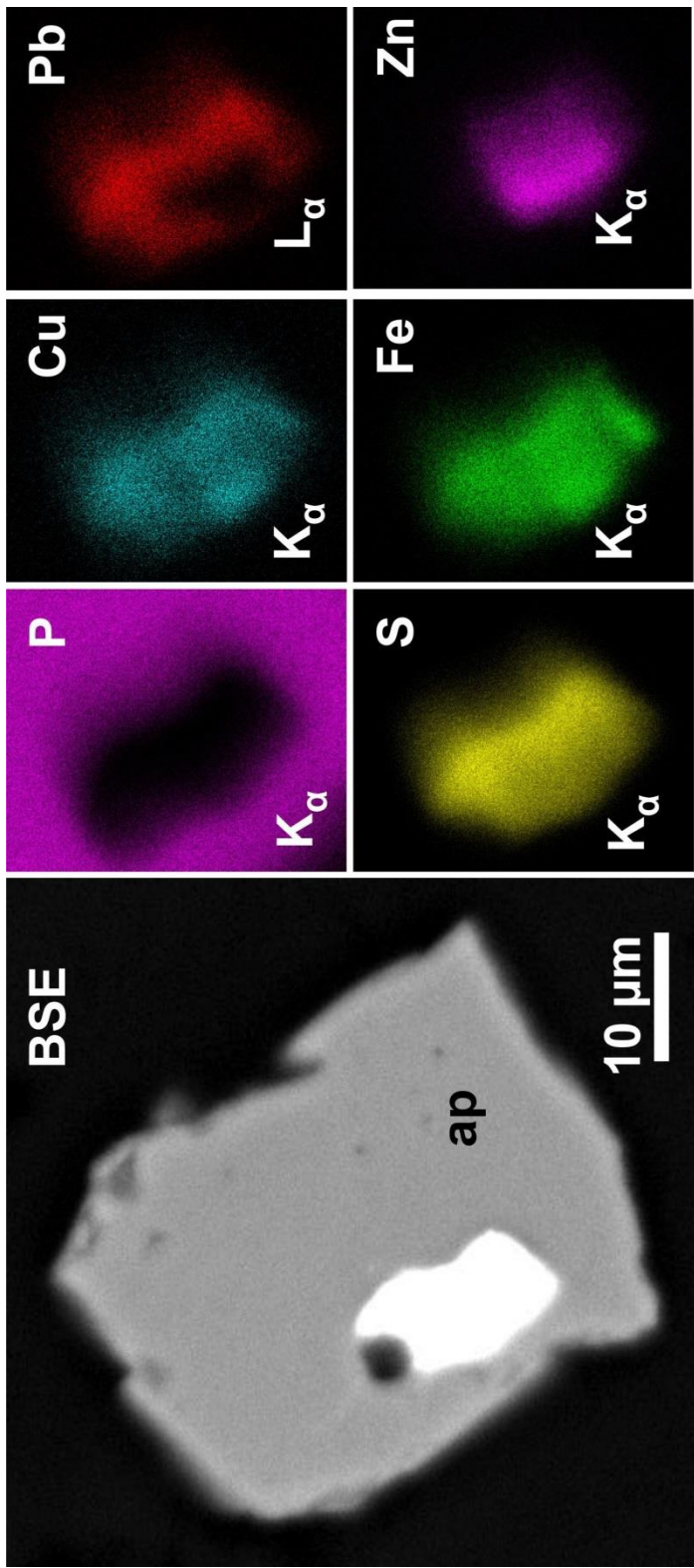


Figure 2.10: Element SEM maps of sulfide melt inclusions hosted in apatite from the Pele offset dike. SEM-BSE image (a) shows a sulfide melt inclusion trapped in anhedral apatite from the Pele Offset where it appears a bubble is present near the top of the inclusion. SEM element maps (b-g) show that the inclusion is nearly homogeneous but shows slight zonation.

2.3.6 Melt inclusion major element chemistry

Coeval (co-entrapped) melt inclusion compositions from the TZG and Pele offset dikes show two distinct types when analyzed with the SEM (Table 2.4, Appendix A). The chemistry of major elements by LA-ICP-MS shows that contrasting melt types are also found in the norite and Whistle offset dike (Table 2.5, Appendix A). Si-rich melt inclusions range in composition from tonalitic to granodioritic (60-70 wt % SiO₂, up to 11 wt % FeO). Fe-rich melt inclusions range in composition from syenogabbroic to essexitic to alkali gabbroic (27-49 wt % SiO₂, 16-44 wt % FeO), determined by SEM-EDS and EMP analyses of opened, homogenized melt inclusions. Melt inclusions hosted in apatite from the norite and Pele and Whistle offset dikes commonly contain heterogeneously trapped inclusions and are reported in Table 2.5, Appendix A as “potential mixed” inclusions (~45-57 wt % SiO₂, ~10-15 wt % FeO).

2.3.7 Melt inclusion trace element chemistry

Trace element chemistry of apatite-hosted melt inclusions by LA-ICP-MS in the Main Mass shows that the elements most strongly concentrated in the Fe-rich melt are V, Cr, and Co, but significant levels of Rb and Nb are also noted. Very few Si rich melt inclusions were observed in the Pele and Whistle offsets (2 and 1, respectively). In the Pele offset, concentrations of trace elements are generally concentrated in the Fe-rich melt are V, Cr, Co, Ni, As, Rb, Sr, Y, Zr, Nb, Ag, Sb, and Cs. The Pele offset dikes contained abundant apatite-hosted Fe-rich melt inclusions and trace element concentrations are comparable to those in apatite from the overlying norite. Melt inclusions, both Si-rich and Fe-rich, hosted in apatite from the mineralized Whistle offset

(09AV02) show Ni enrichment by up to 4 orders of magnitude more than those liquids trapped in the units stratigraphically higher in the SIC. In contrast, chemistry of melt inclusions from the unmineralized Pele offset (13AV18) shows very little enrichment in Ni or Cu, with the exception of a few inclusions (Table 2.5, Appendix A).

2.3.8 Trace element partition coefficients between apatite and coeval melt

Apparent $K_d^{\text{apatite/melt}}$ values for both Si- and Fe-rich inclusions in the TZG and norite show that the REE Sr, and Y are compatible in apatite, and As is weakly compatible or incompatible in apatite, whereas the following elements are incompatible (in increasing order of incompatibility: Cr, Ni, Cu, Zr, Co, Cs, Ag Nb, Hf, Ta, Rb) (Fig. 2.11) (Table 2.6, Appendix A). $K_d^{\text{apatite/melt}}$ values for apatite from the Whistle and Pele offsets are comparable although figures are based on lesser amounts of Si-rich trapped melt and are shown in Figure 2.12.

2.3.9 Trace element partition coefficients between Fe-rich and Si-rich melt

Apparent K_d values between the two coexisting melt phases ($K_d^{\text{Fe-rich/Si-rich}}$) in the TZG show that most trace elements were weakly compatible or incompatible in each melt phase, with the exception of V, Co, Rb, Sr and Cs that show consistent enrichment in the Fe-rich melt phase. However, moving down stratigraphy in the SIC, K_d values show that in the noritic unit of the North Range all elements analysed prefer the Fe-rich melt, with the exception of Ni and Cu that hover around a K_d value of 1 (Fig. 2.13). The K_d values between contrasting melt types in the Whistle and Pele offset dikes are comparable,

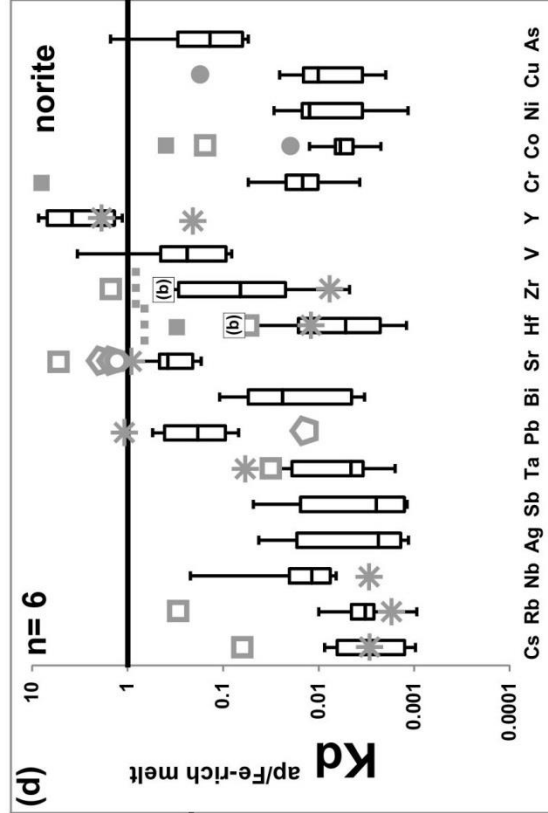
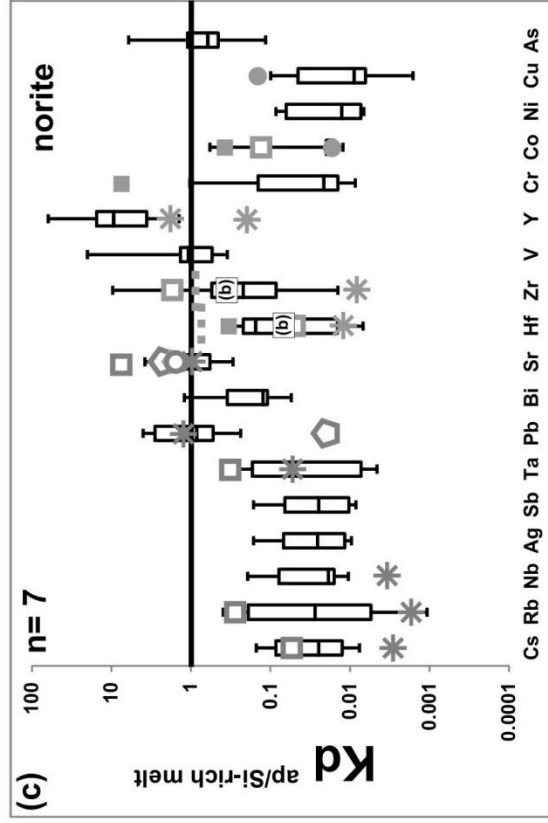
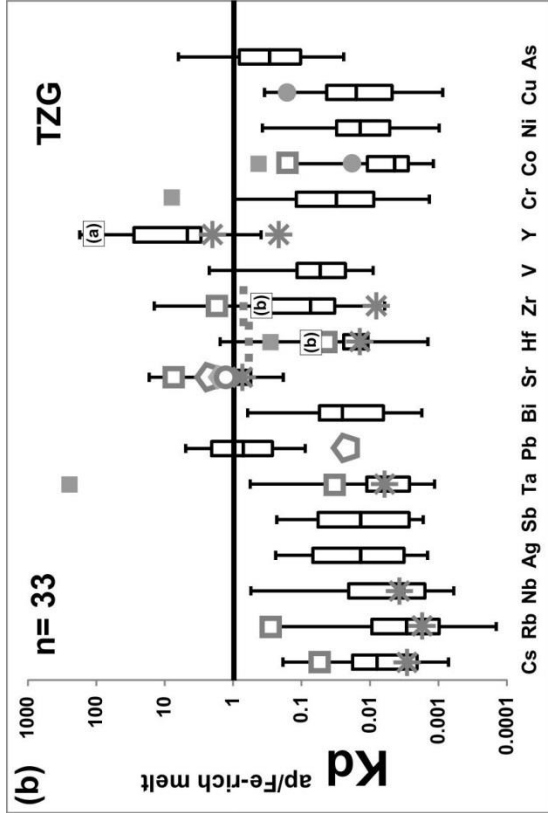
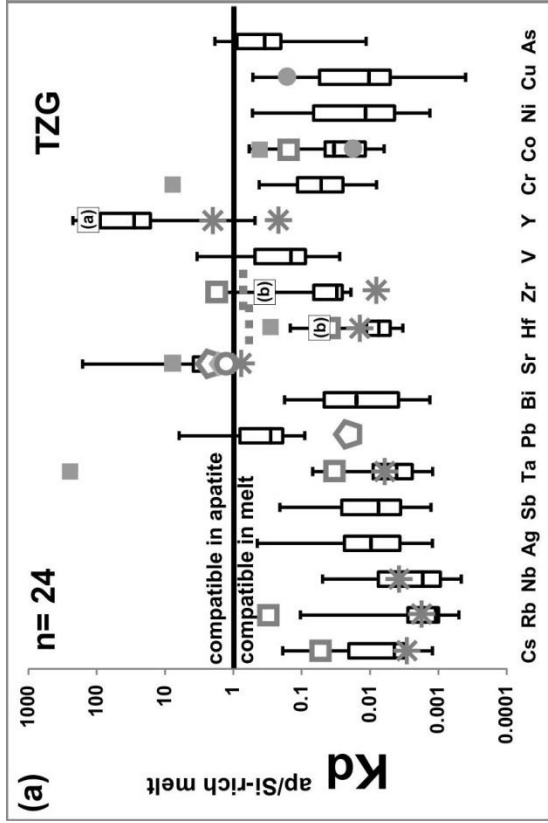


Figure 2.11: Box and whisker plots of the Kd values between apatite and melt inclusions in the Main Mass. (a) Shows Kd values corresponding to the Si-rich melt of the TZG. (b) Shows Kd corresponding to the Fe-rich melt inclusions of the TZG. (c) Shows values corresponding to the Si-rich melt inclusions of the norite. (d) Shows values corresponding to the Fe-rich melt of the norite. Reference Kd values plotted in the diagrams include: Solid squares = trachyandesite (Luhr *et al.*, 1984); Solid circles = basalt (Paster *et al.*, 1974); Hollow squares = panterllerite-trachyte (Mahood & Stimac, 1990); Stars = carbonatite (Klemme, 2003, Dawson & Hinton, 2003); Open pentagon = granite; Open circles = basanite basalt; Solid pentagons = tholeiitic-andesite (Watson & Green, 1981); (a) = per-aluminous granite (Bea *et al.*, 1994); (b) = andesite; Dashed line = dacite (Fujimaki, 1986).

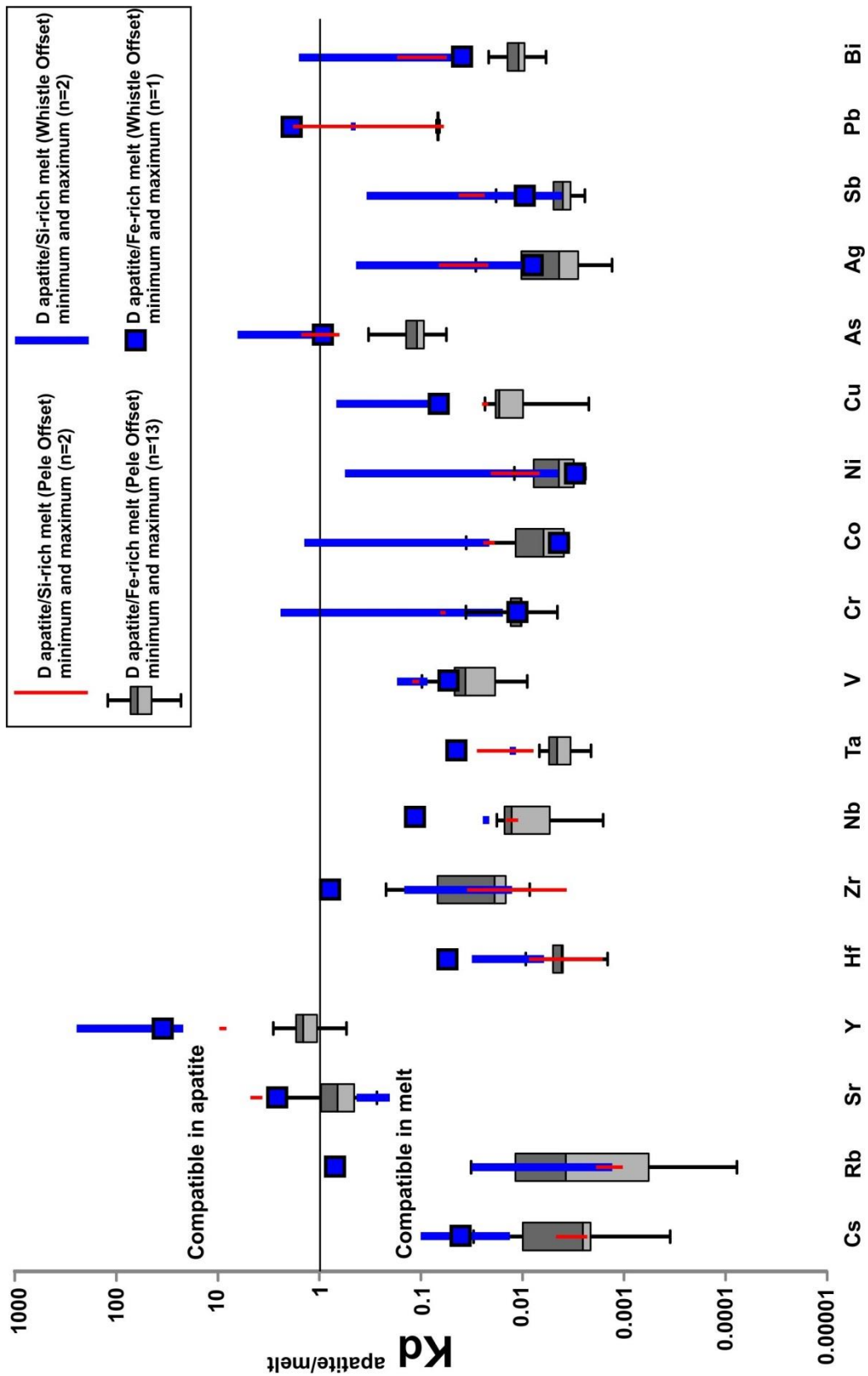


Figure 2.12: Box and whisker plot of Kd values between apatite and melt in two quartz diorite offset dikes. The Kd values between apatite and melt in the Pele offset are shown as box and whisker plots for $Kd_{\text{apatite/Fe-rich melt}}$. The Si-rich melt in the Pele offset are shown with red lines for minimum and maximum values. $Kd_{\text{apatite/Fe-rich melt}}$ for the Whistle offset is plotted as blue squares and $Kd_{\text{apatite/Si-rich melt}}$ for the Whistle offset are shown with blue lines for minimum and maximum values. Sr, As, Pb, and Bi are weakly compatible in apatite and Y is strongly compatible in apatite.

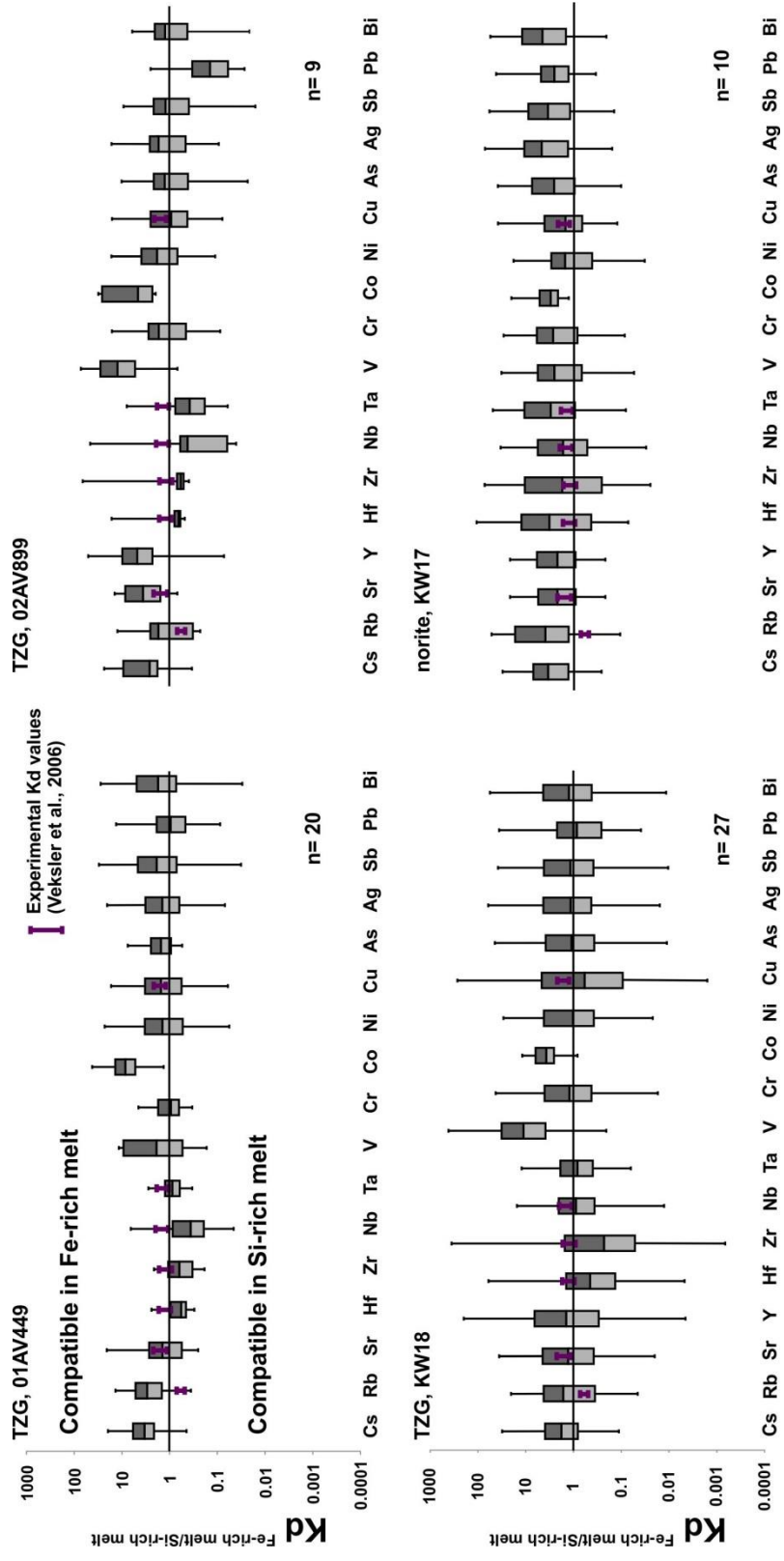


Figure 2.13: Plot of the Kd values between Si-rich melt inclusions and Fe-rich melt inclusions in the Main Mass. The Kd values are plotted from melt inclusions hosted in apatite from the TZG and the norite. Experimentally derived Kd values for immiscible Fe- and Si-rich melts (Veksler *et al.*, 2006) are also plotted with values from the SIC for comparison. Note that the experimental data set is incomplete compared to the data for the SIC and the experiments of Veksler *et al.* (2006) were carried out using a centrifuge at temperatures ranging from 1050° to 1100°C. The number (n) corresponds to the number of melt inclusions (both Si- and Fe-rich).

although figures are based on lesser amounts of Si-rich trapped melt, and are shown in Figure 2.14.

2.3.10 Microthermometry

2.3.10.1 TZG

Microthermometry for apatite-hosted melt inclusions from the TZG (01AV449) show that in mixed inclusions the formation of two bubbles is common, which may eventually form a larger bubble at temperatures above 1180°C. Bubbles form in large, homogenous and mixed melt inclusions, however in large inclusions it becomes less likely that homogenization will occur due to decrepitation (Fig. 2.15). Vapor bubbles in melt inclusions are not visible at room temperature and melt inclusions do not appear to be glassy at room temperature, except the inclusions that appear to be the pure Si-rich end-members. The most successful microthermometry results come from small, homogeneous inclusions where complete melting occurs at ~1100°C and homogenization, which is close to the true trapping temperature, occurs at high temperatures from 1165° to 1236°C. The results are based on ~50 melt inclusion heating experiments in which 2 melt inclusions homogenized completely (bubble closure). An additional complication that occurs during microthermometry is that an unidentified dark coloured phase, present in most inclusions, does not melt, even at high temperatures >1250 °C. This dark phase may be due to the melt inclusions experiencing oxidation during heating which stabilizes the phase and prevents it melting.

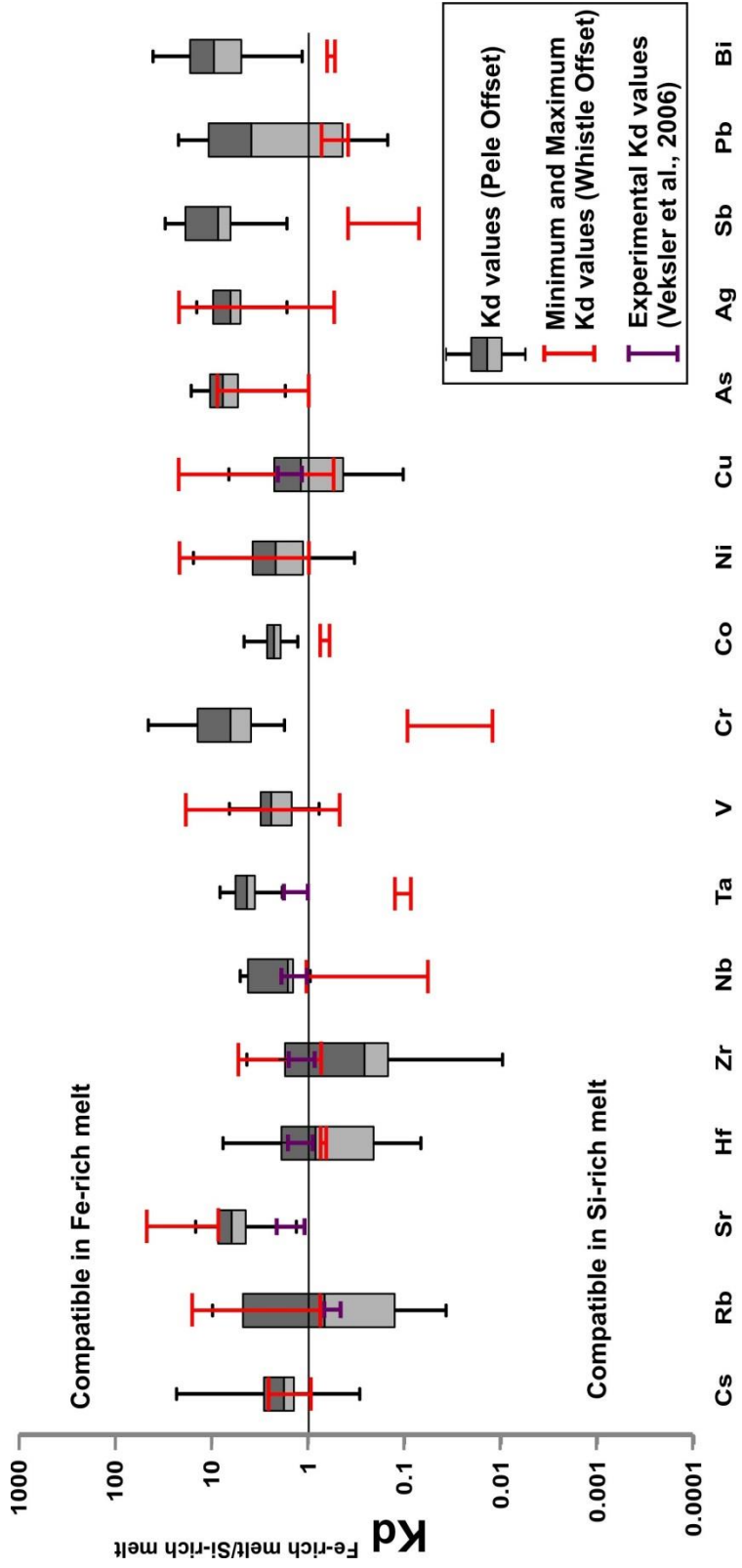


Figure 2.14: Plot of K_d values between Si-rich and Fe-rich melt in the Pele and Whistle offset dikes. The K_d values for trace elements between Fe- and Si- rich melt inclusions for the Pele offset dikes are shown as box and whisker plots which show that these values are close to 1, which compare favourable to what has been found experimentally (Veksler *et al.*, 2006). The exceptions noted are Sr, the incompatible elements (Nb, Ta), and Sr, Cr,As, Ag, Pb, and Bi which show slight affinities for the Fe-rich melt.

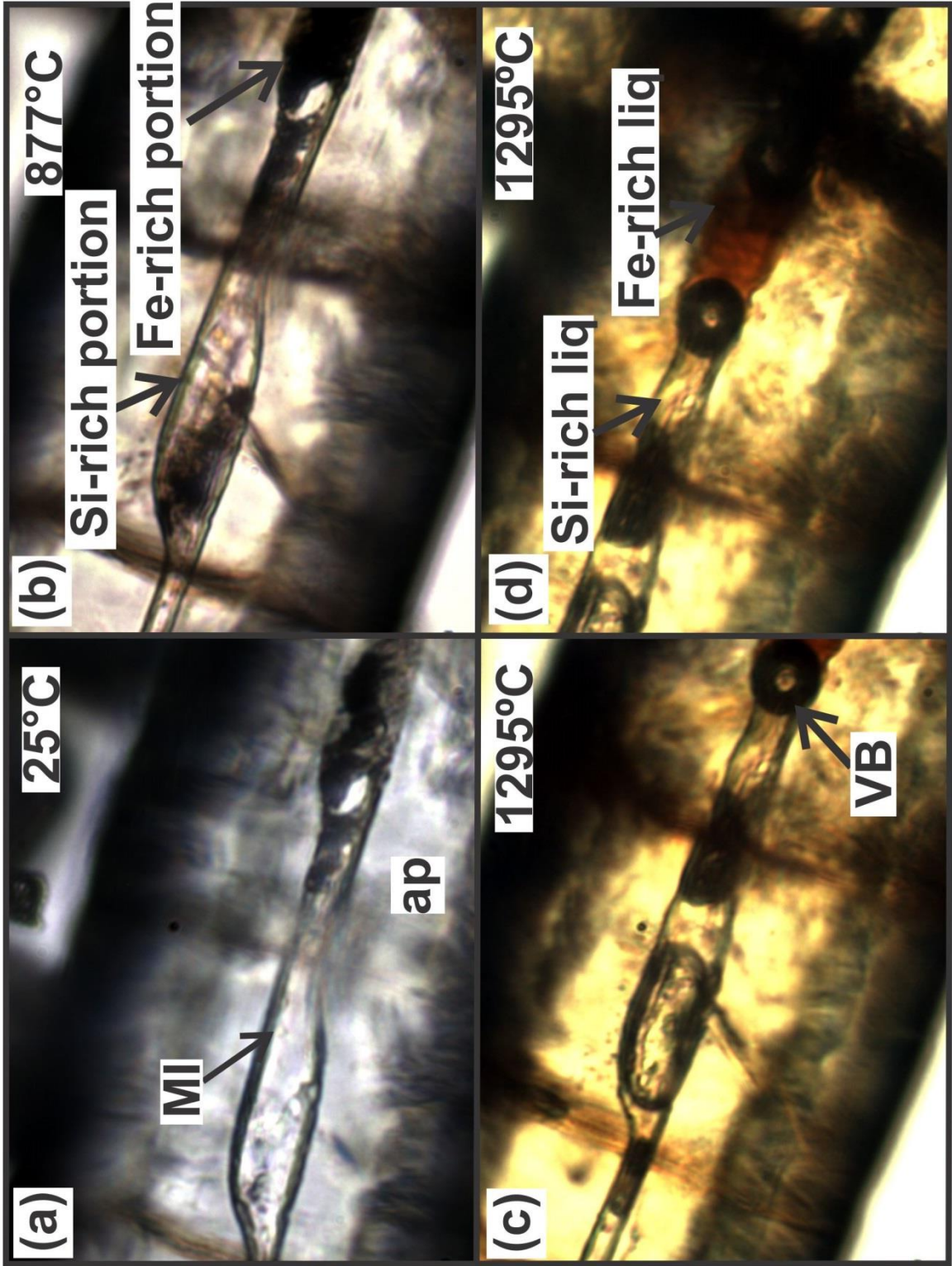


Figure 2.15: Microphotographs of microthermometric heating from 25° to 1295°C of an apatite-hosted melt inclusion from the TZG. At room temperature (a) the 2 phases of the melt inclusion are visible with the dark part (right) comprising the mafic components and the light part (left) containing the felsic components. At 877°C (b) the contrasting melt types are more visible. (c, d) Show that complete melting has occurred at some temperature below 1295°C, as a vapor bubble is now visible and the two melt compositions have completely melted but have not dissolved/mixed to form a homogenous melt. The melts remain immiscible above 1295°C.

2.3.10.2 Pele offset dike

Microthermometry was conducted on 7 melt inclusions from sample 13AV18 (Pele offset). Unlike the melt inclusions hosted in apatite of the TZG, inclusions commonly appear glassy at room temperature with the presence of a vapor bubble (Fig. 2.9, m). During microthermometry, if a vapor bubble was not visible at room temperature then one appeared during heating the inclusion at 1069°C and 1081°C, which is inferred to be a maximum eutectic temperature. The appearance of a single bubble is commonly followed by the appearance of one or more additional bubbles within 20 °C. Two melt inclusions were observed to have vapor bubble closure, which is inferred to approximate the actual trapping temperature (the liquidus temperature), the first at 1135°C and the second at 1207°C. In the first melt inclusion, the vapor bubble appeared at 1069°C and by 1080°C 2 other vapor bubbles, both visible, were shifting in the inclusion. These bubbles converged to form one larger bubble at 1118 °C and then slowly began to close; at 1135°C the bubble closed completely (Fig. 2.16). In the second melt inclusion, a vapor bubble existed at room temperature and the bubble appeared to move at 1128°C and at 1140°C there were 3 bubbles visible. The bubbles began to shrink and close one after the other, until the final bubble closure occurred at 1207°C (Fig. 2.17). Both of the inclusions described above appeared to be homogeneous, Fe-rich end-members at the stage where bubble closure occurred. Unsuccessful thermometric measurements of mixed melt inclusions displayed immiscible behavior similar to what was found in apatite-hosted melt inclusions from the TZG. In two mixed melt inclusions, the dark and light coloured portions occupied opposite ends of the melt inclusion and in one, where the dark coloured phase turned to a golden-brown liquid, mixing with the

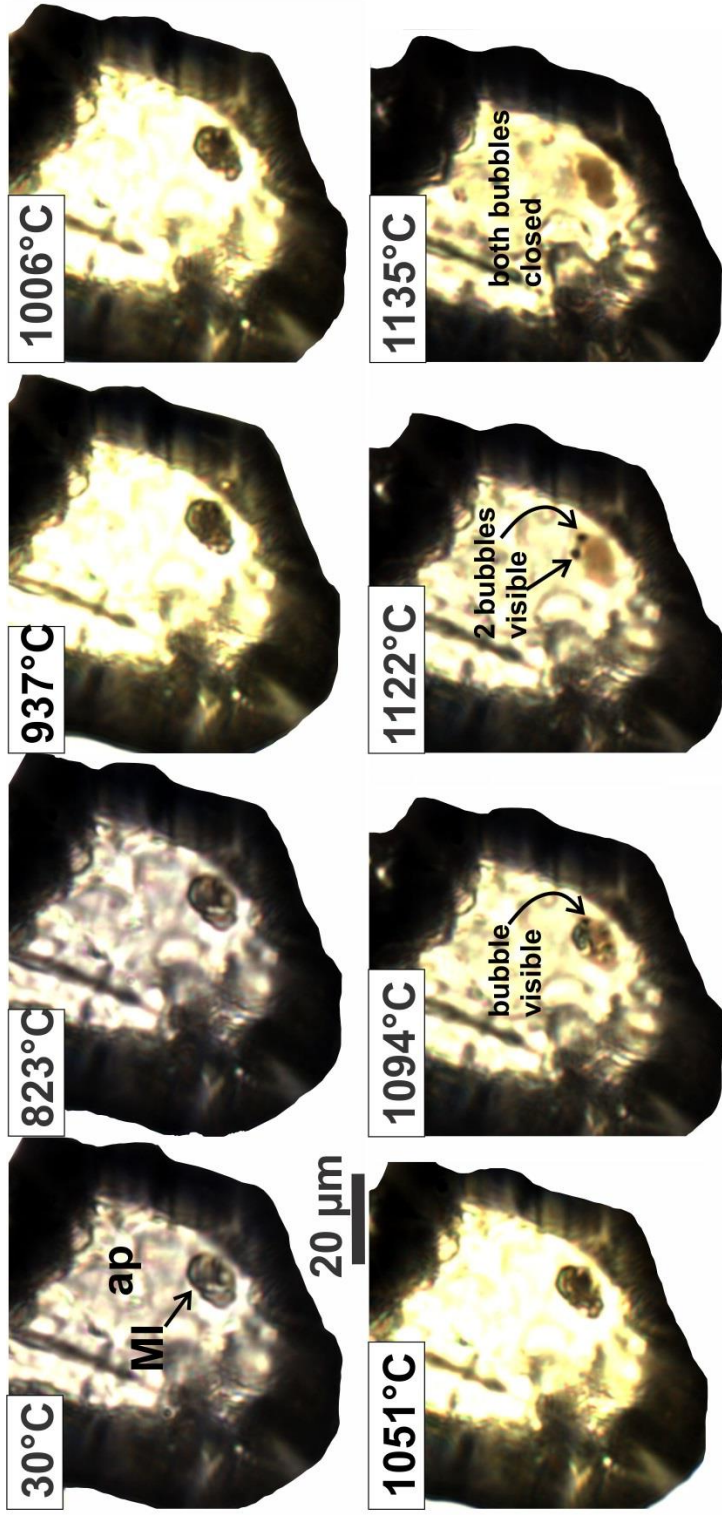


Figure 2.16: Microphotographs of an Fe-rich melt inclusion from the Pele offset showing the effects along 8 step changes from thermometric heating from 30°C where is homogenizes at 1135°C. The appearance of the first vapor bubble was at 1069°C. At 1080°C 2 other vapor bubbles were visible and shifting in the inclusion. The bubbles converged to form one larger bubble at 1118°C and then slowly began to close. At 1135°C the bubble closed completely (~trapping temperature).

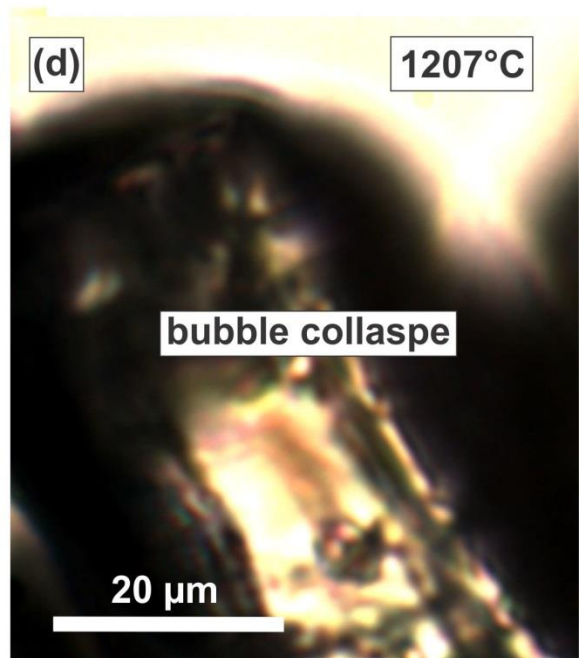
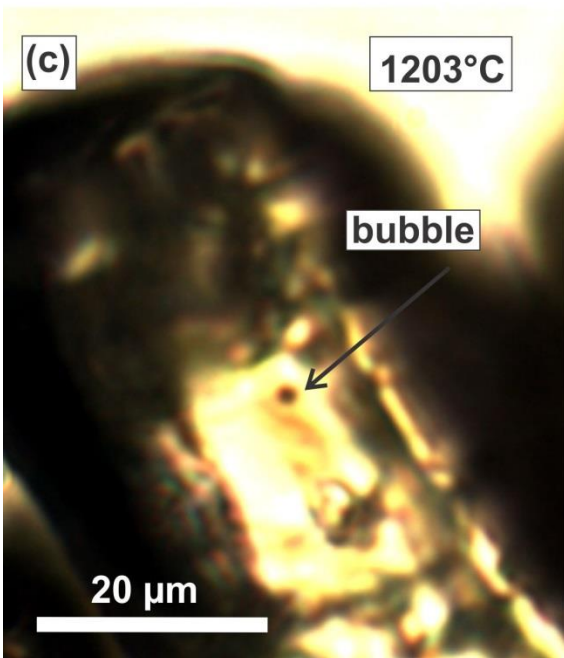
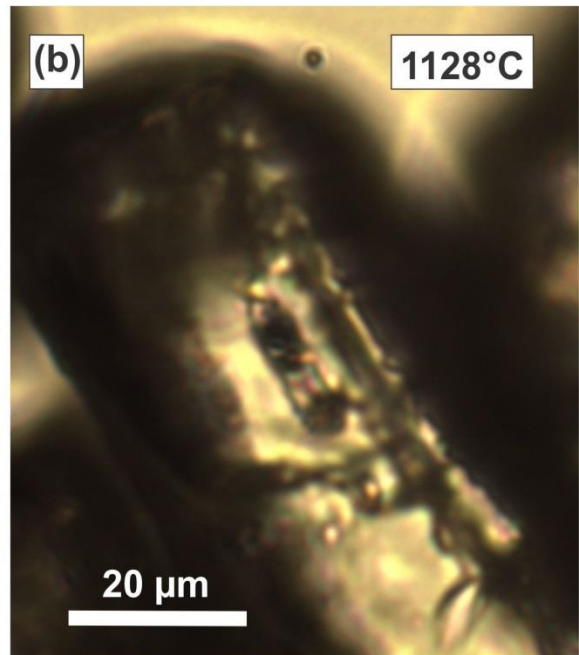
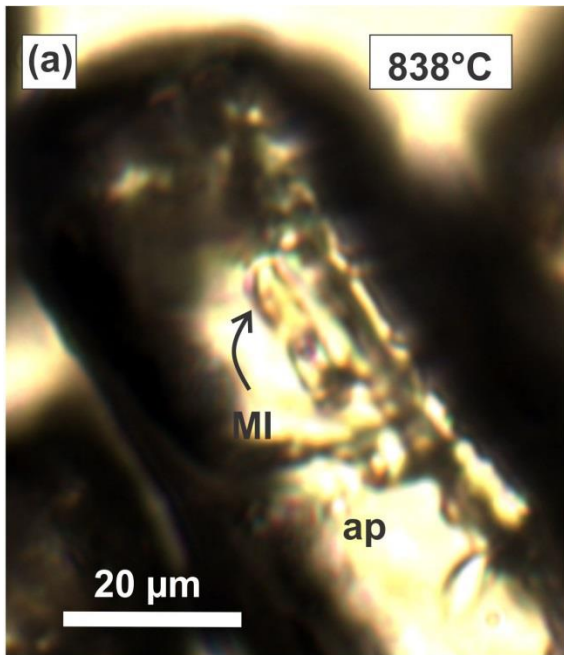


Figure 2.17: Photomicrographs of microthermometric heating of an apatite-hosted Fe-rich melt inclusion from 838° to 1207°C from the Pele offset that homogenizes at 1207°C. (a) Shows that the melt inclusion with a vapor bubble at room temperature began to melt at 838 °C. (b) Shows that the bubble appeared to move at 1128°C; by 1140°C 3 vapor bubbles were visible. (c, d) Shows that the bubbles began to shrink and close one after the other until the final bubble remaining closed at 1207°C (~trapping temperature).

light coloured phase did not occur, even at temperatures above 1300°C. In another, the dark end appeared as dark solids and melting of this material did not occur at temperatures above 1250°C.

The criteria used during heating of melt inclusions to determine whether they contain heterogeneously entrapped end-member liquids are that: (i) dark and light coloured liquids must remain immiscible after melting to very high temperatures (above the expected liquidus temperature based on heating of pure end member inclusions); and (ii) dark and light coloured liquids show highly variable volumetric proportions from one inclusion to another in single samples or inclusion assemblages. In samples from the TZG mixed melt inclusions remain immiscible until well above the expected liquidus temperature of the host melt. In contrast, it is possible that mixed melt inclusions in the quartz diorite may homogenize at temperatures closer to the inferred liquidus temperature of ~1135° to 1207 °C; this in conflict with compositional evidence (see below) for two-liquid immiscibility. The maximum eutectic temperature ($T_{\max}^{\text{eutectic}}$) is inferred by the minimum temperature at which liquid appears in the melt inclusion and this may be measured by observing the liquid becoming visible within the inclusions as they change shape or shift. The minimum liquidus temperature ($T_{\min}^{\text{liquidus}}$) is inferred as that temperature where the melt inclusion has completely melted and no visible solids remain. The temperature of homogenization (T_h) is measured by the disappearance of the final vapor bubble remaining in the melt inclusion, or may also be estimated as the temperature at which the vapor bubble appears to be the smallest before decrepitation or melting of the host phase (i.e. apatite). Results of microthermometry are listed in Table 7, Appendix A.

2.4 Discussion

2.4.1 Major questions surrounding the SIC and its ores

There is considerable debate the surrounding proposed models pertaining to the source of the melt that crystallized as the SIC. It has been suggested that the impact melt sheet was a homogeneous, crust derived melt (Kuo & Crocket, 1979; Dicken *et al.*, 1999) that may have comprised a small mantle contribution (Lightfoot *et al.*, 1997a). Isotopic evidence strongly suggests that the SIC, including the sublayer and its ores, represents crystallization of an impact melt having a single source (Faggart *et al.*, 1985, Greive *et al.*, 1991, Dicken *et al.*, 1999) and REE data strongly suggest a crustal derived magma (Kuo & Crocket, 1979). Warner *et al.* (1998) conducted a detailed study of the chemical composition of apatite crystals in the SIC and concluded from this that the complex evolved by fractional crystallization of a single melt sheet, which was silica rich and mainly crustal in origin, if not solely. However, the large amount of granophyre overlying the norite and TZG has been problematic in modelling the evolution of the SIC melt sheet (e.g. Ariskin *et al.*, 1999).

An alternative model for the SIC involves the emplacement of separate batches of magma (Peredery & Naldrett, 1975; Chai & Eckstrand 1994; Ariskin *et al.*, 1999). Chai and Eckstrand (1993) found that the REE contents of the granophyre are nearly double that of the norite and that this could only be accounted for by the emplacement of separate batches of magma. However, whereas Lightfoot *et al.* (1997a) concur that the granophyre typically has double the abundance of incompatible elements when compared to the felsic norite, they found that the ratios of incompatible elements of the granophyre

and felsic norite are strikingly similar. This latter observation led these authors to conclude that the compositional differences between these two rock suites is likely due to in-situ differentiation of one parental magma of crustal derivation, rather than mixtures of upper crust, lower crust, and mantle derived magmas.

Zieg and Marsh (2005) suggest that the sharp geochemical contrast between the granophyre and the felsic norite is entirely due to the bi-modal composition of the target rocks in the continental crust and that the magnitude of the impact did not allow for homogenization into a single magma, but rather resulted in segregation of the melt before igneous fractionation occurred. In this model, known as “viscous emulsion differentiation”, the authors propose that the melt sheet was at no point in time a single uniform magma and, instead was stratified before crystallization began. In this model the bulk composition of the melt sheet is nearly identical to the bulk composition of the local crust, but rather than homogenous in nature the superheated (~1700 °C) melt sheet was comprised of interdispersed parcels of viscous mafic and felsic melt. Thus, the model suggests that the sharp geochemical transition between the norite and the granophyre is due solely to the bimodal nature of the target rocks which comprised continental crust and that differentiation, or in this case unmixing, of the melt occurs strictly in the liquid state and prior to any crystallization processes. If the SIC melt sheet been density stratified before crystallization then the most basal melt layers would be more mafic which would explain the mafic-ultramafic domains within the sublayer of the SIC that have been dated to be the same age as the SIC (Lightfoot *et al.*, 2001).

The quenched marginal phase of the composite quartz diorite offset dikes is thought to represent the original melt composition of the SIC (Lightfoot *et al.*, 2001;

Pope *et al.*, 2004). Considered to be a closer approximation to the parental composition of the primary melt sheet, however, is the vitric andesite in the Onaping Formation (Ames *et al.*, 2002). If the melt sheet started off as a heterogeneous parental melt that would eventually experience silicate differentiation or silicate gravitational segregation, the quartz diorite offset dikes may represent primary silicate heterogeneity of the melt sheet (Lightfoot & Farrow, 2002). The question of heterogeneity of a parental melt (e.g. Lightfoot & Farrow, 2002; Darling *et al.*, 2010b) versus the model of “viscous emulsion” (e.g. Keays & Lightfoot, 2004; Zieg & Marsh, 2005) is difficult to address, as the scale of homogeneity in impact melts is itself poorly understood.

2.4.2 Evidence for silicate liquid immiscibility in the SIC and comparison of melt-host relationships to other magmatic systems

2.4.2.1 Petrographic evidence for silicate liquid immiscibility combined with microthermometry of melt inclusions

The presence of coevally (co-entrapped) Si- and Fe-rich melt inclusions in the same crystallizing phase (e.g., apatite) provide the only unambiguous evidence for immiscibility in a natural setting, either volcanic or plutonic setting (Jakobsen *et al.*, 2005; Charlier *et al.*, 2011). In the SIC Main Mass, and Pele and Whistle offset dikes, apatite-hosted melt inclusions occur parallel to the c-axis, an indication of their primary origin, and contain two distinct dark and light coloured phases. In this study, petrographic evidence that immiscibility developed early in the TZG is based on the coexistence of

these dark and light coloured melt inclusions and mixed (heterogeneously entrapped) melt inclusions in cumulate early formed apatite.

The textural criteria for apatite as a primocryst phase in the TZG is that it mainly occurs as euhedral crystals poikilitically enclosed in early forming plagioclase and by cutting all mineral phases, with the exception of late granophyre (i.e., intergrowth of quartz and potassium feldspar; Figs. 2.3, 2.4). However, petrographic colour CL images of apatite from the Pele and Whistle offset dikes, the norite, and TZG, as well as observations made during SEM-EMP analysis of apatite in the Main Mass, show that apatite occurs as three distinct morphologies in all units of the SIC (Figs. 2.3 and 2.6, Table 2.3, Appendix A). Each morphological type (hexagonal cross section, elongate hexagonal, needle) ranges in size: from 20 μm to upwards of 200 μm for hexagonal cross section, from 50 μm to upwards of 500 μm for elongate hexagonal, and from 100 μm to upwards of 1000 μm for needle. It is considered, therefore, that these distinct growth stages represent distinct stages of paragenesis (e.g. Meurer & Boudreau, 1996), and therefore at least some apatite-hosted melt inclusions in the norite and offset dikes represent early stage melts. It should be noted, however, that even for the large euhedral apatite, whereas the euhedral morphology and occurrence as inclusions in the major phases are two petrographic criteria commonly used to suggest early saturation of accessory phases in plutonic rocks (Hoskin *et al.*, 2000), such phases can grow under locally saturated conditions or in late-stage interstitial melt pools (Miles *et al.*, 2013; Hoskin *et al.*, 2000). However, needle type apatite was not included in the separates, as the separation technique was not amenable for these to be properly separated with the method used. Similarly, needle shaped apatite-hosted melt inclusions was not analysed

with any of the methods (i.e., SEM-EDS, EMP, LA-ICP-MS) used in this study. Thus, if the needle apatite represents the latest apatite to crystallize from late-stage residual liquids then any melt inclusions that may have been trapped during this stage in the evolution of the SIC are not represented by this study.

Apatite is rare in the norite compared to the TZG and the offset dikes, where based on its texture, apatite appears to be an early crystallizing phase (Figs 2.3 and 2.4). In the norite, previous workers interpreted apatite to occur as an intercumulus phase (Warner *et al.*, 1998), but whereas apatite is commonly found in the norite as needle type morphology or as cross cutting late stage granophyric patches and also as very small (>20 μm) grains embedded in oxides or in interstitial phases, transmitted light petrographic study of the least altered samples of the norite show that at least some apatite is hosted in cumulus plagioclase and associated with cumulus orthopyroxene (Fig. 2.4).

In combination, results of microthermometry of apatite-hosted melt inclusions indicate melt was trapped at temperatures from $\sim 1165^{\circ}\text{C}$ to 1236°C in the TZG (Table 7, Appendix A) and from $\sim 1135^{\circ}\text{C}$ up to 1207°C in the Pele offset dike (Figs. 2.16, 2.17) (Table 7, Appendix A). Microthermometric data tells us that temperature of the bulk liquid at the onset of immiscibility and also the temperature at which apatite reaches the liquidus must be a minimum of $\sim 1135\text{-}1165^{\circ}\text{C}$. Microthermometric data indicate, therefore, that the temperature of the bulk liquid at the onset of immiscibility and the time at which apatite saturated must have a minimum of $\sim 1135^{\circ}$ to 1165°C . This temperature range is higher than reported for the onset of immiscibility in basaltic compositions (e.g. Charlier & Grove, 2012, Charlier *et al.*, 2013), however, evolution of temperature as a function of time (the cooling rate) is also an important factor constraining the onset of

immiscibility and in a plutonic environment, where slow cooling conditions prevail, immiscibility can develop at a high temperature (Charlier *et al.*, 2013) and in the SIC it has been suggested that cooling of the melt sheet occurred over 0.5 Ma (Zieg & Marsh, 2005).

If apatite in the TZG and Pele offset comprised a mixture of early to late periods of crystallization, even for the same morphology type, then the large range for temperatures of homogenization (T_h) for the apatite-hosted melt inclusions for these units is explainable (Table 7, Appendix A). It is also considered that T_h temperatures recorded during microthermometric heating may be anomalously high due heterogeneously entrapped with fluid inclusions (e.g. Tibor *et al.*, 2011), and , therefore, apatite did not grow and trap melts at the microthermometric temperature reported. However, abundant fluid inclusions are only present in apatite from the norite and Whistle offset, while apatite from the TZG and Pele offset that microthermometry of melt inclusions was conducted on was free of any mineral or fluid inclusions. Additionally, it has been considered that immiscible melt end-member compositions may have resulted from necking of inclusions that were trapped as a homogenous parental melt, therefore, it would be inferred that the homogenous melt became immiscible at lower temperatures after apatite grew from the melt sheet. However, it would then be expected that heterogeneous inclusions would homogenize during microthermometry and even at temperature $>1300^{\circ}\text{C}$ is it common to see a meniscus separating the Fe- and Si-rich parts of the inclusion (Fig. 2.15).

2.4.2.2 Constraints on timing of apatite growth from apatite trace element chemistry

In basaltic compositions, it is generally accepted that apatite appears as a cumulus phase after $\geq 90\%$ of fractionation (Meurer & Meurer, 2006) and in the SIC apatite has previously been considered to appear as a cumulus phase only late in the fractionation history of the Main Mass, its first appearance, but one which is abundant, being in the TZG (Warner *et al.*, 1998). The trace- and REE-chemistry of apatite from this study show some differences compared with the findings of Warner *et al.* (1998). These differences are that apatite from the North Range norite show higher concentrations in HFSE (Zr and Hf) and in the South Range norite trace element trends are similar to previously published trends (Warner *et al.*, 1998) (Fig. 2.18).

Elemental zonation maps of in-situ apatite in the TZG and norite, as determined using LA-ICP-MS may serve as a proxy for both the timing of apatite growth with respect to other accessory phases and early forming plagioclase in the TZG. In intermediate to felsic magmas, the abundances of REE are controlled by accessory minerals and any changes in rare earth element abundances of an accessory phase records the effects of other accessory minerals precipitating, or even the earlier crystallization of the same phase (Hoskin *et al.*, 2000). Apatite from the TZG shows strong zonation of the REE which are concentrated in the core which suggests this apatite crystallized early. The enrichment of Eu in the core of apatite also suggests it grew before plagioclase (Fig. 2.7). In contrast, the apatite from the norite shows an opposite trend with REE strongly enriched in the rim of apatite which may infer the early crystallization of apatite rather than late from an intercumulus liquid locally enriched in REE (Fig. 2.8) (e.g. Warner *et al.*, 1998). As previously mentioned, petrographic evidence of apatite hosted in cumulus

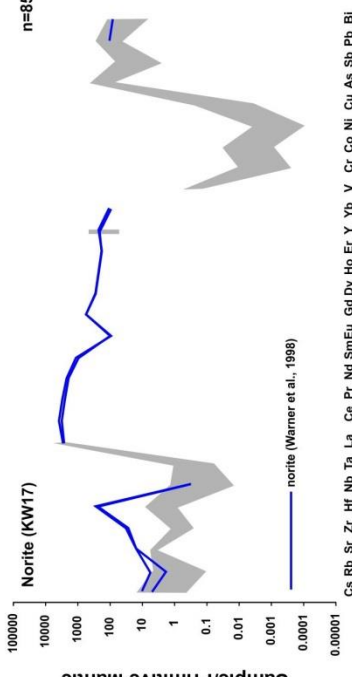
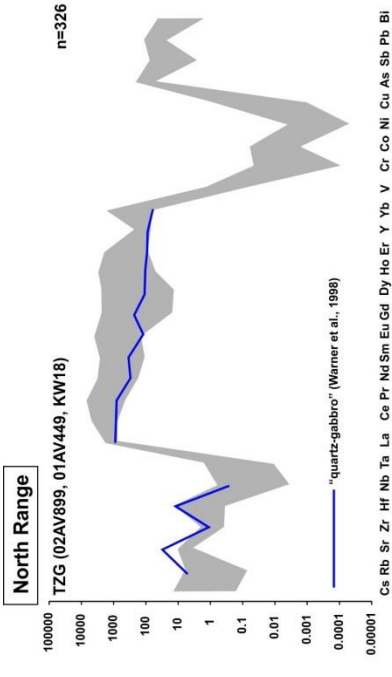
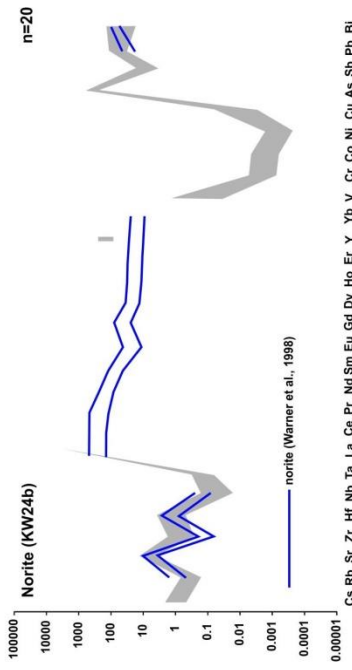
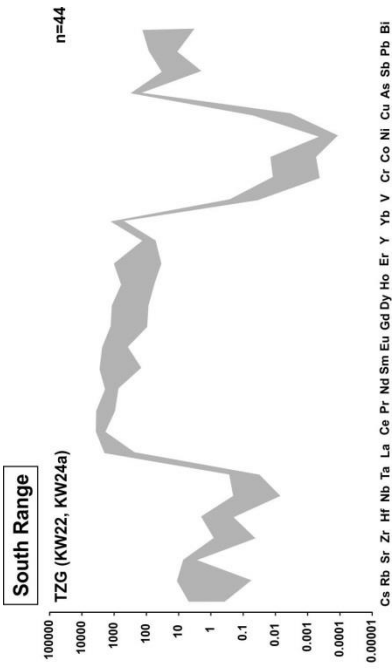


Figure 2.18: Apatite trace element and REE chemistry comparing the North and South Range Main Mass normalized to primitive mantle. Trace and REE are shown plotted for the TZG and norite apatite from this study. Values for apatite from the TZG, norite, and granophyre (Warner *et al.*, 1998) and for the South Range granophyre (Ames, personal communication) are plotted for comparison.

plagioclase and associated with cumulus orthopyroxene shows that apatite may be early in the norite and also bulk separation of apatite favoured the separation of large euhedral apatite for this study.

The enrichment of LREE in late crystallized apatite from the norite is suggested be the result of LREE partitioning into the intercumulus melt rather than cumulus silicate minerals (i.e. pyroxenes) that have D^{LREE} values less than 1 with respect to the melt, whereas apatite has a D^{LREE} much greater than 1 with respect to the melt (Warner *et al.*, 1998). The LREE (La, Ce, Pr, Nd) are highest in apatite from the norite in the Main Mass and decrease into the TZG, however trace element data for apatite by LA-ICP-MS for the Pele and Whistle offset show that the LREE (La) in apatite from the Pele offset has similar abundances to the TZG whereas is higher (more comparable to the norite) in apatite from the Whistle offset (Fig. 2.19, Table 2.3 and 2.4, Appendix A). This suggests that the early growth of apatite is not entirely dependent on the where it occurs stratigraphically in the SIC. For instance, in the noritic sublayer of the SIC apatite is abundant in mafic melanorite inclusions which is unusual considering that apatite is normally present in accessory levels in mafic rocks (Lightfoot *et al.*, 2001).

2.4.2.3 Evidence for silicate liquid immiscibility and constraints on the timing of immiscibility from major element chemistry of melt inclusions

The major element chemistry for both the Fe- and Si-rich melt inclusions from all units studied is strikingly similar. In this regard, it is noted that samples with melt inclusions from the TZG and the Pele offset were heated and homogenized prior to polishing in preparation for SEM-EDS and EMP analyses, thus these units provide the

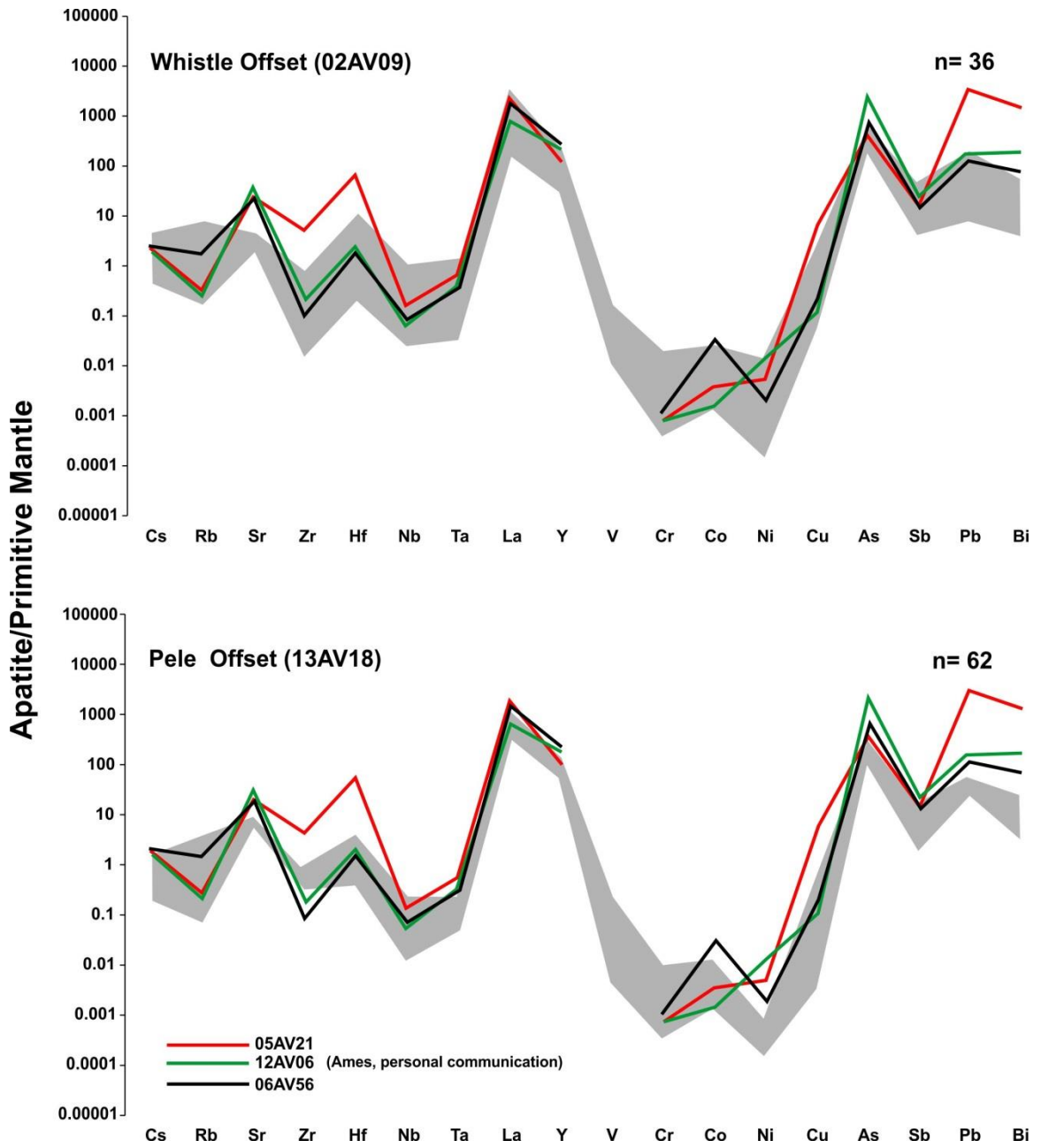


Figure 2.19: Apatite trace element chemistry of the mineralized Whistle offset dike and barren Pele offset dikes normalized to primitive mantle. Apatite in the Whistle offset shows the highest concentrations of As and Cu. Apatite from the mineralized footwall (Ames, personal communication) shows higher concentrations of As that are comparable to what is observed in apatite from the mineralized Whistle offset dike.

best comparison for major element chemistry. However, end-member melt compositions for samples from the norite and Whistle offset, as determined by LA-ICP-MS, show little to no differences in the ranges observed for SiO₂ and FeO contents of melt inclusions from the TZG or Pele offset (Table 2.5, Appendix A). In the TZG the compositions of the Si-rich melt range from ~61 to 79 wt % SiO₂ and ~0.16 to 11.58 wt % FeO, whereas apatite-hosted melt inclusions in the Pele offset have similar compositions with ~66.31 to 66.87 wt; % SiO₂ and ~11.87 to 13.57 wt; % FeO (Table 2.4, Appendix A). The main difference among these data is that the range in compositions is larger for melt inclusions from the TZG.

One of the most important similarities observed for the melt inclusions from the TZG, norite, and both the Pele and Whistle offsets is their high MgO contents. In basaltic liquids it has been shown that low temperature immiscible melts will show corresponding low MgO contents (Charlier *et al.*, 2013), thus it is significant to note that Fe-rich melt inclusions from the SIC are MgO rich compared to both Fe-rich melt inclusions from the Skaergaard Complex (average of 2.35 wt; %) and experimental basaltic liquids (average of 1.52 wt; %) (Charlier & Grove, 2012). Thus, for Fe-rich melt inclusions from the SIC, the average MgO contents follow: TZG, 7.27 wt; %, norite 11.59 wt; %, the Pele offset 3.80 wt; %, and the Whistle offset 13.32 wt; %. The melt inclusion major element chemistry for samples from the TZG and Pele offset are, however, considered slightly more accurate since, as noted above, they represent SEM-EDS and EMP analyses of homogenized melt inclusions (Table 2.4 and Table 2.5, Appendix A). The MgO composition of the Fe-rich melt inclusions is also significantly higher than the MgO contents of the inferred bulk SIC parental composition from the chilled margin of the

offset dikes (4.30 wt % MgO) (Lightfoot *et al.*, 2001) and the vitric andesite of the Onaping Formation (4.28 wt % MgO) (Ames, personal communication; Ames *et al.*, 2002). The MgO composition of Fe-rich melt inclusions is also significantly higher than the MgO contents based on whole rock analyses for both the North Range offset dikes (avg. 3.46 wt %). However, there are mafic-ultramafic constituents of the SIC that exhibit these high levels of MgO. For instance, the sublayer norites and gabbronorites have moderate to high MgO of 7 to 16 wt % (Lightfoot *et al.*, 2001).

2.4.2.4 Evidence for silicate liquid immiscibility from trace element chemistry of melt inclusions

Trace element concentrations and distribution of trace elements between Si- and Fe-rich melt inclusions ($K_d^{\text{Fe-rich melt/Si-rich melt}}$) determined for immiscible melt pairs in this study show that the majority of trace elements partition evenly between the Si- and Fe-rich liquids. The incompatible elements (Hf, Zr, Nb, Ta) show a slight affinity for the Si-rich liquid in the TZG and V and Co showing a slight affinity for the Fe-rich liquid in the TZG (Fig. 2.13, a-c). The calculated K_d values are very close to those determined experimentally for immiscible melt pairs in basalt (Veksler *et al.*, 2006) which are shown plotted of Figure 2.13. These latter findings coincide with that observed in the granophyre, which shows that trace elements ratios are relatively similar to the norite but that the granophyre contains nearly double the amount of incompatible elements, suggesting that the Si-rich melt observed in this study may have gone on to crystallize the granophyre.

Trace element patterns in the granophyre (Lightfoot *et al.*, 1997a) are strikingly similar to what is found in Si-rich melt inclusions from the Main Mass and Whistle and Pele offset dikes when normalized to primitive mantle (Fig. 2.20). The starting composition of the SIC, as inferred from the least altered vitric composition of the Onaping Formation (Ames *et al.*, 2002) also shows similar trends but, with less of a spike in the incompatible elements than shown by the Si-rich melt inclusions, which is in agreement with Si-rich liquid having slightly higher incompatible element enrichments (Fig. 2.20). Bulk rock trace element chemistry of the granophyre and leucocratic igneous textured sublayer matrix (Lightfoot *et al.*, 1997a) most closely follow the trace element trends of the least altered vitric composition of the Onaping Formation (Fig. 2.20). Trace element patterns in the bulk rock data for the mafic and felsic norite (Lightfoot *et al.*, 1997a) are similar to that observed in Fe-rich melt inclusions from the Main Mass and Pele and Whistle offset dikes, with the exception of Nb which has a much higher and opposing spike when normalized to primitive mantle than what is found in all Fe-rich melt inclusions (Fig. 2.21).

2.4.2.5 The onset of immiscibility in the SIC and subsequent differentiation of the melt sheet

When the major element chemistry of the Si- and Fe-rich liquids from apatite-hosted melt inclusions from the SIC are plotted on an enlarged part of the pseudo-ternary Grieg diagram, the inferred conjugate Fe- and Si-rich pairs fall on opposite ends of the two-liquid field near the binodal curve that separates the one- and two-liquid fields in the system leucite-fayalite-silica (Roedder, 1979) (Fig. 2.22). It has been shown that for

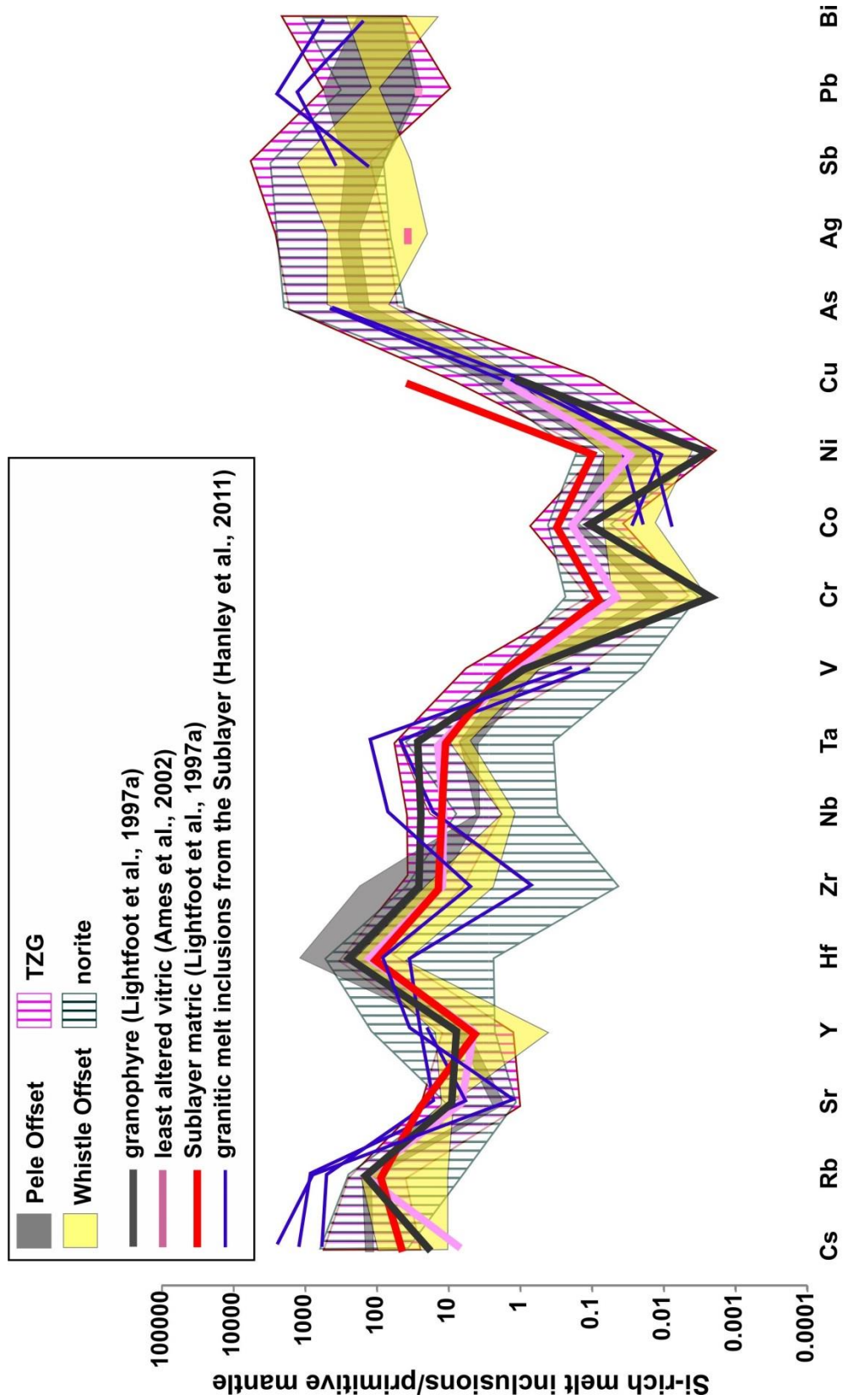


Figure 2.20: Spider diagram plot showing the trace element chemistry of Si-rich melt inclusions normalized to primitive mantle. The Si-rich melt inclusions hosted in apatite from the TZG and norite and shown by pink and grey striped fields, respectively. For comparison to the apatite hosted Si-rich melt inclusion data, the bulk rock composition of the granophyre (black) and leucocratic igneous textured sublayer matrix (red) (Lightfoot *et al.*, 1997a) are also plotted as a black line and red line, respectively. Granitic melt inclusions hosted in quartz from the SIC sublayer (Hanley *et al.*, 2011) are also shown and are plotted as a blue line. The trace element chemistry of the least altered vitric component of the Onaping Formation (Ames *et al.*, 2002) is plotted as a pink line.

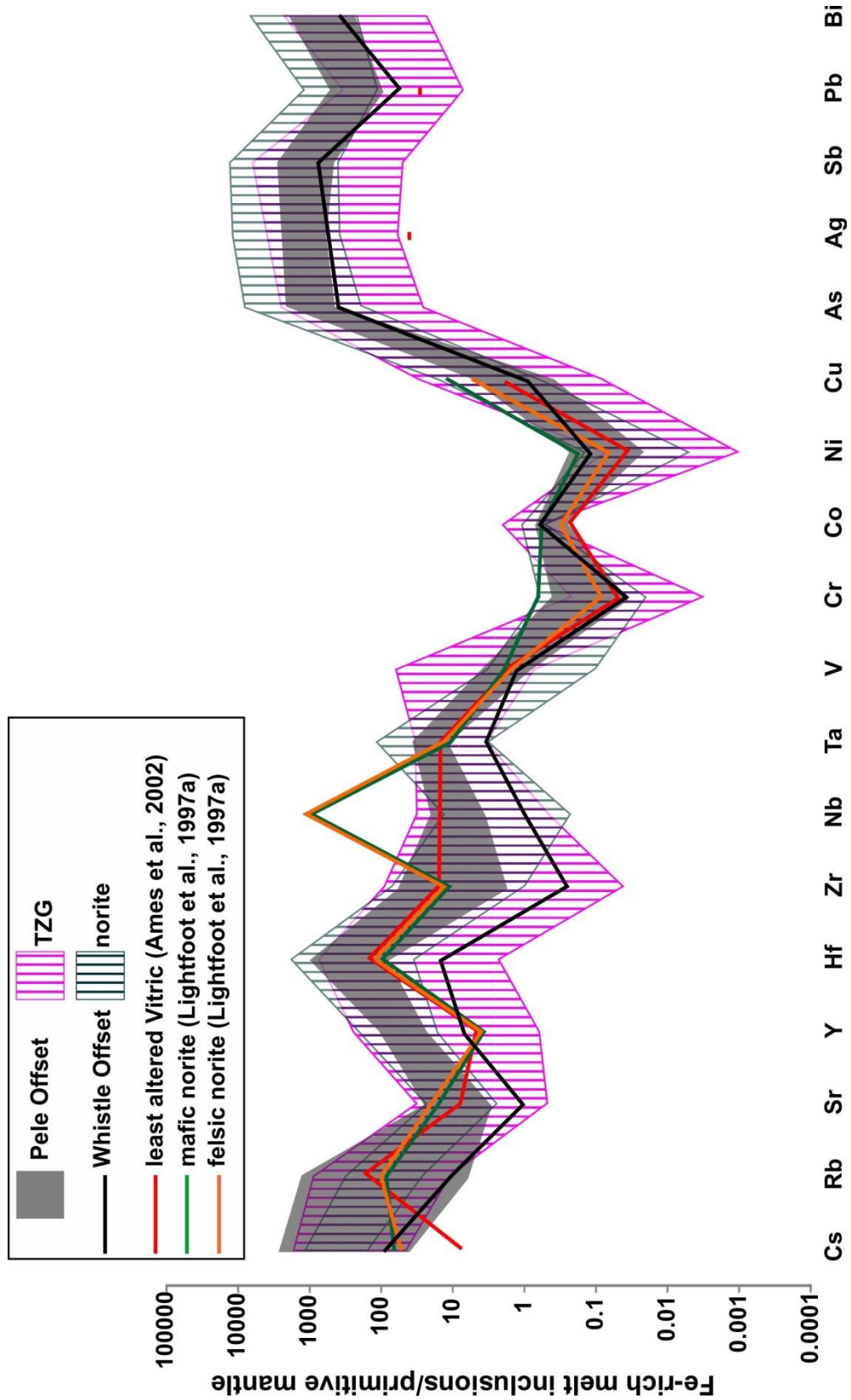


Figure 2.21: Spider diagram plot for trace element chemistry of the Fe-rich melt inclusions normalized to primitive mantle. The Fe-rich melt inclusions from the TZG and norite are shown as pink and green striped fields, respectively, and are compared with the Fe-rich melt inclusions of the Pele offset which are shown as a grey field, and one Fe-rich melt inclusion that was observed in the Whistle offset that is shown as a black line. The trace element composition of the bulk rock mafic and felsic norite (Lightfoot *et al.*, 1997a) are shown as green and orange lines, respectively. Trace element compositions of the least altered vitric component of the Onaping Formation (Ames *et al.*, 2002) are shown plotted by as a red line.

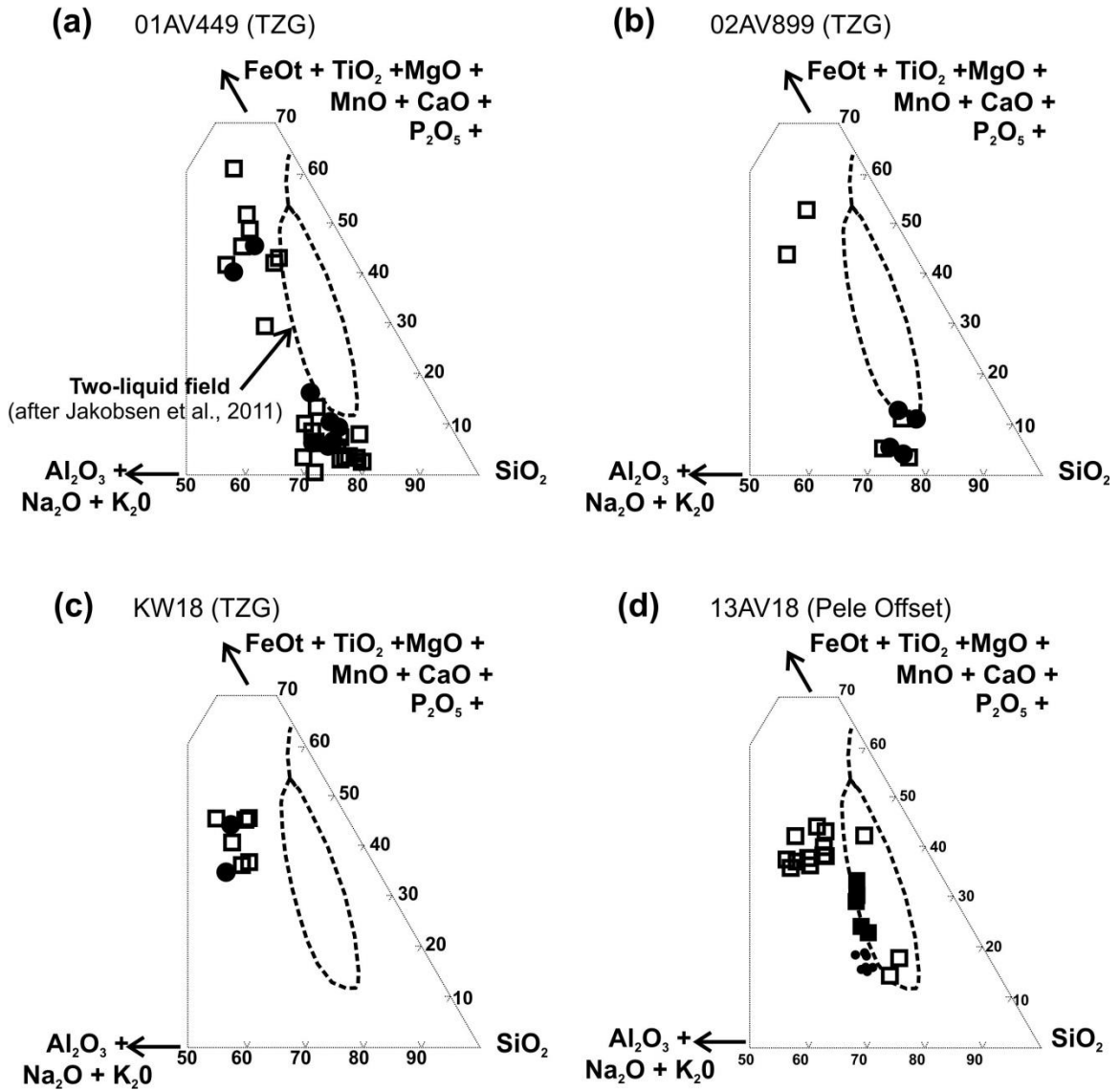


Figure 2.22: Major element chemistry of apatite-hosted melt inclusions from the Main Mass and quartz diorite Pele offset dike plotted on an enlarged part of the pseudo-ternary Grieg diagram (after Jakobsen et al., 2011). Apatite-hosted melt inclusions analysed by SEM (hollow squares) and EMP (solid circles) fall on opposite ends and close to the phase boundary of the two-liquid field in the system leucite-fayalite-silica after Roedder (1979) in the TZG (a-c) and Pele quartz diorite offset dike (d). In the Pele offset dike mixed (heterogeneously trapped) inclusions are plotted as solid squares and bulk compositions for offset dikes (Ermatinger, Hess, Ministic, Parkin, Pele, Trill) are plotted as small dots.

basaltic melts immiscibility may occur following the crystallization of major rock forming minerals along a liquid line of descent and that whether residual liquids will intersect the immiscibility field is dependent on minor bulk compositional changes (Namur *et al.*, 2012).

However, immiscibility may also result from simple cooling (Roedder, 1951) and the position of parental melt compositions for the SIC melt sheet which falls on or near or on the binodal (the intersection of the immiscibility field), supports this second scenario (Fig. 2.23). In Figures 2.23, it is shown that melt compositions from the TZG and Pele offset define a locus in P-T-X space that is shown as a best-fit line between these end-member melt pairs (e.g. experiments by Charlier & Grove, 2012). This best-fit line represents the binodal curve for the SIC melt sheet that when intersected by either the bulk liquid composition or an evolved liquid composition will experience stable immiscibility (Charlier & Grove, 2012, Namur *et al.*, 2012, Charlier *et al.*, 2013).

The chemical variation observed for melt inclusions in nature may be attributed to variable amounts of pyroxene and Fe-Ti oxide crystallization in the Fe-rich melts which, therefore, push the residual compositions towards the Si-apex or in the case of Si-rich melts sufficient plagioclase may not have crystallized, thus the melts have higher Al_2O_3 ; the result of the former is melt pair compositions in nature may fall within the two-liquid field (Charlier *et al.*, 2013). Therefore, the variability in major elements of melt inclusions in the SIC, shown as fields, that cause some to fall within the two-liquid field is likely a result of variable post-entrapment crystallization of daughter phases in melt inclusions (Fig. 2.23).

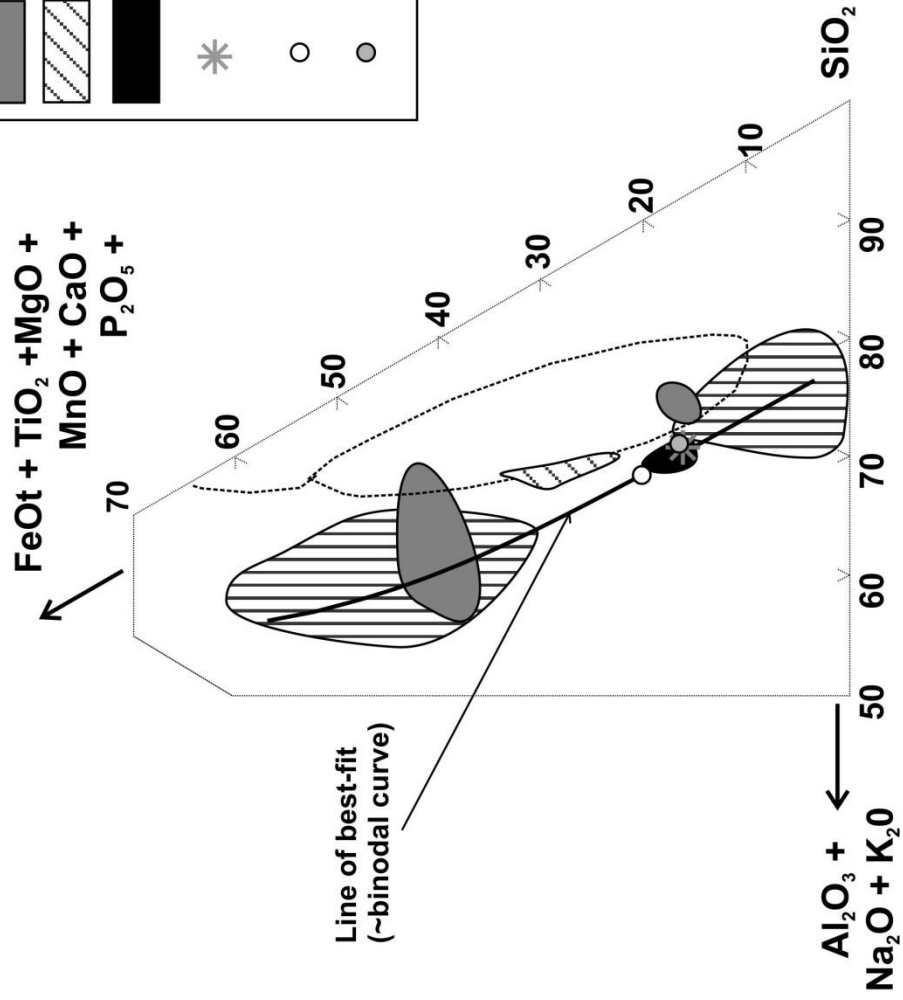
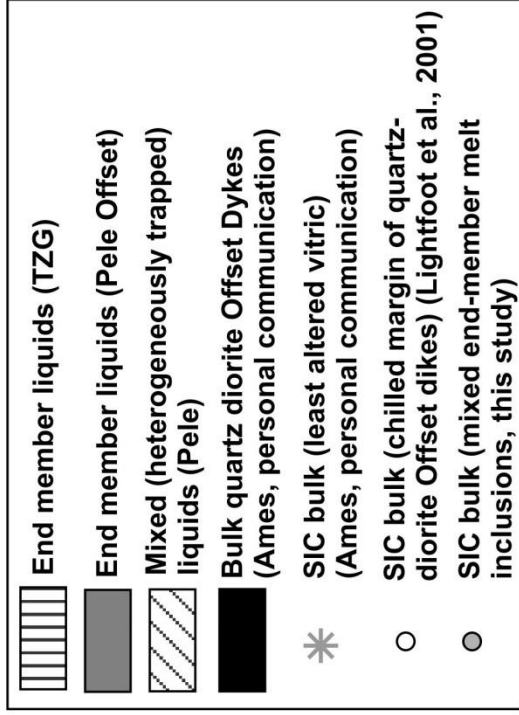


Figure 2.23: Major element chemistry of apatite hosted melt inclusions from the Main Mass TZG and Pele offset dike plotted as shaded fields on an enlarged part of the pseudo-ternary Grieg diagram with the binodal curve separating the one and two-liquid fields. Major element compositions from the Main Mass TZG (vertical striped fields) and Pele offset dike (grey shaded fields) are plotted along with the binodal curve that is drawn from a line of best-fit. The SIC bulk compositions are represented by the least altered vitric of the Onaping Formation (Ames et al., 2002) as a grey star and the chilled margin of the quartz diorite Offset dikes (Lightfoot *et al.*, 2001) as a hollow circle. The bulk composition that is calculated by mixing end-member liquids from this study is shown as a grey circle (see discussion for how the calculation was done). The North Range quartz diorite bulk rock compositions are shown plotted as a horizontal striped field (Ames, personal communication). The two-liquid field in the system leucite-fayalite-silica is shown as a dotted outline (Roedder, 1979) (after Jakobsen *et al.*, 2011).

Melt inclusion compositions in the SIC as are comparable to those that have been observed for the Skaergaard Complex (Jakobsen *et al.*, 2005; Jakobsen *et al.*, 2010) where immiscibility has been shown to occur (Fig. 2.24), although it has been shown that for basaltic melts immiscibility may occur following the crystallization of major rock forming minerals along a liquid line of descent and that whether residual liquids will intersect the immiscibility field is dependent on minor bulk compositional changes (Namur *et al.*, 2012). In Figure 2.24 two experimental basaltic liquids for the Sept Iles intrusion are shown, MCU II that surpassed the binodal along a liquid line of descent and experienced immiscibility and MCUI that reached its solidus before reaching the binodal (Namur *et al.*, 2012). Additionally, for basalts, if the bulk liquid experiences either Fe- or Si-enrichment along the liquid line of descent before reaching the binodal curve, the compositions of the melt pairs will be more drastically variable in terms of their FeO and SiO₂ contents, therefore widening the two-liquid field. In contrast if the bulk liquid remains relatively constant in terms of FeO and SiO₂ then the two-liquid field will be very narrow (Charlier *et al.*, 2013). The 30 experimental melt pairs plotted on Figure 2.24 are shown for a variety of liquid lines of descent and bulk liquid compositions for basalts; therefore the extent of the two-liquid field for basalts is shown fully on this diagram.

The parental compositions of experiments on fractional crystallization of the SIC (Ariskin *et al.*, 1999) are also shown plotted on Figure 2.24, the composition closest to the SiO₂ apex able to produce a volume of residual Si-rich liquid that could accommodate the granophyric unit of the SIC. However, the amount of granophyric liquid that would become trapped in cumulates of the norite during solidification would result in a lesser amount of granophyric liquid that would be available to crystallize as the upper

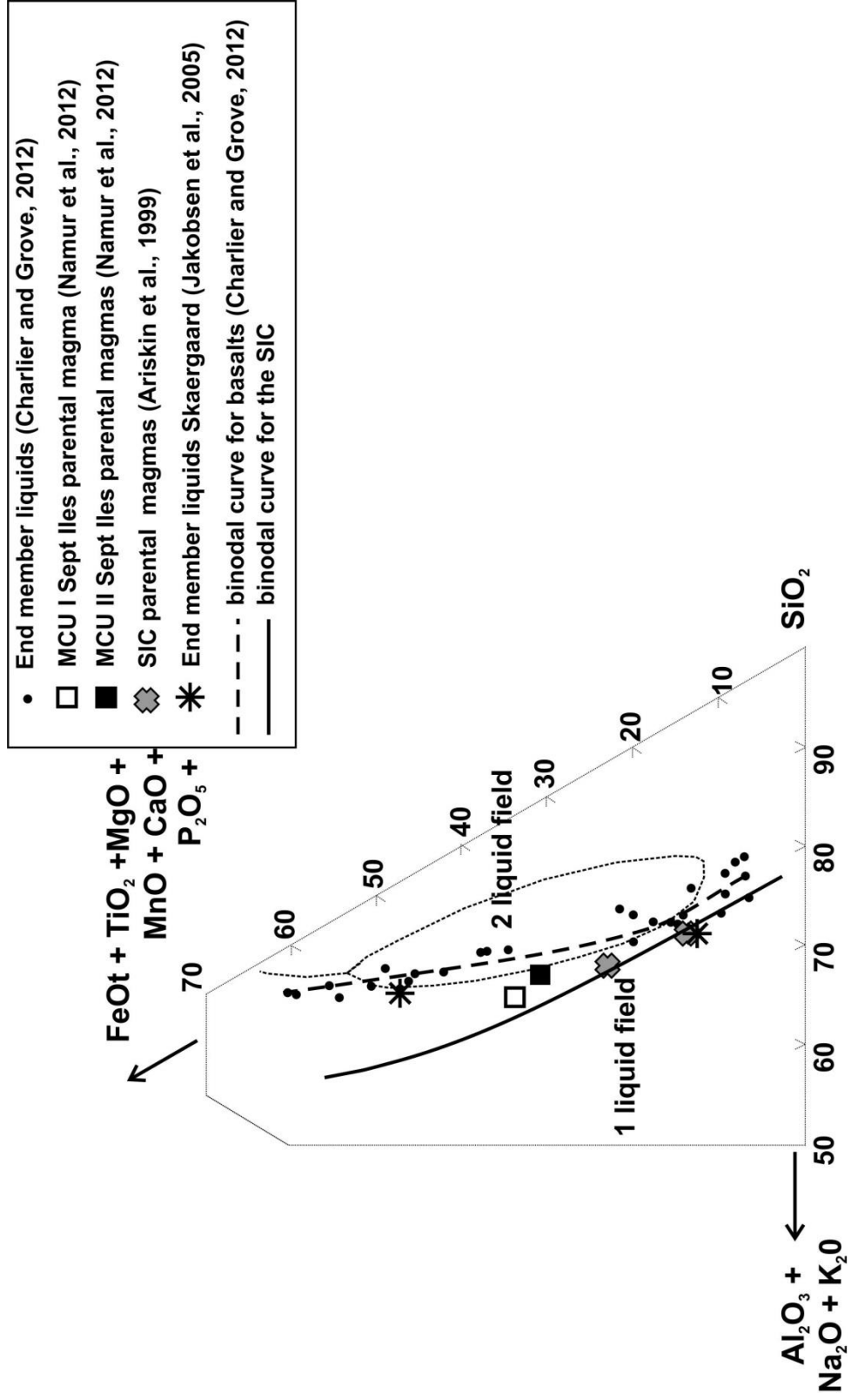


Figure 2.24: End-member immiscible liquids from experiments and from nature plotted on an enlarged part of the pseudo-ternary Grieg diagram with the binodal curve for basaltic liquids and for the SIC shown for comparison. Experimental end-member liquids from experiments (after Charlier & Grove, 2012) are shown plotted as solid black circles and define the binodal curve separating the one- and two-liquid fields for basaltic systems (dashed line). The binodal curve for the SIC is shown as a solid line. Two experimental liquid compositions from the Sept Iles intrusion, plotted as open and solid squares, represent data that did not surpass the binodal curve (MCUI) and that did surpass the binodal curve (MCUII) reaching stable immiscibility in models by fractional crystallization along a liquid line of descent. Experimental bulk compositions in experiments by Ariskin *et al.* (1999) are shown as grey x's with the composition that could produce the mafic constituents of the SIC closer to the Fe-apex and the composition that could not account for the mafic constituents of the SIC but produced significantly more granophyric residual liquid plotted closer to the Si-apex. Average end-member melt inclusion compositions from the Skaergaard intrusion are plotted as stars (Jakobsen *et al.*, 2005). The two-liquid field in the system leucite-fayalite-silica is shown as a dotted outline (Roedder, 1979) (after Jakobsen *et al.*, 2011).

granophyre unit of the SIC. In contrast, whereas the more mafic starting composition used in the experiments by Ariskin *et al.* (1999) (Fig 2.24) explained adequately the mafic constituents of the SIC, not nearly enough granophyric liquid was produced.

In the SIC, because the bulk liquid composition falls very close to the Si-rich end-member melt inclusion compositions and also to the two-liquid field, suggesting the bulk liquid is neither becoming enriched or depleted in SiO₂ or FeO before surpassing the binodal, it is expected that the two-liquid field would be very wide (i.e. very contrasting FeO and SiO₂ contents), as the proximity of the bulk liquid to the Si-rich end-member melts indicates that the field is being intersected on the limb of the binodal curve (closer to the Si-rich than Fe-rich side of the binodal curve) as oppose to near the closure, which is in agreement with the contrasting major element chemistry from melt inclusions from TZG and Pele offset (Fig. 2.22) (Table 2.2, Appendix A). The Fe-rich melt inclusions from the SIC are also higher in Al₂O₃, Na₂O and K₂O when compared to those in basalts, although the Si-rich liquids are very comparable to that observed for immiscible Si-rich liquids in basalts (Fig. 2.24). The binodal curve defined by end-member compositions in the SIC is, therefore, wider near the Fe-apex of the ternary than what is shown for the binodal curve for experimental immiscible melt pairs for basaltic parental compositions (Charlier and Grove, 2012) and for the Skaergaard Complex (Jakobsen *et al.*, 2005). However, the SIC parental liquid is andesitic in nature, and the shape of the binodal curve is defined by the bulk composition of the melt sheet at the time immiscibility is reached (Charlier & Grove, 2013) and as previously mentioned, we would expect the compositions of the earliest formed immiscible melts to be extensively variable.

As previously mentioned, the bulk composition of the SIC falls directly on the “binodal” that separates the one- and two-liquid fields, inferring that the bulk SIC melt sheet would reach the immiscibility field prior to changes in the bulk composition (i.e., by the crystallization of major rock forming minerals on the liquidus) (Fig. 2.23) which is in contrast to the timing of immiscibility onset in well studied basaltic intrusions (i.e. the Skaergaard intrusion, Greenland; the Sept Iles intrusion, Canada), where immiscibility is a consequence of the bulk liquid composition that surpasses the binodal along a liquid line of descent (Namur *et al.*, 2012). This early formation of an emulsion of Fe-and Si-rich melt pairs by way of immiscibility will only influence differentiation of the body of magma if there is adequate time for it to cool before cumulates start to grow, with larger intrusions able to undergo differentiation such as Sept Iles and the Bushveld complex. Large-scale differentiation of immiscible melts has also been suggested to result in a granophyre cap of some layered intrusions on Earth as the Bushveld Complex, South Africa (Namur *et al.*, 2012, VanTongeren & Mathez, 2012).

If the rate of cooling of a body of magma prohibits immiscible melt pairs to differentiate on a large-scale it becomes virtually impossible to distinguish the products of cumulate rocks that crystallized in an emulsion of Fe-and Si-rich melts from those that crystallized from homogeneous melt, as both contrasting liquids produce the same minerals, only in different proportions (Charlier *et al.*, 2011). However, early immiscible melts of the SIC melt sheet should have significant time to differentiate before crystallization and formation of cumulate phases (on the order of months) (Zieg & Marsh, 2005), thus eliminating the problem of a residual Si-rich melt becoming trapped in cumulates (e.g., Ariskin *et al.*, 1999). It is not surprising therefore, that apatite is trapping

Fe- and Si-rich melt inclusions on a micro scale. At the time that the melt sheet cooled enough for crystals to grow (possibly apatite) most of the denser mafic liquid constituents would have settled to the base of the complex but the extreme density of the Fe-rich liquid and the extreme viscosity of the felsic liquid (~10-15 times more viscous than the mafic liquid) would have trapped felsic liquid (parcels) whereas only very small blebs of mafic liquid would have remained in the felsic liquid phase above (Zieg & Marsh, 1999).

If immiscibility occurred early in the SIC melt sheet, then the large-scale compositional layering of the SIC in itself is considered to be evidence for large-scale differentiation of immiscible liquids. The ratio of the granophyre to norite is ~3:1 on the North Range and ~1:1 on the South Range (Kuo & Crocket, 1979) and the amount of granophyric liquid that is required in order to account for the volume of granophyre that is observed in the SIC cannot be accounted for by fractional crystallization alone (e.g., see experiments by Ariskin *et al.*, 1999). The quartz diorite offset dikes and, thought to be an even closer approximation, the primary shock melt composition of the Onaping Formation, are the most widely accepted parental compositions of the SIC Melt sheet (Lightfoot *et al.*, 2001, Ames *et al.*, 2002; Pope *et al.*, 2004). Therefore, we use the average composition of the vitric component of the Onaping in combination with compositions of Fe- and Si- rich melt inclusions for the Lever rule to define the ratio of FeO: SiO₂ rich liquids that would be produced upon unmixing (Fig. 2.25) and then mix the compositions of melt inclusions based on these proportions to compare with the bulk composition of the SIC inferred from the chilled margins of the quartz diorite offset dikes (Lightfoot *et al.*, 2001). The ratio of felsic to mafic liquids in the SIC that would be produced by unmixing of the parental composition at the binodal, inferred from

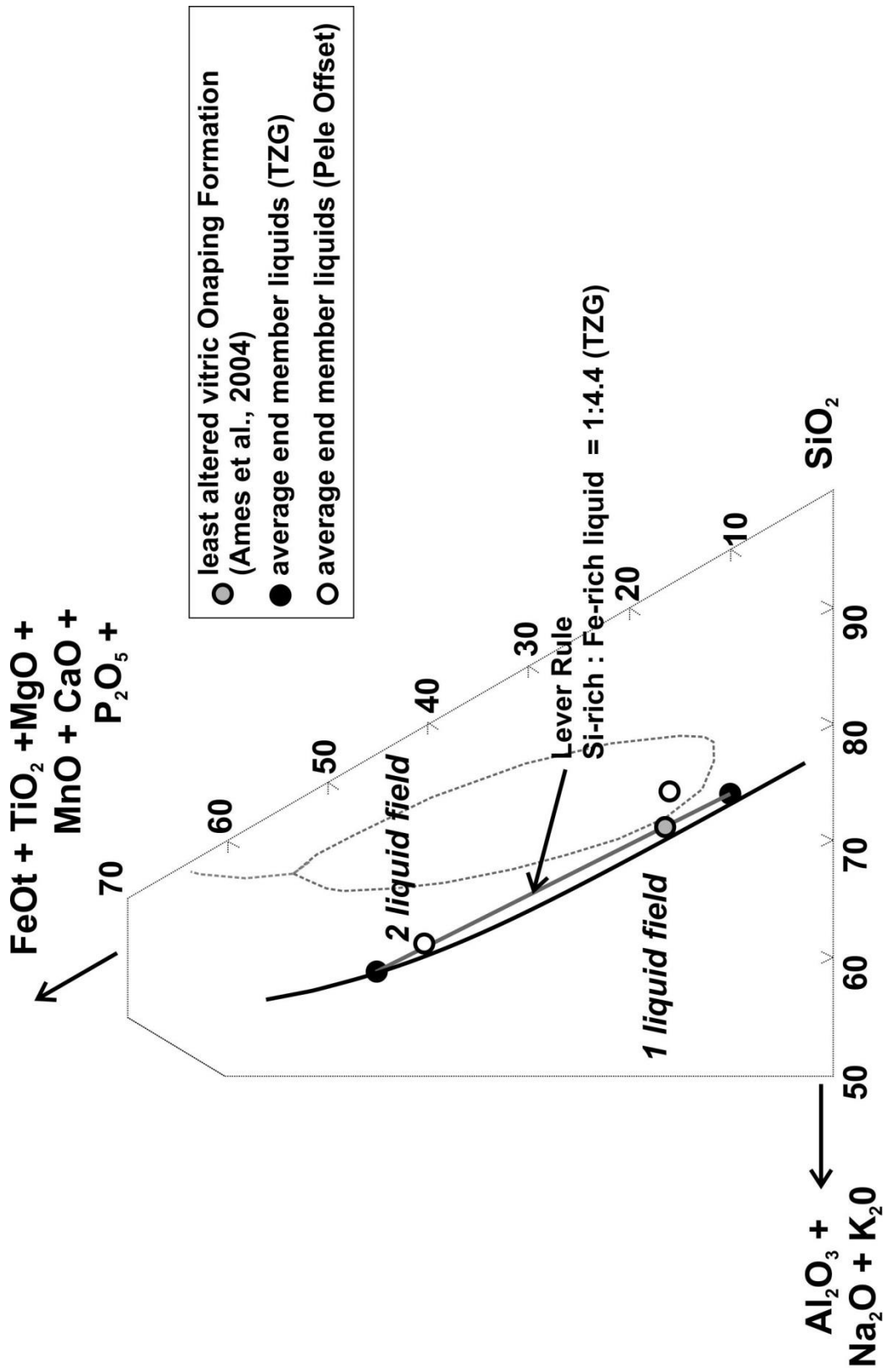


Figure 2.25: Ratio of Fe: Si-rich liquids observed in the SIC defined by the Lever Rule. The ratio of felsic to mafic liquids in the SIC that would be produced upon unmixing of the bulk SIC melt sheet composition (the shock melt of the Onaping Formation, Ames *et al.*, 2002) (grey circle) can be determined using the Lever Rule to be 78% Si-rich liquid and 22% Fe-rich liquid (~1:4.5). The average compositions of melt inclusions from the TZG (solid circles) were used for the Lever Rule, as more analysis were taken. The average compositions of melt inclusions from the Pele offset are also shown (open circles). The binodal curve for the SIC is shown as a solid curved line and the tie line connecting the average melt inclusion compositions that was used for the Lever Rule is shown as a solid straight line. Note that the bulk composition of the SIC falls on the tie line between contrasting melt inclusion compositions.

contrasting Si- and Fe-rich melt inclusion compositions, is determined by the Lever rule to be 78% Si-rich liquid and 22% Fe-rich liquid (~1:4.5) (Fig. 2.25). This is comparable to amount of granophyric liquid produced in experiments by Ariskin *et al.* (1999) (70% residual melt containing more than 67.50 wt % SiO₂).

Furthermore, if the average FeO content of the Fe-rich melt inclusions and average SiO₂ contents of the Si-rich melt inclusions are combined to produce the parental SiO₂ composition of the melt sheet: [(36.18 wt % SiO₂ * 22% Fe-rich liquid produced on unmixing) + (70.70 wt % SiO₂ * 78% Si-rich liquid produced upon unmixing)], then the parental SiO₂ content of the melt sheet is estimated to be 59.43 wt %, which is very similar to the proto SIC represented the quartz diorite offset dikes (63.10 wt % SiO₂; Fig. 2.23). The estimated bulk composition of the SIC, using the Lever Rule for all major elements of contrasting melt pairs is plotted on Figure 2.23 for comparison to the inferred parental SIC from the chilled margin of the offset dike (Lightfoot *et al.*, 2001).

2.5 Implications for the SIC evolution and timing of sulfide saturation

Si- and Fe -rich melt pairs show a decrease in both Ni and Cu contents from the base of the SIC to the Main Mass where melts are highly depleted in Ni compared to the offset dikes, notably the Whistle offset dike, which shows an enrichment of Ni (up to 4 orders of magnitude compared to melt inclusions from the Main Mass) (Table 2.5, Appendix A). The enrichment of Ni in melt inclusions from the offset dikes may be a result of (i) equilibrium between a sulfide liquid and locally Ni-enriched silicate liquid (predominately Fe-rich) or (ii) melt entrapment prior to sulfide saturation of the melt sheet. The potential influence that Si- and Fe-rich liquids in equilibrium with one another

may have on sulfide saturation of the melt sheet has never been studied before, although it has been suggested that immiscibility influenced the characteristics of mineralization types in the Skaergaard intrusion due to loss of immiscible granophyric melt (Nielsen, 2013). In addition to the Ni content shown in Table 2.5, Appendix A, an image of the LA-ICP-MS signals in SILLS demonstrates the common occurrence of a Ni peak coincident with other melt inclusion constituents from the Whistle offset (Fig. 2.26).

The $K_d^{\text{Fe-rich/Si-rich}}$ values for melt inclusions from the Whistle offset dike show that Ni is slightly more compatible in the Fe-rich melt; in addition, the minimum and maximum K_d values for immiscible melt compositions in the Pele offset are in agreement (Fig. 2.25). The $K_d^{\text{Fe-rich/Si-rich}}$ melt values are close to 1 with the exception of the Sr, Ta, Cr, Co, As, Ag, Sb, and Bi, all of which show affinity for the Fe-rich melt. It may be possible that Ni is present in higher concentrations near the base of the SIC where there is a larger volume of the dense Fe-rich immiscible liquid, and if we consider this it might be plausible that sulfide saturation in the SIC was influenced by the large amount of mafic melt that had settled to the base of the SIC.

Trace element concentrations in apatite from the Whistle offset are in agreement with the presence of a larger volume of Fe-rich immiscible melt at the base of the SIC at the time apatite nucleated. The trace element $K_d^{\text{apatite/melt}}$ values between apatite and Fe-rich and Si-rich melt indicate that the only elements that may be strongly compatible in apatite in Y and to a lesser extent As, Pb, and Bi (Fig. 2.11, 2.12) and the most significant increase for As in apatite is from the Whistle offset (~19 ppm in the Whistle offset, ~9 ppm in the norite, and ~4 ppm in the TZG). There is also a slight increase in Cu

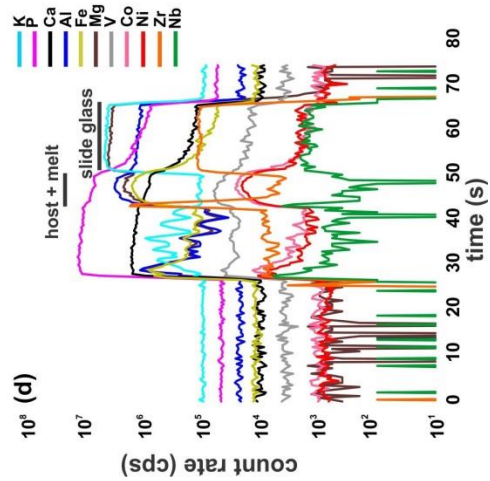
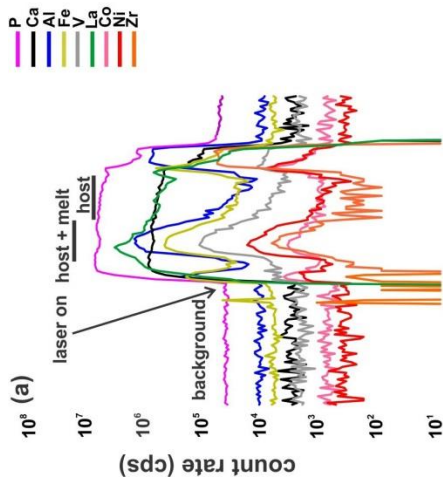
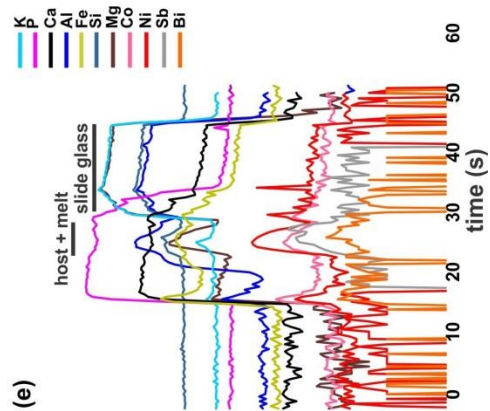
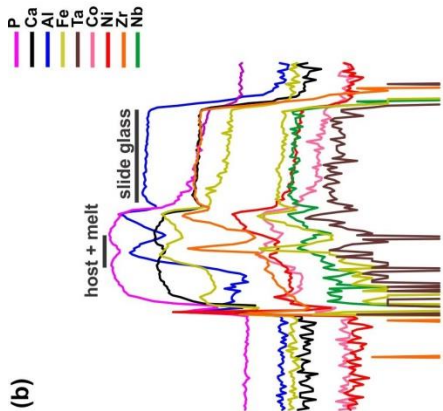
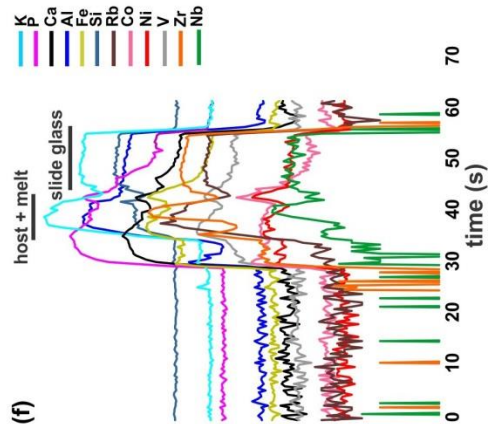
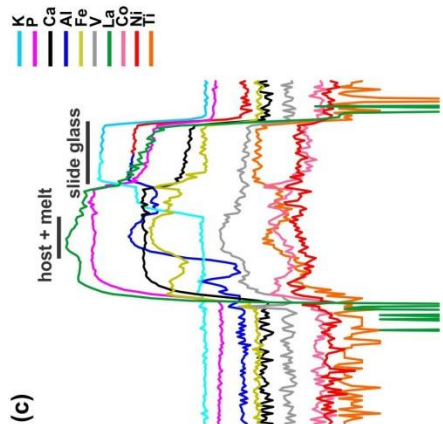


Figure 2.26: Plot of ablation time (s) versus count rate for element isotopes showing apatite-hosted melt inclusions in the Whistle offset dike. Six melt inclusions are shown from the Whistle offset dike. Image (a) shows the background interval before the laser is on and before it intersects the melt inclusion near the edge or center of the apatite grain (a-c) Show the characteristics of inferred “mixed inclusions”. (d-e) Show the characteristics of the Fe-rich inclusions and (f) shows an example of a Si-rich inclusion that contains an accidentally trapped Zr-mineral phase, a common problem when conducting data reduction of melt inclusions. The images provide a good reference for the problems encountered when choosing host and melt signals in SILLS. Contamination of the glass slide which hosts the melt inclusions and apatite is common (images c and d). Common elements are plotted that occur in the melt inclusions along with Ni, which is plotted as a red line that shows a significant increase in melt inclusions (images a, d, and e). Images (b, d and f) demonstrate the very common accidental entrapment of Zr-rich crystal phases that interfere with melt inclusion signals.

within apatite from the Whistle offset (~17 ppm) compared to that in apatite from the norite (~2 ppm) and TZG (1.2 ppm) and the Pele offset (~2.7 ppm) (Table 2.3).

Intervals of host and melt that are chosen in SILLS demonstrate that melt inclusions from the Whistle offset commonly contain trapped crystal phases, particularly Zr-bearing minerals (Fig. 2.26 b, f) or a mixture of end-member Si- and Fe-rich melts (Fig. 2.26 a-c), although zirconium may also occur as a constituent of the melt, as indicated by a smooth signal for Zr that follows Fe, Al, V, Co in several ablation profiles (Fig. 2.26 a, c). Notably, of the three melt inclusions containing end-member melts found in apatite from the Whistle offset, the two Fe-rich signals show that Ni is enriched by up to 4 orders of magnitude with respect to the norite and TZG (Fig. 2.26, d-e). Mixed signals also show significant increases in Ni (Fig. 2.26, a, c).

It is not likely that the saturation of apatite in the melt sheet which had already experienced differentiation of immiscible Si- and Fe-rich melts (within months of impact; Zieg & Marsh, 2005) pre-dates sulfide saturation of the melt sheet. If the melt sheet experienced in-situ crystallization of a previously density-stratified melt, the most basal layers in the density stratified melt sheet would be more mafic and may crystallize the Ni- and Cu-rich sulfide (Lightfoot *et al.*, 2001). Thus, it is suggested that apatite near the base of the SIC crystallized in the presence immiscible Si- and Fe- rich melts and that the dominant conjugate liquid near the base of the SIC would have been the dense Fe-rich liquid that had sunk to the base of the SIC. The enrichment of Ni in apatite hosted melt inclusions, therefore, is a result of trapped liquid that was in equilibrium with sulfide liquid.

2.6 Conclusions

Immiscibility is a widely accepted process that has been shown to occur in many volcanic and, to a lesser extent, some plutonic settings globally, that latter including such well known basic intrusions as the Skaergaard intrusion, East Greenland (Jakobsen *et al.*, 2005) and the Sept Iles intrusion, Canada (Namur *et al.*, 2012). The conditions that favour the onset of immiscibility in basalts and the extent to which immiscible melts will vary in composition is well understood for basaltic systems, however, a similar level of knowledge is currently lacking for more felsic systems, which would include the SIC, the subject of the present study.

The SIC is unique from all other well studied magmatic systems on Earth in several important respects. Firstly and most important, the melt that crystallized to form the SIC is the result of a bolide impact and the melt sheet generated was initially superheated (i.e. $>1700\text{ }^{\circ}\text{C}$) (Zieg & Marsh, 2005). Secondly, the SIC and its basement rocks, host the world's largest known concentration of Ni-Cu-PGE bearing sulfides. Immiscibility was not a process considered to play any role in the petrogenesis of the SIC, however, it has been suggested that the compositional layering of the SIC may have resulted from an initial emulsion of Si- and Fe-rich melts that differentiated in the liquid state. If one considers the “viscous emulsion” theory proposed by Zieg and Marsh (2005), it would be expected that the bulk liquid composition of the melt sheet would fall to the far right of the immiscibility field in the system leucite-fayalite-silica and near the 1600°C isotherm where the high temperature immiscibility field has been defined by Roedder (1979).

The proximity of the vitric andesite of the Onaping Formation (Ames *et al.*, 2004) and the chilled margins of the quartz diorite offset dikes (Lightfoot *et al.*, 2001) that represent the bulk composition of the SIC melt sheet fall on the tie line between Si- and Fe-rich immiscible melt pairs from the SIC and, therefore, on the binodal curve that separates the one- and two-liquid fields. The binodal curve for the SIC that has been determined from end-member melt pair compositions is also in close proximity binodal curve for basaltic systems and in the system leucite-fayalite-silica after Roedder (1979). However, for basaltic systems, the bulk composition must follow a liquid line of descent before reaching the immiscibility field, and falls to the left of the binodal curve. It is concluded that bulk composition of the SIC reached the immiscibility field as a result of very slow cooling (~0.5 Ma) of the superheated melt sheet rather than by crystallization along a liquid line of descent, unlike what has been shown to be the case for basaltic systems.

It is, therefore, also suggested that the onset of immiscibility pre-dates the crystallization of the melt sheet and resulted in the compositional layering that is observed in the Main Mass of the SIC. The nature of the compositional layering of the SIC, most notably manifested by the large volume of the granophyre unit, has been widely debated (Peredery & Naldrett, 1984, Chai & Eckstrand, 1994, Ariskin *et al.*, 1999). When the Lever Rule is applied in the pseudo-ternary (see Fig. 2.25), with the additional assumption of the quartz diorite offset dikes and least altered vitric dikes and clasts of the Onaping Formation reasonable proxies for the initial bulk liquid of the SIC, it is determined that unmixing of this melt could adequately produce sufficient volumes of Si-rich liquid to form the overlying granophyric unit (1:4.5). Although, similar

amounts of granophyric liquid have been produced by experiments on fractional crystallization (Ariskin *et al.*, 1999), the amount that would become trapped in the cumulate norite, as demonstrated by modelling parental melts using geological software programs, would result in a lesser volume of granophyre than what is observed in the SIC. Thus, if the SIC differentiated by unmixing of and subsequent sinking of dense Fe-rich melt globules that trapped some Si-rich conjugate liquid and Fe-rich micro scale blebs remained dispersed in the viscous Si-rich liquid above, prior to cumulate formation of the norite, as proposed by Zieg and Marsh (2005), then this process can account for the presently observed volume of granophyre in the SIC.

Furthermore, the partition coefficients between Si- and Fe- rich liquids, as determined from apatite-hosted melt inclusions, show that whereas most elements partition close to unity, the incompatible elements (Hf, Zr, Nb, Ta) show a slight affinity for the Si-rich liquid. These findings are consistent with that observed in the granophyre where most trace element ratios are relatively similar to those of the norite, but that the granophyre unit contains nearly double the amount of incompatible elements. This latter observation suggests that the Si-rich melt documented in this study may represent the melt which crystallized to form the granophyre.

Additional evidence for early immiscibility in the SIC is that microthermometric measurements for apatite-hosted melt inclusions from the TZG and Pele offset yield trapping temperatures for the melt inclusions that range from $\sim 1150^{\circ}$ to 1230°C . That immiscibility is a high temperature phenomenon in the SIC is further evidenced by the presence, during heating of mixed melt inclusions, of a meniscus between Fe- and Si-rich liquids at temperatures above 1250°C . The high MgO contents of all Fe-rich melt

inclusions from the base of the SIC to the TZG (3.8; wt % to 13.0 wt; %) is also a further indication that these are not low temperature immiscible melts (Charlier *et al.*, 2013).

The immiscible melts found in the Main Mass and are devoid of metals compared with melt inclusions from the mineralized quartz diorite Whistle offset. The absence of Ni and Cu in melt inclusions from the unmineralized Pele offset and Main Mass of the SIC may reflect loss of these metals to early sulfide liquids, however, if the differentiation of immiscible liquids resulted in a density stratified melt prior to in-situ crystallization processes, the most basal layers in the density stratified melt sheet would be more mafic and may crystallize the Ni- and Cu-rich sulfide (Lightfoot *et al.*, 2001). The Ni-rich apatite hosted melt inclusions from the Whistle offset are, therefore, likely a result of trapped immiscible liquid that was in equilibrium with sulfide liquid.

2.7 References

- Ames, D.E., Golightly, J.P., Lightfoot, J.P., & Gibson, H.L. (2002). Vitric compositions in the Onaping formation and their relationship to the Sudbury Igneous Complex, Sudbury Structure *Economic Geology* **97**, 1541-1562.
- Ames, D.E. & Farrow, C.E.G. (2007). Metallogeny of the Sudbury mining camp, Ontario, in Goodfellow, W.E., ed., Mineral Deposits of Canada: A Synthesis of Major Deposit-Types, District Metallogeny the Evolution of Geological Provinces, and Exploration Methods: Geological Association of Canada, *Mineral Deposits Division, Special Publication* **5**, 329-350.
- Anderson, D.L. (1982). Chemical composition of the mantle. *Journal of Geophysical Research* **88**, B41-B52.
- Ariskin, A. A., Deutsch, A., & Ostermann, M. (1999). Sudbury Igneous Complex: Simulating phase equilibria and in situ differentiation for two proposed parental magmas, in Dresser B.O., & Sharpton, V.L., eds., Large Meteorite Impacts and Planetary Evolution II: Boulder Colorado, *Geological Society of America Special Paper* **339**, 373-388.
- Bea, F., Pereira, M.D. and Stroh, A. (1994). Mineral/leucosome trace element partitioning in a peraluminous migmatite (a laser ablation-ICP-MS study). *Chemical Geology* **117**, 291-312.
- Boegaerts, M., & Schmidt, M.W. (2006). Experiments on silicate melt immiscibility in the system $\text{Fe}_2\text{SiO}_4\text{-KAlSi}_3\text{O}_8\text{-SiO}_2\text{-CaO-MgO-TiO}_2\text{-P}_2\text{O}_5$ and implications for natural magmas. *Contributions to Mineralogy and Petrology* **152**, 257-274.
- Bowen, N. L., (1928). Evolution of the Igneous Rocks. *Princeton University Press, Princeton*.
- Brooks, C.K. & Nielsen, T.F.D. (1990). A discussion of Hunter and Sparks (Contrib Mineral Petrol 95: 451–461). *Contributions to Mineralogy and Petrology* **104**, 244-247.
- Card, K.D, Gupta, V.K., McGrath, P.H., & Grant, F.S. (1984). The Sudbury Structure: its regional geological and geophysical setting, in E.G. Pye, A.J. Naldrett, P. Giblin, eds., The Geology and Ore Deposits of the Sudbury Structure. *Ontario Geological Survey, Spec. Pub.* **1**, 25-43.
- Chai, G., & Eckstrand, R. (1994). Rare-earth element characteristics and origin of the Sudbury Igneous Complex, Ontario, Canada. *Chemical Geology* **113**, 221-244.

- Charlier, B., Namur, O., Toplis, M.J., Schiano, P., Cluzel, M., Higgins, M.D., & Auwera, J.V. (2011). Large-scale silicate liquid immiscibility during differentiation of tholeiitic basalt to granite and the origin of the Daly gap. *Geology* **39**, 907-910.
- Charlier, B. & Grove, T.L. (2012). Experiments on liquid immiscibility along tholeiitic liquid lines of descent. *Contributions to Mineralogy and Petrology* **164**, 27–44.
- Charlier, B., Namur, O., & Grove, T.L. (2013). Compositional and kinetic controls on liquid immiscibility in ferrobasalt-rhyolite volcanic plutonic series. *Geochimica et Cosmochimica Acta* **113**, 79-93.
- Chung, H-Y. & Mungall, J.E. (2009). Physical constraints on the migration of immiscible fluids through partially molten silicates, with special reference to magmatic sulfide ores. *Earth and Planetary Science Letters* **286**, 14-22.
- Coats, C.J.A. & Snajdr, P. (1984). Ore deposits of the North Range, Onaping-Levack Area in E.G. Pye, A.J. Naldrett, P.E. Giblin (Eds.), *The geology and ore deposits of the Sudbury structure. Ontario Geological Survey Special Publication* **1**, 327-346.
- Darling, J.R., Hawkesworth, C.J., Storey, C.D., & Lightfoot P.C. (2010a). Shallow impact: isotopic insights into crustal contributions to the Sudbury impact melt sheet. *Geochimica et Cosmochimica Acta* **74**, 5680-5696.
- Darling, J.R., Hawesworth, C.J., Lightfoot, P.C., Storey, C.D., & Tremblay, E. (2010b). Isotopic heterogeneity in the Sudbury impact melt sheet. *Earth and Planetary Science Letters* **289**, 347-356.
- Darling J.R., Hawkesworth, C.J., Lightfoot, P.C., Storey, C.D., & Tremblay, E. (2010c). Response to the scientific comment by Dicken on “isotopic heterogeneity in the Sudbury impact melt sheet” [EPSL 289 (2010) 347-356]. *Earth and Planetary Science Letters* **300**, 44-45.
- Dawson, J. and Hinton, R. (2003). Trace element content and partitioning in calcite, dolomite, and apatite in carbonate, Phalaborwa, South Africa. *Mineralogical Magazine* **67**, 921-930.
- Dietz, R.S. (1964). Sudbury structure as an astrobleme. *Journal of Geology* **72**, 412-434.
- Dicken, A.P., Nguyen, T., & Crocket, J.H. (1999). Isotopic evidence for a single impact melting origin of the Sudbury Igneous Complex, in Dresser B.O., & Sharpton, V.L., eds., Large Meteorite Impacts and Planetary Evolution II: Boulder Colorado, *Geological Society of America Special Paper* **339**, 361-371.

- Dressler, B.O. (1984). General Geology of the Sudbury Area, in E.G. Pye, A.J. Naldrett, and P.E. Giblin, eds., *The Geology and Ore Deposits of the Sudbury Structure Ontario Geological Survey, Special Publication 1*, 57-82.
- Fagan, T.J., Taylor, G.J., Keil, K.K., Hicks, T.L., Killgore, M., Bunch, T.E., Wittke, J.H., Mittlefehldt, D.W., Clayton, R.N., Eugster, O., Lorenzetti, S., & Norman, M.D. (2003). Northwest Africa 773: Lunar origin and iron-enrichment trend. *Meteoritics & Planetary Science* **38**, 529-554.
- Faggart, B.E., Basu, A.R., & Tatsumoto, M. (1985). Origin of the Sudbury Complex by meteoritic impact: neodymium isotopic evidence. *Science* **230**, 436-439.
- Fujimaki, H. (1986). Partition-Coefficients of Hf, Zr, and Ree between Zircon, Apatite, and Liquid. *Contributions to Mineralogy and Petrology* **94**, 42-45.
- Farrow, C.E.G. & Watkinson, D.H. (1997). Diversity of precious-metal mineralization in footwall Cu-Ni-PGE deposits, Sudbury, Ontario: Implications for hydrothermal models of formation. *Canadian Mineralogist* **35**, 817-839.
- Farrow, C.E.G. & Lightfoot, P.C. (2002). Sudbury PGE revisited: Toward an integrated model. *Canadian Institute of Mining, Metallurgy and Petroleum Special Volume* **54**, 13-130.
- Farrow, C.E.G., Everest, J.O., King, D.M. & Jolette, C. (2005). Sudbury Cu (-Ni)-PGE systems: refining the classification using McCreehy West Mine and Podolsky Project case studies *Mineralogical Association of Canada, Short Course* **35**, 163-180.
- Gasparrini, E. & Naldrett, A.J. (1972). Magnetite and ilmenite in the Sudbury nickel irruptive. *Economic Geology* **67**, 605-621.
- Golightly, P.J. (1994). The Sudbury igneous complex as an impact melt: Evolution and ore genesis, in Lightfoot, P.C., and Naldrett, A.J. eds., Proceedings of the Sudbury-Noril'sk Symposium *Sudbury, Ontario Ministry of Northern Development and Mines, Ontario Geological Survey*, 105-118.
- Grant, R.W. & Bite, A. (1984). Sudbury Quartz Diorite Offset Dikes in E.G. Pye, A.J. Naldrett, P. Giblin, eds., *The Geology and Ore Deposits of the Sudbury Structure. Ontario Geological Survey Special Publication 1*, 275-300.
- Greig, J. (1927). Immiscibility in silicate melts: part I. *American Journal of Science* **s5-13**, 1-44.

- Grieve, R.F. (1991). The Sudbury structure: controversial or misunderstood? *Journal of Geophysical Research* **96**, 22, 753-22, 764.
- Guillong, M.M., Maier, D.L., Allan, M.M., Heinrich, C.A., and Yardley, B.W.D., 2008, Appendix A6: SILLS: a MATLAB based program for the reduction of laser ablation ICP-MS data of homogeneous materials and inclusions, in Sylvester P., ed., *Laser Ablation ICP-MS in the Earth Sciences: Current Practices and Outstanding Issues: Mineralogical Association of Canada Short Course Series* **40**, 328-333.
- Hart, S.R. & Zindler, A. (1986). In search of a bulk-Earth composition. *Chemical Geology* **57**, 247-267.
- Holness, M.B., Stripp, G., Humphreys, M.C.S., Veksler, I.V., Nielsen, T.F.D, & Tegner, C. (2011). Silicate liquid immiscibility within the crystal mush: late stage magmatic microstructures in the Skaergaard Intrusion, East Greenland. *Journal of Petrology* **52**, 175-222.
- Hoskin, P.W.O., Kinny, P.D., Wyborn, D., & Chappell, B.W. Identifying accessory mineral saturation during differentiation in granitoid magmas: an integrated approach. *Journal of Petrology* **41**, 1365-1396.
- Humphreys, M.C.S. (2011) Silicate liquid immiscibility within the crystal mush: evidence from Ti in plagioclase from the Skaergaard Intrusion. *Journal of Petrology* **52**, 147-174.
- Hunter, R.H. & Sparks, R.S.J. (1987). The differentiation of the Skaergaard intrusion. *Contributions to Mineralogy and Petrology* **95**, 451-461.
- Ivanov, B.A. & Deutsch, A. (1999). Sudbury impact event: cratering mechanics and thermal history, in Dresser B.O., & Sharpton, V.L., eds., *Large Meteorite Impacts and Planetary Evolution II: Boulder Colorado*, *Geological Society of America Special Paper* **339**, 389-397.
- Jakobsen, J.K., Veksler, I.V., Tegner, C., & Brooks, C.K. (2005). Immiscible iron-and silica-rich melts in basalt petrogenesis documented in the Skaergaard intrusion. *Geology* **33**, 885-888.
- Jakobsen, J.K., Veksler, I.V., Tegner, C., & Brooks, C.K. (2011). Crystallization of the Skaergaard intrusion from an emulsion of immiscible iron-and-silica-rich liquids: evidence from melt inclusions in plagioclase. *Journal of Petrology* **52**, 345-373.

- Keays, R.R. & Lightfoot, P.C. (2004). Formation of Ni-Cu-Platinum Group Element sulfide mineralization in the Sudbury Impact Melt sheet. *Mineralogy and Petrology* **82**, 217-258.
- Klemme, S. (2003). Trace element partitioning between apatite and carbonatite melt. *American Mineralogist* **88**, 639-646.
- Kontak, D.J., De Young, m.Y.D.W., & Dostal, J. (2002). Late-stage crystallization history of the Jurassic North Mountain Basalt, Nova Scotia, Canada. I. textural and chemical evidence for pervasive development of silicate liquid immiscibility. *The Canadian Mineralogist* **40**, 1287-1311.
- Kuo, H.Y. & Crocket, J.H. (1979). Rare earth elements in the Sudbury nickel irruptive: comparison with layered gabbros and implications for nickel petrogenesis. *Economic Geology* **74**, 590-605.
- Lightfoot, P.C., Keays R.R., Morrison G.G., Bite, A., & Farrell, K.P. (1997a). Geochemical relationships in the Sudbury Igneous Complex: origin of the Main Mass and Offset Dikes. *Economic Geology* **92** 289-307.
- Lightfoot, P.C., Keays R.R., Morrison, G.G., Bite, A., & Farrell, K.P. (1997b). Geologic and geochemical relationships between the Contact Sublayer, Inclusions, and the Main Mass of the Sudbury Igneous Complex: a case study of the Whistle Mine embayment. *Economic Geology* **92**, 647-673.
- Lightfoot, P.C., Reid R.K., & Doherty, W. (2001) Chemical evolution and origin of nickel sulfide mineralization in the Sudbury Igneous Complex, Ontario, Canada. *Economic Geology* **96**, 1855-1875.
- Lightfoot, P.C. & Farrow, E.G. (2002). Geology, geochemistry, and mineralogy of the Worthington Offset Dike: a genetic model for offset dike mineralization in the Sudbury Igneous Complex. *Economic Geology* **97**, 1419-1446.
- Lightfoot, P. C. & Zotov, I. A. (2005). Geology and Geochemistry of the Sudbury Igneous Complex, Ontario, Canada: Origin of Nickel Sulfide Mineralization Associated with an Impact-Generated Melt Sheet. *Geology of Ore Deposits* **47**, 349-381.
- Luhr, J.F., Carmichael, I.S.E. and Varekamp, J.C. (1984). The 1982 eruptions of El Chichon volcano, Chiapas, Mexico: mineralogy and petrology of the anhydrite-bearing pumices. *Journal of Volcanology and Geothermal Research* **23**, 69-108.
- Mahood, G.A. and Stimac, J.A. (1990). Trace element partitioning in pantellerites and trachytes. *Geochimica et Cosmochimica Acta* **54**, 2257-2276.

- McBirney, A. R., & Naslund, H. R. (1990). The differentiation of the Skaergaard intrusion. *Contributions to Mineralogy and Petrology* **104**, 235-240.
- McBirney, A.R. (2008). Comments on: 'liquid immiscibility and the evolution of basaltic magma' *Journal of Petrology* 48, 2187-2210. *Journal of Petrology* **49**, 2169-2170.
- McDonough, W.F & Sun, S.-S. (1995). Composition of the Earth. *Chemical Geology* **120**, 223-253.
- Meurer, W.P. & Boudreau, A.E. (1996). An evaluation of models of apatite compositional variability using apatite from the Middle Banded series of the Stillwater Complex, Montana. *Contributions to Mineralogy and Petrology* **125**, 225-236.
- Morse, S.A. (2008). Compositional convection trumps silicate liquid immiscibility in layered intrusions: a discussion of 'liquid immiscibility and the evolution of basaltic magma' by Veksler et al., *Journal of Petrology* 48, 2187-2210. *Journal of Petrology* **49**, 2157-2168.
- Mungall, J.E. (2002). Late-Stage Sulfide Liquid Mobility in the Main Mass of the Sudbury Igneous Complex: Examples from the Victor Deep, McCreedy East, and Trillabelle Deposits. *Economic Geology* **97**, 1563-1576.
- Mungall, J.E., Ames, D.E., & Hanely, J.J. (2004). Geochemical evidence from the Sudbury structure for crustal redistribution by large bolide impacts. *Letters to Nature* **429**, 546-548.
- Mungall, J.E., Andrews, D.R.A., Cabri, L.J., Sylvester, P.J., & Tubrett, M. (2005). Partitioning of Cu, Ni, Au, and platinum-group elements between monosulfide solid solution and sulfide melt under controlled oxygen and sulfur fugacities. *Geochimica et Cosmochimica Acta* **69**, 4349-4360.
- Mungall, J.E., Andrews, D.R.A., Cabri, L.J., Sylvester, P.J., & Tubrett, M. (2005). Partitioning of Cu, Ni, Au, and platinum-group elements between monosulfide solid solution and sulfide melt under controlled oxygen and sulfur fugacities. *Geochimica et Cosmochimica Acta* **69**, 4349-4360.
- Mungall, J. E. (2007). Crystallization of magmatic sulfides: An empirical model and application to Sudbury ores. *Geochimica et Cosmochimica Acta* **71**, 2809-2819.
- Mungall, J.E. & Naldrett, A.J. (2008). Ore deposits of the platinum-group elements. *Elements* **4**, 253-258.

- Naldrett, A.J. (1969). A portion of the Fe-S-O and its application to sulphide ore magmas. *Journal of Petrology* **10**, 171-201.
- Naldrett, A. J. (1984a) Mineralogy and composition of the Sudbury ores, in Pye, E.G., Naldrett, A.J., and Giblin, P.E., eds., *The geology and ore deposits of the Sudbury structure: Toronto, Canada, Ministry of Natural Resources* **1**, 309-325.
- Naldrett A.J., Bray J.G., Gasparriani E.L., Podolsky T., & Rucklidge J.C. (1970). Cryptic variation and the petrology of the Sudbury Nickel Irruption. *Economic Geology* **65**, 122-155.
- Naldrett, A. J. & Hewins, R.H. (1984). The main mass of the Sudbury igneous complex in E.G. Pye, A.J. Naldrett, P. Giblin, eds., *The Geology and Ore Deposits of the Sudbury Structure: Ontario Geological Survey, Special publication* **1**, 233-251.
- Naldrett, A. J., Hewins, R.H, Dressler, B. O., & Rao, B.V. (1984). The Contact Sublayer of the Sudbury igneous complex in E.G. Pye, A.J. Naldrett, P. Giblin, eds., *The Geology and Ore Deposits of the Sudbury Structure: Ontario Geological Survey, Special publication* **1**, 254-273.
- Naldrett, A.J., Pesseran, A., Asif, M., & Li, C., (1994b). Compositional variation in the Sudbury ores and prediction of the proximity of footwall copper-PGE ore bodies: *Ontario Geological Survey Special Publication* **5**, 133-146.
- Namur, O.N., Charlier, B., & Holness, M.B. (2012b). Dual origin of Fe-Ti-P gabbros by immiscibility and fractional crystallization of evolved tholeiitic basalts in the Sept Iles layered intrusion. *Lithos* **154**, 100-114.
- Nielsen, T.F.D. (2013). Origin of the world-class PGE-Au mineralisation in the Skaergaard intrusion by bulk S-saturation, accumulation, partial dissolution, and secondary reef formation. *Geophysical Research Abstracts* **15**, EGU2013-7879
- Paster, T.P., Schauwecker, D.S. & Haskin, L.A. (1974). The behavior of some trace elements during solidification of the Skaergaard layered series. *Geochimica et Cosmochimica Acta* **38**, 1549-1577.
- Peredery, W.V. & Naldrett, A.J. (1975). Petrology of the upper irruptive rocks, Sudbury, Ontario. *Economic Geology* **70**, 164-175.
- Philpotts, A.R. (1976). Silicate liquid immiscibility: Its probable extent and petrogenetic significance. *American Journal of Science* **276**, 1147-1177.

- Philpotts, A.R. (1979). Silicate liquid immiscibility in tholeiitic basalts. *Journal of Petrology* **20**, 99-118.
- Philpotts, A.R. (1982). Compositions of immiscible liquids in volcanic rocks. *Contributions to Mineralogy and Petrology* **80**, 201-218.
- Pope, K.O., Kieffer, S.W., & Ames, D.E. (2004). Empirical and theoretical comparisons of the Chicxulub and Sudbury impact structures. *Meteoritics & Planetary Science* **39**, 97-116.
- Ripley, E.M., Severson, M.J., & Hauk, S.A. (1998). Evidence for sulfide and Fe-Ti-P-rich liquid immiscibility in the Duluth complex, Minnesota. *Economic Geology* **93**, 1052-1062.
- Roedder, E. (1951). Low temperature liquid immiscibility in the system $K_2O-FeO-Al_2O_3-SiO_2$. *American Mineralogist* **36**, 282-286.
- Roedder, E. (1956). The role of liquid immiscibility in igneous petrogenesis: a discussion. *The Journal of Geology* **64**, 84-88.
- Roedder, E. (1978). Silicate liquid immiscibility in magmas and in the system $K_2O-FeO-Al_2O_3-SiO_2$: an example of serendipity. *Geochimica et Cosmochimica Acta* **42**, 1597-1617.
- Roedder, E. (1979). The evolution of igneous rocks. *Princeton University Press, Princeton*.
- Sun, S.-S. (1982). Chemical composition and origin of the earth's primitive mantle. *Geochimica et Cosmochimica Acta* **46**, 179-192.
- Therriault, A.M., Fowler, A.D., & Grieve, R.A.F. (2002). The Sudbury Igneous Complex: A differentiated impact melt sheet. *Economic Geology* **97** 1521-1540.
- Thy, P., Leshner, C.E., Nielson, T.F.D., & Brooks, C.K. (2006). Experimental constraints of the Skaergaard liquid line of descent. *Lithos* **92**, 154-180.
- Tibor, G., Mitchell, R.H, Szabo, C., Berkesi, M., Milke, T., & Abart, R. (2011). Carbonatite melt inclusions in coexisting magnetite, apatite, and monticellite in Kerimasi calciocarbonatite, Tanzania: melt evolution and petrogenesis. *Contributions to Mineralogy and Petrology* **161**, 177-196.
- Toplis, M.J., Dingwell, D.B., & Libourel, G. (1994). The effect of phosphorous on the iron redox ratio, viscosity, and density of an evolved ferro-basalt. *Contributions to Mineral Petrology* **117**, 293-304.

- VanTongeren, J.A., Mathez, E.A. (2012). Large-scale liquid immiscibility at the top of the Bushveld Complex, South Africa. *Geology* **40**, 491-494.
- Veksler, I.V. (2004). Liquid immiscibility and its role at the magmatic-hydrothermal transition: a summary of experimental studies. *Chemical Geology* **210**, 7-31.
- Veksler, I.V., Dorfman, A.M., Danyushevsky, L.V., Jakobsen, J.K., Dingwell, D.B. (2006). Immiscible silicate liquid partition coefficients: implications for crystal-melt element partitioning and basalt petrogenesis. *Contributions to Mineralogy and Petrology* **152**, 685-702.
- Veksler, I.V., Dorfman, A.M., Borisov, A.A., Wirth, R., & Dingwell, D.B. (2007). Liquid Immiscibility and the evolution of basaltic magma. *Journal of Petrology* **48**, 2187-2210.
- Veksler, I.V., Dorfman, A., Borisov, A.A., Wirth, R., & Dingwell, D.B. (2008). Liquid immiscibility and evolution of basaltic magma: reply to S. A. Morse, A. R. McBirney and A. R. Philpotts. *Journal of Petrology* **49**, 2177-2186.
- Veksler, I.V., Kahn, J., Franz, G., & Dingwell, D.B. (2010). Interfacial tension between immiscible liquids in the system K₂O-FeO-Fe₂O₃-Al₂O₃-SiO₂ and implications for the kinetics of silicate melt unmixing. *American Mineralogist* **95**, 1679-1685.
- Warner, S., Martin, R.F., Abdel-Rhaman, A-F.M., & Doig, R. (1998). Apatite as a monitor of fractionation, degassing, and metamorphism in the Sudbury Igneous Complex, Ontario. *The Canadian Mineralogist* **36**, 981-999.
- Watson, E.B. and Green, T.H. (1981). Apatite/liquid partition coefficients for the rare earth elements and strontium. *Earth and Planetary Science Letters* **56**, 405-421
- Zieg, M.J. & Marsh, B.D. (2005). The Sudbury Igneous Complex: viscous emulsion differentiation of a superheated impact melt sheet. *Geological Society of America Bulletin* **117**, 1427-1450.

Chapter 3: Application of Study and Suggestions for Future Work

3.1 Limitations of Study and Future Work

Apatite-hosted melt inclusions were determined to be end-member compositions in the TZG and Pele offset dike by heating to homogenize and polishing into by hand to expose for SEM-EDS and EMP analyses. For trace element chemistry of apatite-hosted melt inclusions from the TZG, the abundance of melt inclusions allowed for multiple signals to be run through SILLs in order to pick out apatite, host, and standard intervals. Larger data sets for melt inclusion trace element chemistry from the TZG allowed for easier determination of trace element distribution in each melt type and allowed for more end-member compositions to be picked out from the data set. However, apatite-hosted melt inclusions from the norite were less abundant and smaller in size. Therefore, the small size of melt inclusions meant that signals were more difficult to unmix from host apatite in SILLs and less abundance meant less end-member compositions in the final data set. Apatite from the Whistle offset dike saw the most complications when unmixing signals in SILLs. Approximately 150-200 melt inclusions were mapped for analyses; however the extremely common occurrence of accidentally trapped Zr crystal phases in the melt inclusions meant that many signals were not representative (only 2 end-member compositions remain in the final data set). Additionally, apatite separates should be mounted on pucks for analysis by LA-ICP-MS for less chance of glass contamination in signals, although contamination is still likely for smaller apatite grains.

Throughout this study a large portion of available time was spent mapping melt inclusions for LA-ICP-MS. A very small portion of apatite grains was placed within each

puck to make it easier to relocate mapped grains on the laser. The mapping of melt inclusions was necessary, as the LA-ICP-MS optics is not feasible for seeing the melt inclusions on the screen. The size and shape of apatite, along with the pattern of surrounding apatite grains on the puck were the only proxy for aiming the laser and hitting the melt inclusions. For future melt inclusion work on apatite in the SIC, I suggest that a LA-ICP-MS with better optics is employed for (i) preserving time and (ii) obtaining more accurate melt data upon ablation.

Apatite is an abundant phase in the SIC and while studies have concluded that apatite is crystallizing late from the melt sheet, I suggest trace and particularly REE chemistry of apatite from each individual unit of the SIC be studied in order to determine if there are multiple crystallization events of apatite occurring in each unit. Particular emphasis should be placed on trace element zoning in apatite that may be used as a proxy for timing of apatite growth from the melt sheet. Only 2 apatite grains were mapped for zoning in this study, one from the TZG and the other from the norite and additional element maps of apatite may lead to better constraints on the timing of melt entrapment in apatite throughout the SIC and in turn help to elaborate on some of the remaining questions on timing of immiscibility in the SIC melt sheet and timing of sulfide saturation. In addition, the large abundance of apatite in the SIC is unusual, notably associated with mafic phases near the base of the SIC. Under the advisement of Dr. Alan Boudreau, it is suggested that software program PELE be employed to better constrain the onset of immiscibility in the SIC and to place additional constraints on apatite saturation from both the Si-rich and Fe-rich liquids separately, the Fe-rich and Si-rich liquids in equilibrium, and from bulk SIC composition.

3.2 Potential Exploration Criteria for the SIC

Apatite-hosted melt inclusions that were compared between mineralized (Whistle) and unmineralized (Pele) offset dikes revealed that melt inclusions in close proximity to mineralization contain high (upwards of 400 ppm) amounts of Ni. In addition, apatite from the Whistle offset contained the highest amounts of Cu and As. These findings compare to what is found in apatite from the mineralized footwall and may be applicable to exploration in the SIC. I suggest that similar comparisons be placed between mineralized and unmineralized zones with the intent of determining the maximum distance to the ore bodies that apatite is highest in As and Cu and that apatite-hosted melt inclusions are enriched in Ni. The conclusions of this study suggest that apatite-hosted melt inclusions from the Whistle offset dike were in equilibrium with sulfide liquids at the time of their entrapment. Therefore, the metal content of apatite-hosted melt inclusions in the basal portions of the SIC may serve as a proxy for distance to ore bodies within the SIC.